Automated analysis of ultrasound imaging of muscle and tendon in the upper limb using artificial intelligence methods

Shaima Ibraheem Jabbar

This thesis is submitted in partial fulfilment of the requirements for the degree of

Doctor of Philosophy in Biomedical Engineering

October 2018

Keele university

ACKNOWLEDGEMENTS

Though the following dissertation is an individual work, I could never have reached the heights or explore the depths without the help, support, guidance, and effort of many people in so many ways.

Firstly, I owe my deepest gratitude to my lead supervisor Dr. Edward Chadwick, Senior Lecturer in Biomedical Engineering, Institute for Science and Technology in Medicine, Guy Hilton Research Centre. Without his continuous optimism concerning this work, enthusiasm, encouragement and support this study would hardly have been completed.

I also express my warmest appreciation to my second supervisor Dr. Charles Day, a Lecturer in Computer Science and Mathematics at Keele University. His passion, guidance and comments were essential to complete this dissertation.

I would like to thank my advisor Prof. Anand D Pandyan, Professor of Rehabilitation Technology & Head of Rehabilitation School at Keele University for his kind help and support.

I would like to thank Mr. Nicholas Heinz for assistance in collection of the panoramic ultrasound images.

I would like to express my deepest gratefulness to my homeland Iraq and to the Iraqi Government and to the Higher Minister of Education for granting the funding of this PhD study. Also, I would like to thank the Iraqi Cultural Attache, London, UK for their kind help and advice through-out the long journey of my study.

Special deepest gratitude to Abathar Qahtan Aladi, my best friend and husband for his continuous love, passion, support, and for providing me with faith during the whole 12 years of our marriage. Without your encouragement the world would have seemed a lonely place.

I would like to thank my lovely daughter Rafeef and my two sons Ahmad and Yasser. They have been a great inspiration to me and filled my life with joy and happiness.

A special and tremendous gratitude to my father and mother who have walked alongside me during my life journey. They have guided me, placed opportunities in front of me and showed me the doors that might be useful to open.

Special thanks should also go to my lovely sisters and brothers. Without your support and encouragement, this work could not see the light.

Finally, I would like to express my sincere thanks to my colleague in the office, Mackay Building, Keele University for their support and help during this long journey. Also, a big special thank should go the secretary department at Mackay Building, Keele University for all their support and kind help.

Abstract

Accurate estimation of geometric musculoskeletal parameters from medical imaging has a number of applications in healthcare analysis and modelling. In vivo measurement of key morphological parameters of an individual's upper limb opens up a new era for the construction of subject-specific models of the shoulder and arm. These models could be used to aid diagnosis of musculoskeletal problems, predict the effects of interventions and assist in the design and development of medical devices. However, these parameters are difficult to evaluate in vivo due to the complicated and inaccessible nature of structures such as muscles and tendons. Ultrasound, as a non-invasive and low-cost imaging technique, has been used in the manual evaluation of parameters such as muscle fibre length, cross sectional area and tendon length. However, the evaluation of ultrasound images depends heavily on the expertise of the operator and is time-consuming. Basing parameter estimation on the properties of the image itself and reducing the reliance on the skill of the operator would allow for automation of the process, speeding up parameter estimation and reducing bias in the final outcome. Key barriers to automation are the presence of speckle noise in the images and low image contrast. This hinders the effectiveness of traditional edge detection and segmentation methods necessary for parameter estimation. Therefore, addressing these limitations is considered pivotal to progress in this area.

The aims of this thesis were therefore to develop new methods for the automatic evaluation of these geometric parameters of the upper extremity, and to compare these with manual evaluations. This was done by addressing all stages of the image processing pipeline, and introducing new methods based on artificial intelligence.

Speckle noise of musculoskeletal ultrasound images was reduced by successfully applying local adaptive median filtering and anisotropic diffusion filtering. Furthermore, low contrast of the ultrasound image and video was enhanced by developing a new method based on local fuzzy contrast enhancement. Both steps contributed to improving the quality of musculoskeletal ultrasound images to improve the effectiveness of edge detection methods.

Subsequently, a new edge detection method based on the fuzzy inference system was developed to outline the necessary details of the musculoskeletal ultrasound images after image enhancement. This step allowed automated segmentation to be used to estimate the morphological parameters of muscles and tendons in the upper extremity.

Finally, the automatically estimated geometric parameters, including the thickness and pennation angle of triceps muscle and the cross-sectional area and circumference of the flexor pollicis longus tendon were compared with manually taken measurements from the same ultrasound images.

The results show successful performance of the novel methods in the sample population for the muscles and tendons chosen. A larger dataset would help to make the developed methods more robust and more widely applicable.

Future work should concentrate on using the developed methods of this thesis to evaluate other geometric parameters of the upper and lower extremities such as automatic evaluation of the muscle fascicle length.

ABBREVIATIONS LIST

2D	Two-dimensional
3D	Three-dimensional
ADC	Apparent Diffusion Coefficient
ADF	Anisotropic Diffusion Filter
AME	Logarithmic Michelson Contrast Measure
BNN	Backpropagation Neural Network
CGT	Canny Ground Truth
CL	Convolutional Layers
CMY	Cyan Magenta Yellow
CNN	Convolution Neural Network
CT	Computer Tomography
DBN	Deep Belief Net
DSEM	Delft Shoulder and Elbow Model
DICOM	Digital Imaging and Communications in Medicine
DIP	Digital Image Processing
DLNN	Deep Learning Neural Network
DOF	Degree Of Freedom
DTI	Diffusion Tensor Imaging
EGT	Expert Ground Truth
EME	Measure of Enhancement
EMG	Electromyography
EPI	Enhanced Preservation Index
FA	Fractional Anisotropy
FCL	Fully Connected Layer
FEDM	Fuzzy Edge Detection Method
Fn	False negative
FOM	Pratt's Figure of Merit

Fp	False positive
FPLT	Flexor Policies Longus Tendon
GFCE	Global Fuzzy Contrast Enhancement
GPU	Graphics Processing Unit
HE	Histogram Equalization
HIS	Hue Saturation Intensity
IFS	Intuitionistic Fuzzy Sets
JPEG	Joint Photographic Experts Group
LAMF	Local Adaptive Median Filter
LFCE	Local Fuzzy Contrast Enhancement
LOG	Laplacian of Gaussian operator
MCC	Matthews Correlation Coefficient
MHZ	Megahertz
ML	Max-pooling Layers
MOS	Mean Opinion Score
MPSSI	Mean Preservation Speckle Suppression Index
MRI	Magnetic Resonance Imaging
MUI	Musculoskeletal Ultrasound Imaging
NLUM	Non-Linear Unsharp Masking
PCS	Physiological Cross Section area
PD	Proton Density
RAM	Random Access Memory
RBEM	Reference-Based Edge Measure
RBM	Restricted Boltzmann Machine
RGB	Red Green Blue
SAR	Synthetic Aperture Radar
SD	Standard Deviation
SDAE	Stacked Denoising Auto-Encoder

SDME	Second-Derivative-like Measure of Enhancement
SMPI	Speckle Suppression Mean Preservation Index
SSI	Speckle Suppressions Index
Tn	True negative
Tp	True positive
US	Ultrasonography

LIST OF FIGURES

Figure (2-1) Anterior view of musculoskeletal model of the upper extremity (Holzbaur et al., 2005). 11

Figure (2-2) Interior structure of skeletal muscle, cited from Lieber (2002). 13

Figure (2-3) Different patterns of muscle fibre arrangement in the muscle, cited from Hamill & Knutzen (1995). PCS is physiological cross section area, which can be defined as cross section area, which is perpendicular on the muscle fibre. A illustrates fusiform muscle, while B shows penniform muscle (unipennate, bipennate and multipennate). 14

Figure (2-4) The coordinates of the image plane, the blue line is the detected line by (r, ∅). 36

Figure (2-5) RBM structure, which is adapted from Fischer (2012). 39

Figure (2-6) Simple diagram of CNN, this figure is updated from Cernazanu-glavan, & Holban (2013). 40

Figure (2-7) Pipeline of fuzzy image processing. 42

Figure (3-1) Panoramic ultrasound image of the left shoulder, which was collected from a cadaver. 48

Figure (3-2), this figure from left to right shows image visualization at depth 1.5cm and 7 cm respectively. Figure (b) shows a high level of the musculoskeletal structure information and less resolution, while figure (a) illustrates less musculoskeletal structure information and high resolution. 50

Figure (3-3), this figure from left to right shows collected images at low and high gain respectively. 50

Figure (3-4), the first line of this figure presents ultrasound image at high contrast (dynamic range=36) and its histogram, while the second line illustrates ultrasound image at low contrast (dynamic range=96) and its histogram. 51

Figure (3-5), illustrated collected image and its histogram when frequency=12 MHz, gain=54, depth=4.5 cm and dynamic range=66. 52

Figure (3-6), the left hand of the figure illustrates scanning posterior aspect of the elbow joint at crab position, while the right-hand shows scanning one snapshot ultrasound image of the medial head of the triceps muscle at crab position. 53

Figure (3-7) Longitudinal section scanning of flexor carpi radials tendon. 54

Figure (3-8), the left hand of the figure illustrates scanning one snapshot of flexor pollicis longus tendon (transverse plane), while the right-hand shows scanning of this tendon at longitudinal plane. 55

Figure (4-1) Input ultrasound image (longitudinal section of flexor pollicis longus tendon) is shown in figure (a) and figure (b) illustrates the same image after adding speckle noise. Figure (c) and (d) show input image after adding (salt and pepper) noise and gaussian noise respectively. 61

Figure (4-2) Processing steps of applying LAMF on 3x3 mask (central pixel and its neighbours around the image). 64

Figure (4-3) Musculoskeletal ultrasound image, which was collected from cadaver (right shoulder region). 67

Figure (4-4) Comparison between performance of LAMF and ADF across five iterations when performing on cadaver musculoskeletal ultrasound image and window size is 3x3. 68

Figure (4-5) Cadaver musculoskeletal ultrasound image after applying ADF. 69

Figure (4-6) Cadaver musculoskeletal ultrasound image after applying LAMF. 69

Figure (4-7) Healthy musculoskeletal ultrasound image (triceps ultrasound image). 70

Figure (4-8) Comparison between performance of LAMF and ADF across (1-5) iterations when performing on the healthy sample of the musculoskeletal ultrasound image (triceps muscle) and the size of the window is 3x3. 71

Figure (4-9) Healthy musculoskeletal ultrasound image (triceps ultrasound image after applying ADF is shown in figure (a), while figure (b) illustrates output image after applying LAMF. 71

Figure (4-10) Healthy musculoskeletal ultrasound image (cross section of flexor pollicis longus tendon). 72

Figure (4-11) Comparison between performance of LAMF and ADF across (1-5) iterations when performing on cadaver musculoskeletal ultrasound image. 72

Figure (4-12) Healthy musculoskeletal ultrasound image (cross section of flexor pollicis longus tendon) after applying ADF is shown in figure (a), while figure (b) illustrates output image after applying LAMF. 73

Figure (4-13) Applying LFCE on 3x3 sub-image (central pixel and its neighbours) around the image. Connection between central pixel and its neighbours, which are illustrated in rule 1 and rule 6. In rule1, the central pixel was fed up from brightness membership function, while neighbours pixels are taking from darkness. In case of rule6, the central pixel was fed up from darkness and its neighbours pixels were fed up from grey level membership function. 82

Figure 4-14), illustrates the selection of the best values of the Sd and Se parameters-based on evaluation the maximum value of the SDME. As example, the red square color represents the maximum value of the SDME at (Sd_3,Se_3), so it is possible to extract the figure of (Sd against SDME) when Sd=3 and set of

Se (40 values), also extraction the figure of (Se against SDME) when Se=0.3 and set of Sd (40 values). 84

Figure (4-15) illustrates three membership functions, function in blue color represents darkness membership function, while in red color represents brightness membership function and function in green shows grey membership. 85

Figure (4-16) Representation of central pixel (C_5) and its neighbours (C_1, C_2, C_3, C_4, C_6, C_7, C_8, C_9), fuzzy rules will be applied on C_5 and each neighbour's pixel and then combining together to get the final decision. 85

Figure (4-17) illustrates selection the best value of block size, the dimensions of the input image after cropping to select region of interest are [305,559], and the optimum block size is 151; this means image is divided into 5 blocks and these blocks distributed across two rows (r_1=2) and three columns (r2 = 3). 89

Figure (4-18), the left hand side of this figure illustrates the estimation of Sd and Se and different colors depict the SDME values across different values of Sd and Se, while the right hand side represents illustration of the proper values of Sd and Se at maximum value of SDME in separated figure (Sd=1.4 and Se=25 of sample1).The evaluations of left and right side based on the figure (4-14). 90

Figure (4-19), the first line illustrates input image of sample 1 and this image after applying GFCE (Global Fuzzy Contrast Enhancement technique) and HE respectively, while the second line shows input image after applying NLUM and LFCE respectively. 91

Figure (4-20) illustrates the selection of the block size, but in this figure the value of the entropy represents the mean value of the entropy of four frames (frames 5,50,75,90) in the case of sample 1. The dimensions of the input frame after cropping are [254,271], and the proper block size that was determined is 127; therefore, the number of the rows (r_1) equals 2 and the number of the columns (r2) equals 2. 92

Figure (4-21), the left-hand side of this figure presents the proper values of Sd alongside the video frames (120) of sample1, while the right-hand side illustrates the set of Se parameter after estimation of the same video sample. 92

Figure (4-22) shows estimation of Sd and Se of two frames (46 and 88) of sample 1, different colors depict the SDME values across different values of Sd and Se. Furthermore, the separated figure shows Sd

value of frame 46 (Sd =1.2) and frame 88 (Sd= 2.7) at maximum value of SDME. In terms of evaluation of Se value in frame 46 equals 27, while in frame 88 equals 3 at maximum value of SDME. The evaluations of left and right side based on the figure (4-14). 93

Figure (4-23) Evaluation of SDME for video using LFCE method and GFCE of sample 1. 94

Figure (4-24) Evaluation of SDME for video of different methods of contrast image enhancement (Input, LFCE, HE and NLUM) of sample 1 in the experiment 2. 94

Figure (4-25) In the first line, figure (a, b, and c) from left to right illustrate frame 88 of input video, after applying GFCE, and HE methods on this frame, while the second line (d and e) shows this frame after applying NLUM and LFCE (block's size=127, Se=3 and Sd=2.7)). 95

Figure (4-26) Selection of block size, the dimensions of input image after cropping are [170,772], and the optimum block size is 85; therefore, number of rows (r_1) equals 2 and number of columns (r2) equals 9. 96

Figure (4-27), the left-hand side of this figure illustrates the estimation of Sd and Se and different colors depict the SDME values across different values of Sd and Se, while the right hand side represents illustration of the proper values of Sd and Se at maximum value of SDME in separated figure. So, Sd=3.6 and Se=2 of sample 1. The evaluations of left and right side based on the figure (4-14). 96

Figure (4-28), from top to bottom: the input image from the cadaver is shown in figure (a), while figure (b) shows this image after applying GFCE method. The image in figure (c) shows the result after applying HE, while figure (d) is input image after applying NLUM method. Finally, figure (e) illustrates contrast image enhancement using LFCE method. 97

Figure (5-1) Pipeline, which explains how to get geometric parameters of musculoskeletal system then feed it to the musculoskeletal model. This pipeline includes ultrasound images, which have been recorded from healthy volunteers for image processing (image enhancement, edge detection and analysis). 104

Figure (5-2) Input image of sample1 is illustrated in figure (*a*), while figure(*b*) shows CGT of sample1, it was extracted by using Matlab 8.6. Figure(*c)* shows EGT image, drawn by expert anatomist and figure (*d*) illustrates labeling of figure (*c*). by expert. 107

Figure (5-3) process of data preparation for training and testing. This process depends on labelling input pixels, a random selection of pixels. We can track any pixel, which has been selected based on its saved x-y coordinates and distribute unique pixels between training and testing equally. 108

Figure (5-4), output image from training and testing dataset. 110

Figure (5-5), the left hand side of this figure shows optimization of window size for CGT image, while the right hand side illustrates optimization of window size for EGT image. 113

Figure (5-6) Composite output image produced using the output of the trained and tested CNN, showing the training pixels (in green) and the testing pixels (in red) using the data derived from the EGT image. 114

Figure (5-7) Output image derived by the Canny ground truth image -CNN using sample1 as the input image. 115

Figure (5-8), from top to bottom, Tp, Fp, Tn and Fn of input MUI (sample1). 116

Figure (5-9), the left column from top to bottom illustrates input ultrasound image (sample2), CGT and output image, while the right column shows, input ultrasound image (sample3), CGT and output image. 117

Figure (5-10), from top to bottom, input ultrasound image (sample4), CGT and output image. 117

Figure (5-11) Output image derived by the EGT-CNN using sample1 as the input image. 118

Figure (5-12), from top to bottom, Tp, Fp, Tn and Fn of input MUI (sample1). 118

Figure (5-13), the left column from top to bottom, illustrates input ultrasound image (sample2), EGT and output image, while the right column shows, input ultrasound image (sample3), EGT and output ultrasound image. 119

Figure (5-14), from top to bottom, input ultrasound image (sample4), EGT and output ultrasound image. 119

Figure (5-15) Pipeline of FEDM structure. 127

Figure (5-16) illustrates three membership functions ($\mu_1(i,j)$, $\mu_2(i,j)$ and $\mu_3(i,j)$) in different colors, blue color for first membership function in the case of level 1, red color for level 2 and green color for representation membership function of level 3, where, (Cp_0, Cp_1, Cp_2, and Cp_3) are parameters of these membership functions. 128

Figure (5-17) illustrated plot of SD curve which is calculated from a set of SD values. In this curve the value of SD_k is calculated at m_k =0.5 as example. 129

Figure (5-18) Mask configuration for detection of image's edges. 131

Figure (5-19) Speckle noise reduction on FPLT (sample1), figure (a) and figure (b) represent image before and after enhancement respectively. 133

Figure (5-20), illustrates the plot of the SD curve, where the first cut-off point is 1, which represents the minimum grey level intensity in the input image of the sample 1, the last cut-off is 146, this value represents the maximum grey level intensity in the input image, so we have 145 cut-off points. 134

Figure (5-21) Steps of obtaining proper parameters of membership functions at different levels (level 1, level 2 and level 3). Step 1 was optimization of $m_{k,}$ step 2 was evaluation of SD_k and third step was extraction parameters ($Cp_{0,}$ $Cp_{1,}$ $Cp_{2,}$ and Cp_3). 135

Figure (5-22) shows input image (sample 1), edge detection images at three different levels of information by using fuzzy edge detection method. Level 1 shows background information, and level 3 illustrates the information inside the object (texture information), while level 2 outlines the object shape. 136

Figure (5-23) Edge detection image before and after thinning. 136

Figure (5-24), illustrates the statistically comparison of FEDM and Canny method of experiment 1. 138

Figure (5-25) Example of ultrasound imaging (one snapshot of triceps muscle), which shows fat and subcutaneous tissue layer above the upper aponeurosis. 139

Figure (5-26) Steps of extraction of upper aponeurosis and lower aponeurosis from ultrasound image. 139

Figure (5-27) illustrates the pipeline of performing processing steps of experiment 2, starting from input ultrasound image and denoising as the pre-processing step. Following this step by implementing fuzzy edge detection technique on the image, this step includes plotting SD curve, selecting the best value of m_k, getting parameters (Cp0, Cp1, Cp2 and Cp3) then extraction of three edge detection images. Applying active contour on level 2 to get the binary image then getting the final edge detection image using fuzzy edge detection technique on the binary image. 140

Figure (5-28) illustrates SD curve, the value of $SD_k = SD_{max.}$ 140

Figure (5-29), illustrates the statistically comparison of FEDM and Canny method of experiment 2. 142

Figure (5-30) Input ultrasound image (sample1) without doing denoising processing is shown in figure (a), while figure (b) and (c) represent the result of image after applying fuzzy edge detector and thinning respectively. In figure (c), some artifacts were noticed due to the impact of the noise on the image (see red circles in figure (c)). 142

Figure (5-31), figure (a) represent image after denoising. The result of image after applying Canny edge detector on the image is shown in figure (b), while figure (c), shows using active contour on the image

in figure (b) to extract binary object. Figure (d) demonstrates the difficulty in isolating the boundaries of the tendon at cross-section from its background due to unnecessary information inside the object. 143

Figure (5-32), where figure (a) represents the result of image after denoising and figure (b) presents the image after applying Canny edge detector on the image in figure (a), while figure (c) illustrates image after following steps in the figure (5-26). 143

Figure (6-1), illustrates the framework of automatic method to evaluate some of morphological parameters of musculoskeletal system in the upper limb. 149

Figure (6-2) Brief description of Bland Altman plot. 150

Figure (6-3) Evaluation of cross section area of flexor pollicis longus tendon at transverse plane and one ultrasound image snapshot manually. This area was evaluated in cm^2 by tracing the border of tendon at cross section, so the cross-sectional area is 0.19 cm^2. 152

Figure (6-4) The circumference determination of the flexor pollicis longus tendon at transverse plane (one ultrasound image snapshot) is shown manually. This circumference was evaluated in cm by gathering small straight distances around the cross section of the tendon. The circumference in this evaluation was 1.69 cm 153

Figure (6-5) Steps of the evaluation area and circumference of the FPLT at cross-section. 153

Figure (6-6), a, b and c represent the ultrasound image of sample 17, after applying active contour on this image and extracting binary object. Figure d illustrates the image after speckle noise reduction, while figure e illustrates isolated objects by active contour to achieve binary image in figure f. 155

Figure (6-7), a represents the ultrasound image of sample 17 after speckle noise reduction. The image in figure b shows employing active contour on the edge detection image (resultant image after using FEDM), while figure c depicts the binary object. 155

Figure (6-8), the first line illustrates calculation of cross section area of sample 1 and sample 5 using active contour-based segmentation method, while the second line shows the area calculation of the sample 13. 156

Figure (6-9), a shows input image (sample1) without doing denoising processing. Figure b and figure c represent the result of image after applying fuzzy edge detector and thinning respectively. Active contour was applied on the image in figure c to get the result as shows in figure d and extracted binary

object as shown in figure e. In figure e, some artifacts were noticed due to the impact of the noise on the image (see red circles in figure e). 156
Figure (6-10) Bland-Altman plot of circumference measurements of FPLT in mm. 157
Figure (6-11) Bland-Altman plot of cross-sectional area measurement in $mm^{2.}$ 158
Figure (6-12) presents two different samples, which include subcutaneous tissue layer above the upper aponeurosis of the muscle. 158
Figure (6-13) illustrates a sample of the evaluation of the triceps muscle thickness in one ultrasound image snapshot manually. This sample includes layer of the subcutaneous tissue on the upper aponeurosis. 159
Figure (6-14), shows resulted image after applying fuzzy edge detection method on the image in figure (6-12)b, this image was restricted with subcutaneous tissue layer on the upper aponeurosis of triceps muscle. 160
Figure (6-15) Sample of evaluation of triceps muscle thickness in one ultrasound image snapshot manually. Thickness was evaluated in cm, it is the average of three values: proximal, middle and distal measurement 160
Figure (6-16) illustrates the steps of the thickness evaluation of triceps muscle in one snapshot of the ultrasound imaging. 161
Figure (6-17) illustrates the results at different steps, which ended at thickness evaluation of triceps muscle at three different points (proximal, middle and distal). 162
Figure (6-18) Bland-Altman plot of thickness measurement in mm for 20 volunteers. 163
Figure (6-19) illustrates the difficulty of defining muscle fascicles orientation. 164
Figure (6-20) demonstrates the manual evaluation of the pennation angle of triceps muscle in one snapshot. 165
Figure (6-21) illustrates the steps of pennation angle evaluation of the triceps muscle in one snapshot of ultrasound imaging. 166
Figure (6-22) presents the steps of the pennation angle evaluation of the triceps muscle in one snapshot ultrasound image, the pennation angle is taken as the angle between the aponeurosis and the fibre direction. 167
Figure (6-23) Detection lines in the image, which suffered from subcutaneous tissue layer on the upper aponeurosis of triceps muscle is shown in this figure. 168

Figure (6-24) Detection lines in the image, which suffered from difficulties in defining the orientation of muscle fascicles is illustrated in this figure. 168
Figure (6-25) Bland-Altman plot of pennation angle measurement in degrees for 10 volunteers. 169

LIST OF TABLES

Table (2-1) Comparison of three medical imaging modalities (MRI, DTI and US). 28

Table (4-1) Evaluation of assessment metrics of cadaver musculoskeletal ultrasound image sample 67

Table (4-2) Evaluation of assessment metrics of arm musculoskeletal ultrasound image sample. 70

Table (4-3) Evaluation of assessment metrics of hand musculoskeletal ultrasound image sample. 72

Table (4-4) Equations of three metrics (EME, AME and SDME). 80

Table (4-5) The values of three metrics (EME, AME and SDME) of five samples of musculoskeletal ultrasound image's samples. Image contrast was enhanced using LFCE method and the resultant image of LFCE gives the highest score of SDME and is approximately 34% greater than other GFCE. 91

Table (4-7) The values of three metrics (EME, AME and SDME) of five samples of panoramic musculoskeletal ultrasound image. It is 31% of the LFCE's performance outperforms GFCE's performance. 98

Table (5-1) CNN configuration (13x13) in the case of using CGT, window size =13x13. 113

Table (5-2) CNN configuration (27x27) in the case of using CGT, window size =27x27. 113

Table (5-3) Quantitative assessment of output of MUI). 120

Table (5-4) Quantitative assessment of the 25 healthy samples (Experiment 1). 137

Table (5-5) Quantitative assessment of the 20 healthy samples (Experiment 2). 141

TABLE OF CONTENTS

CHAPTER 1 MOTIVATION AND RESEARCH AIMS 2

1.1 RESEARCH MOTIVATION 2

1.2 THE AIMS OF THE THESIS 5

1.3 THESIS STRUCTURE 5

CHAPTER 2 LITERATURE REVIEW 8

2.1 INTRODUCTION 8

2.2 MUSCULOSKELETAL MODELLING IN MOVEMENT ANALYSIS 9

2.3 MOVEMENT AND BIOMECHANICS OF THE UPPER LIMB 12

2.3.1 Upper limb movement 15

2.4 DETERMINING THE MUSCULOSKELETAL PARAMETERS 16

2.5 MEDICAL IMAGING TOOLS FOR MUSCULOSKELETAL PARAMETERS EXTRACTION 18

2.5.1 Ultrasonography (US) 18

2.5.2 Magnetic Resonance Imaging (MRI) 23

2.5.3 Diffusion Tensor Imaging (DTI) 27

2.6 DIGITAL IMAGE PROCESSING TO IMPROVE PARAMETER DETERMINATION 29

2.6.1 Image Enhancement 30

2.6.1.1 Speckle Noise Reduction 30

2.6.1.2 Contrast Image Enhancement 31

2.6.2 Image Segmentation 32

2.6.3 Image Analysis 34

2.6.3.1 Hough transform 35

2.7 ARTIFICIAL INTELLIGENCE TOOLS TO IMPROVE PARAMETERS EXTRACTION 36

2.7.1 Artificial Intelligence in image processing 37

2.7.1.1 Convolutional Neural Network (CNN) 38

2.7.1.2 Fuzzy Image Processing techniques 41

2.8 SUMMARY 44

CHAPTER 3 COLLECTION OF REFERENCE ULTRASOUND IMAGE DATA FROM CADAVER SPECIMENS AND HEALTHY VOLUNTEERS 47

3.1 INTRODUCTION 47

3.2 ETHICAL APPROVAL 47

3.3 DATA COLLECTION 47

3.3.1 Reference ultrasound image from cadaver specimens 47

3.3.2 Reference ultrasound image from healthy volunteers 48

3.3.2.1 Data collection protocols 52

3.4 SUMMARY: 55

CHAPTER 4 ULTRASOUND IMAGE ENHANCEMENT 58

4 INTRODUCTION 58

4.1 PART 1: SPECKLE NOISE REDUCTION IN THE ULTRASOUND IMAGE 59

4.1.1 Introduction 59

4.1.2 Presence of noise in medical images 59

4.1.3 Filtering to reduce speckle noise 61

4.1.4 No-reference assessment metrics of speckle noise reduction 62

4.1.5 Local Adaptive Median Filter (LAMF) 63

4.1.6 Anisotropic Diffusion Filter (ADF) 65

4.1.7 Implementation and Results 66

4.1.8 Discussion 73

4.1.9 Conclusions 74

4.2 PART 2: CONTRAST ENHANCEMENT IN THE ULTRASOUND IMAGE 75

4.2.1 Introduction 75

4.2.2 Related image contrast enhancement techniques 77

4.2.3 Assessment metrics of contrast image enhancement 79

4.2.4 Local Fuzzy Contrast Enhancement Technique (LFCE) 81

4.2.4.1 Fuzzification 84

4.2.4.2 Generation of fuzzy rules 85

4.2.4.3 Defuzzification 87

4.2.5 Experimental results *88*

4.2.5.1 Experiment 1 88

4.2.5.2 Experiment 2 91

4.2.5.3 Experiment 3 95

4.2.6 Discussion *98*

4.2.7 Conclusions *101*

CHAPTER 5 EDGE DETECTION IN MUSCULOSKELETAL ULTRASOUND IMAGES 103

5.1 PART 1: USING CONVOLUTIONAL NEURAL NETWORK FOR EDGE DETECTION IN MUSCULOSKELETAL ULTRASOUND IMAGES. 105

5.1.1 Introduction *105*

5.1.2 Methods *106*

5.1.2.1 Dataset preparation 106

5.1.2.2 CNN configuration 108

5.1.2.3 Training 109

5.1.2.4 Visualizing output images from training and testing 110

5.1.2.5 Performance measure 110

5.1.2.6 Final Validation using previously unseen MUI 112

5.1.3 Experiments and results *112*

5.1.3.1 Experiment 1 114

5.1.3.2 Experiment 2 117

5.1.4 Discussion *120*

5.1.5 Conclusions *122*

5.2 PART 2: USING FUZZY EDGE DETECTION IMAGE TECHNIQUE IN MUSCULOSKELETAL ULTRASOUND IMAGES. 123

5.2.1 Introduction *123*

5.2.2 Metrics of Edge Measurement based on Reference image *124*

5.2.3 Fuzzy Edge Detection Method (FEDM) *126*

5.2.3.1 Fuzzification 127
5.2.3.2 Application of the fuzzy rules and defuzzification 131
5.2.4 Experiments and Results *133*
5.2.4.1 Experiment 1 133
5.2.4.2 Experiment 2 138
5.2.5 Discussion *144*
5.2.6 Conclusions *145*
CHAPTER 6 ANALYSIS OF THE MUSCULOSKELETAL ULTRASOUND IMAGE 148
6.1 INTRODUCTION 148
6.2 MANUAL MEASUREMENT 148
6.3 AUTOMATIC MEASUREMENT 149
6.4 COMPARISON BETWEEN MANUAL AND AUTOMATIC MEASUREMENTS. 150
6.5 EXPERIMENTS AND RESULTS 151
6.5.1 Experiment 1 ..... *151*
6.5.1.1 Manual measurement 151
6.5.1.2 Automatic measurement 153
6.5.1.3 Comparing between manual and automatic measurements 156
6.5.2 Experiment 2 ..... *158*
6.5.2.1 Manual measurement 160
6.5.2.2 Automatic measurement 161
6.5.2.3 Comparing between manual and automatic measurements 162
6.5.3 Experiment 3 ..... *163*
6.5.3.1 Manual measurement 164
6.5.3.2 Automatic measurement 165
6.5.3.3 Comparing between manual and automatic measurements 168
6.6 DISCUSSION 169
6.7 CONCLUSIONS 171
CHAPTER 7 GENERAL DISCUSSION 173

7.1 SUMMARY OF THE MAIN FINDINGS 173

7.2 DISCUSSION OF THE DISSERTATION RESULTS IN RELATION TO CURRENT ARTICLES 175

7.3 LIMITATIONS 181

CHAPTER 8 CONCLUSIONS AND FUTURE WORK 184

8.1 CONCLUSIONS 184

8.2 FUTURE WORK 185

APPENDICES 205

APPENDIX I 205

APPENDIX II 206

APPENDIX III 207

Chapter One
Motivation and Research Aims

Chapter 1 Motivation and Research Aims

1.1 Research motivation

Disabilities occur in many forms and can be the result of injuries and several diseases, such as cardiovascular diseases, cerebral palsy, stroke, and spinal cord injury. This is more burdensome when upper limbs are affected because it negatively affects daily activities, such as writing, eating and working. Leaving people who have movement impairment without efficient treatment impacts adversely on mobility and the quality of life for both disabled people and those who live closely with them. Hence, there is an urgent need for engineers and designers to analyse this problem and help those in need to restore natural movement or at least support them to be more independent in the movement through the provision of assistive technologies.

The application of movement analysis requires proper comprehension of internal muscle forces and joint reaction forces. Unfortunately, these measurements are impossible to collect directly from patients because they would need internal measurement. Musculoskeletal modelling is a well-established technique for estimation of these variables. Musculoskeletal modelling is a simulation of a biomechanical model that represents the musculoskeletal system. It consists of two main elements: rigid segment (bone) and muscle, muscles connected to bones by tendons, and bones attached to bones by joints. Musculoskeletal modelling has been used for movement analysis and estimation of the internal forces within the musculoskeletal system (Bolsterlee et al., 2013).

The core of musculoskeletal modelling is derived from measurements of the geometric parameters of the musculoskeletal system such as length of the muscle fibre, muscle thickness and tendon length. These parameters describe the architecture of the muscles, and

tendons. Currently, parameters measurement is extracted successfully from cadavers because the cadaveric measurement is a useful tool to see and measure unknown musculoskeletal parameters at the same time. Although cadaveric measurements offer an opportunity for direct estimation of the musculoskeletal parameters, these measurements are unable to provide information about a living individual. Simple scaling of musculoskeletal parameters from cadaver data to fit an individual typically does not result in a suitably personalised model. Therefore, it is necessary to search for more sophisticated solutions (i.e. extracting fundamental information pertinent to musculoskeletal modelling from a living patient instead of a cadaver).

Medical imaging is a powerful tool that has been utilized for visualization of the internal structure of the body, diagnosis and treatment. Over time, several modalities of medical imaging have emerged and developed, and these include Ultrasonography (US), Magnetic Resonance Imaging (MRI), Diffusion Tensor Imaging (DTI) and Computer Tomography (CT) scanning. Each modality has fundamentally different functions and understandably is accompanied by its own set of advantages and disadvantages. For example, MRI and DTI require a strong magnetic field to create an image, whereas US uses ultrasound waves with a frequency greater than human hearing (>20 kHz), which penetrates and reflects through the body. Furthermore, CT scanning depends on radiation and is used for visualising bones rather than soft tissue. US machine is the most flexible medical imaging tool because it is portable, cheap and has a less negative impact on the body relative to other medical imaging approaches. Moreover, real-time static and dynamic scanning is not possible or somewhat tricky when using other medical imaging devices. Importantly, operator experience is critical to enable minimisation of noise and low contrast. Many types of research have been introduced recently to medical imaging modalities as tools to manually extract geometric

parameters of the musculoskeletal system. The primary purpose of this is to acquire the relevant information in vivo in real time from a patient and feed it to musculoskeletal modelling as a step to attain a specific-subject version. However, this approach is time-consuming and depends on the expertise of the medical imaging system operator.

Digital Image Processing (DIP) is a tool that allows the automated performance of a wide variety of image processing operations, such as image enhancement (increases quality of the image), image segmentation (separates the object from its background) and image analysis (extracts image features). The most striking impression gathered in this processing is the close link between all operations. More specifically, image enhancement should be carried out to the highest degree possible in order to achieve the best outcome from image segmentation, while image segmentation is a fundamental prerequisite in image analysis. In this context, digital image processing accelerates and improves extraction of the geometric parameters of the musculoskeletal system owing to its automated nature. Furthermore, DIP is simple in representation and performance. Although digital image processing techniques are efficiently used in medical applications, they are still inadequate for estimation of image features. This is because DIP requires a high execution time and does not have a creativity to address ambiguous data such as medical images. Combining more efficient and robust tools with DIP techniques could improve the level and quality of execution. One possibility is the use of artificial intelligence tools that could support this objective (e.g. fuzzy image processing techniques and convolutional neural network techniques). In this work, traditional DIP methods were combined with artificial intelligence tools to evaluate geometric parameters in the upper extremity automatically. Ultrasound imaging is chosen to visualise the selected internal structure in the upper limb. All automated measurements will be compared with manual measurements based on ultrasound image sample.

1.2 The aims of the thesis

The main aims of the research presented in this thesis are as follows:

1- Develop methods to enhance the quality of the ultrasound images of muscle-tendon architecture automatically. Ultrasound imaging acquires speckle noise due to the behaviour of the image acquisition system in the ultrasound device. Furthermore, many regions in the ultrasound images suffer from a low difference in the illumination. Therefore, decreasing speckle noise in the musculoskeletal ultrasound image and increasing the contrast at low contrast regions in the image will help to achieve this purpose.

2- Develop methods for robust automated analysis, detection and extraction of relevant musculo-tendon parameters from musculoskeletal ultrasound image using digital image processing tools, convolutional neural network and fuzzy image processing techniques.

3- Collect musculoskeletal ultrasound imaging from healthy volunteers (25 subjects) and apply proposed and developed methods to this data. The main purpose of this is the comparison between manual evaluations of the geometric parameters of the collected data with automated measurements.

1.3 Thesis structure

The structure of this thesis mirrors the key steps of the extraction of geometric musculoskeletal parameters and the objectives that were presented in this chapter. **Chapter 2** introduces the main steps of literature review journey, which includes a descriptive review of musculoskeletal modelling, upper limb movements, medical imaging, digital image processing tools and artificial intelligence tools, which are used in processing of the

musculoskeletal ultrasound images and finally main thesis objectives. The next four chapters illustrate the span of the image processing pipeline of this thesis (image acquisition, image enhancement, image segmentation and image analysis). So, the **third chapter** deals with acquisition of the musculoskeletal ultrasound image from ultrasound machines and illustrates the protocols of the manual analysis of collected images. **Chapter 4** focuses on increasing the quality of the ultrasound image and this chapter introduces a solution to reduce speckle noise in ultrasound image and develop a new method to enhance low image contrast. New applications and novel methods are presented in **Chapter 5** to perform detection of the musculoskeletal parameters such as muscle fascicles, muscle border and cross section of the tendon. **Chapter 6** shows the last step of the methodology pipeline, the application of the developed methods to extract geometric parameters from the upper limb automatically and compare these measurements with manual evaluations. General discussion is reported in **Chapter 7**, while **Chapter 8** deals with conclusions and future work.

Chapter Two
Literature Review

Chapter 2 Literature review

2.1 Introduction

Musculoskeletal disorders could result from work-related injury or diseases such as spinal cord injury, stroke and cerebral palsy disease. It has an adverse impact on the quality of life and economy; particularly, in the case of impairment to the upper limb movement because most daily activities require using hands and shoulders. A recent report by the Health and Safety Executive in the UK stated that the overall number of work-related musculoskeletal injury in 2016/2017 was 507,000 (39%) out of 1,299,000 for all work-linked disorders. Upper limbs or neck disorders were the most common illnesses among these employees (45%). The total loss in working days was around 8.9 million days, with an average of 17.6 days wasted for each worker (Health and Safety Executive, 2017). So, there is not only the impact on the activities of the individual's daily life, but there is also an additional financial burden on the national economy.

Analysis of the behaviour of the normal and impaired movement is a necessary step for the treatment and assistance of people who suffer from impairment to upper limb movement. Movement can be described by evaluation of the internal forces, understanding movement control and coordination, predicting functional ability and identifying disorders. However, it is difficult to measure it in-vivo. Modelling of upper limb segments is a non-invasive powerful tool to analyse movement by solving mechanical equations of motion and force prediction. In this analysis, musculoskeletal models use morphological parameters, which describe the musculoskeletal structure. Some of these parameters are muscle fibre length, tendon length and pennation angle. Therefore, morphological parameters of the musculoskeletal structure are the basic building blocks of musculoskeletal modelling.

Cadavers are the first source of these measurements, but it is time consuming, in-vitro and it is appropriate for designing a generic version of a musculoskeletal model. Such generic models may be useful for generalised predictions about musculoskeletal behaviour but are limited when it comes to making predictions about specific interventions in individual patients. Medical imaging tools can be used to extract these parameters in-vivo to create a personalised musculoskeletal model. However, using these modalities consumes time. Furthermore, it is somewhat subjective rather than objective, since medical imaging modalities such as ultrasonography need an expert to extract these measurements manually from ultrasound images.

More objective evaluation of musculoskeletal parameters could be achieved by involving advanced methods such as digital image processing and artificial intelligence tools. Combining these methods could improve estimation of key parameters and achieves superiority in the efficiency and accuracy of the evaluation.

In the next section, literature describing the necessary tools for the manual and automatic parameter evaluation, as well as key background information on human movement and biomechanics will be reviewed. These parameters describe morphological characteristics of the upper limb.

2.2 Musculoskeletal Modelling in movement analysis

Musculoskeletal modelling has received considerable attention by researchers because it plays an important role in movement analysis. Musculoskeletal modelling works as a non-invasive tool not only for movement analysis and prediction of internal forces (reaction of muscles and bones), it also supports engineers in understanding the design of prosthetic devices.

Two main components describe the framework of musculoskeletal modelling: bones and muscles. Bones are represented in the model as rigid bodies which are connected by mechanical articulations (joints), while the representation of the muscles is as actuators. Muscles connect to bones by tendons, which transfer the force from the muscle to the bone to produce movement. Each of these components has a set of the morphological parameters, which describe different anatomical aspects of it, for example in the case of the muscle, some morphological parameters are the length of the muscle fibre, pennation angle and muscle thickness. These parameters affect the amount of force that can be produced by the muscle.

The solid foundation of musculoskeletal modelling is derived from measurement of the morphological parameters of the musculoskeletal system. This data was typically collected from cadavers, then assumed to represent typical individuals; therefore, this version of modelling is called generic musculoskeletal modelling (Veeger et al., 1991; Veeger et al., 1997; Arnold et al., 2010).

Musculoskeletal modelling has been used in dynamic movement analysis of the upper and lower extremity. Some examples of the upper extremity modelling are (Amis et al., 1979); (Brand et al., 1981); (Lieber et al. 1992); (Veeger et al., 1991, 1997); (Wood et al., 1989), (Van der Helm, 1994), (Makhsous et al., 1999), (Holzbaur et al., 2005), (Charlton & Johnson, 2006) and (Ward et al., 2006). All the previous models are generic models, where the muscle parameters in particular have not been customised to an individual. Figure (2-1) shows one example of these models.

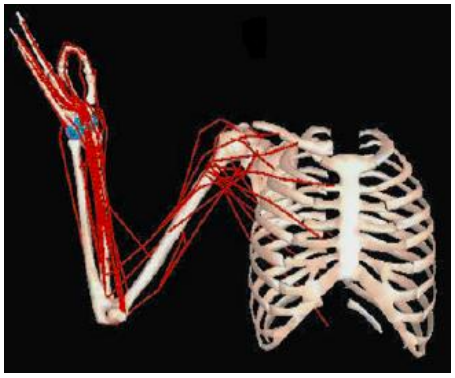

Figure (2-1) Anterior view of musculoskeletal model of the upper extremity (Holzbaur et al., 2005).

The Delft Shoulder and Elbow Model (DSEM) is one example of the musculoskeletal models of the upper limb. An early introduction of DSEM was in 1994 (Van der Helm, 1994). The development of this model has been carried out through alteration of model structure and anatomical data. The software of DSEM offers a potential tool to study and simulate musculoskeletal systems of the upper limb. Musculoskeletal models of the upper limb have been used in specific applications. Firstly, using the musculoskeletal model to understand the biomechanics of the muscle and joint loading on the upper extremity; where the musculoskeletal model was used in the examination of the joint coupling between the shoulder and the elbow (Yu et al.,2011). Also, it is used to assess the stabilising potential of the shoulder muscles (Ackland & Pandy, 2009). Secondly, some musculoskeletal models were used to study and compare shoulder function among different activities, for example, hand cycling (Arnet et al.,2012) and pushing a wheelchair (Veeger. et al.,2002). Another objective is analysing the impact of structural alteration on the shoulder function such as tendon transfer (Magermans et al.,2004) and shoulder implants; this has supported designers in improving shoulder prosthesis (Kontaxis and Johnson, 2009). Furthermore, recent musculoskeletal models were involved in developing the performance of the hand prosthesis

in real time (Blana et al.,2017), and mechanical estimation properties of the arm and shoulder in real time (Chadwick et al.,2014).

As previously stated, generic musculoskeletal modelling is typically based on geometric parameters (muscle volume, tendon length, pennation angle) which are collected from cadavers (Veeger et al., 1991; Veeger et al., 1997; Arnold et al., 2009). The accuracy of cadaver data is restricted by several limitations such as preservation media, accurate dissection and in vitro; in vitro measurements are challenging due to the way of extrapolating and interpretation of the results (Scott 1993; Martin et al., 2001; LaScalza & Gallo, 2002). Therefore, this information is not customized to the geometric parameters of all subjects in the population. Designing musculoskeletal modelling based on the measurement of personal geometric parameters instead of a cadaver is the main target of many researchers nowadays (Blemker et al., 2007). There is much research that has emerged to evaluate these parameters using medical imaging because medical imaging offers a powerful tool for in vivo acquisition data from different subjects of the population (Holzbaur et al., 2007).

2.3 Movement and biomechanics of the upper limb

Movement is the action produced by contraction of groups of muscles (agonists and antagonist). Agonist muscles work as prime movers and contract in the same direction of movement, while the antagonist muscles are opposite muscles to agonists and work to return limb or musculoskeletal parts to the original or resting position. Rationally, it is better to analyse the factors influencing and leading to movement production (Seth et al. 2011). Muscle function and joint action are the two essential parameters, which control movement production. These parameters are affected significantly by the variation of the muscle

architecture, which is typically defined by muscle thickness, length of muscle fibre and pennation angle (Lieber et al., 2002).

Regarding muscle architecture, skeletal muscle consists of bundles of fascicles, which in turn consist of bundles of muscle fibres. Muscle fibres terminate at bundles of myofibrils and a group of sarcomeres arranged on myofibrils. Contraction of skeletal muscle is based on a sliding filament mechanism between actin and myosin on sarcomeres; Figure (2-2) illustrates the organization of the internal structure of skeletal muscle.

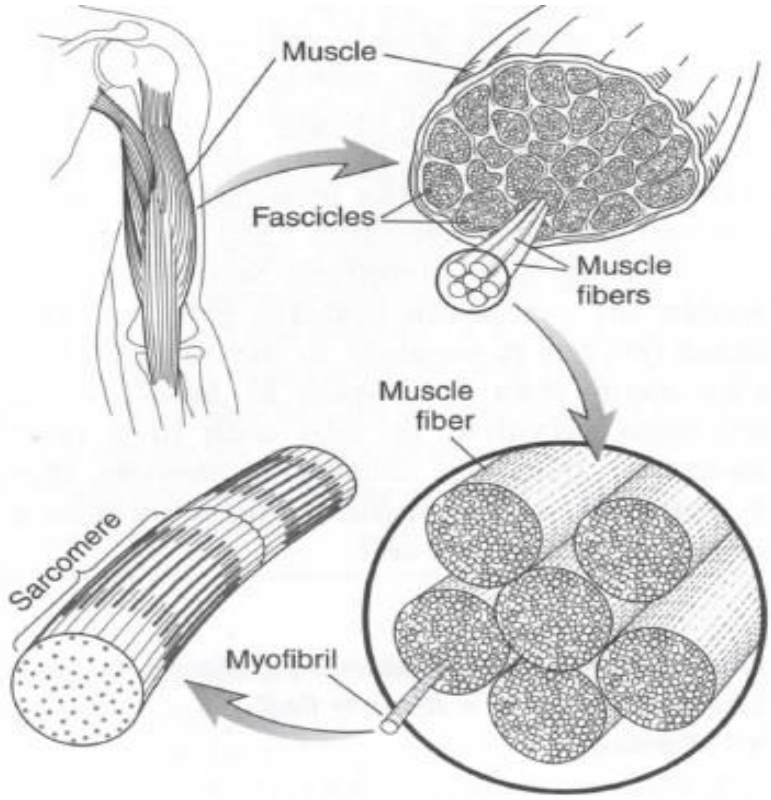

Figure (2-2) Interior structure of skeletal muscle, cited from Lieber (2002).

This will have a considerable effect on the joint excursion or joint rotation (Lieber et al., 2002). Furthermore, there are different arrangement patterns of the muscle fibre in the muscle: muscle fibres approximately extend as a parallel line to muscle aponeurosis between

origin and insertion, this is known as fusiform muscle. On the other hand, muscle with the oblique arrangement of its fibres is known as penniform muscle because it has a pennation angle (an angle between the axis of force generation and the orientation of muscle fibre). Penniform muscle is classified into three types: unipennate, bipennate and multipennate. In the unipennate muscle, the muscle fibres arranged in a diagonal line extending to the tendon, while bipennate muscle includes two diagonal rows similar to a feather shape, in their arrangement. In the case of multipennate muscle, a tendon in the centre has multiple rows of muscle fibres in a diagonal direction are arranged around it and branching out to insert in to more than one tendon. The physiological cross-section (PCS) is defined as the area that cuts all the muscle fibres; it is commonly involved in estimating the number of the fibre of the muscle. Hence pennate muscles have a large number of muscle fibres compared with fusiform muscle; force production is also high in this muscle. Figure (2-3), shows the different kinds of pennate muscle.

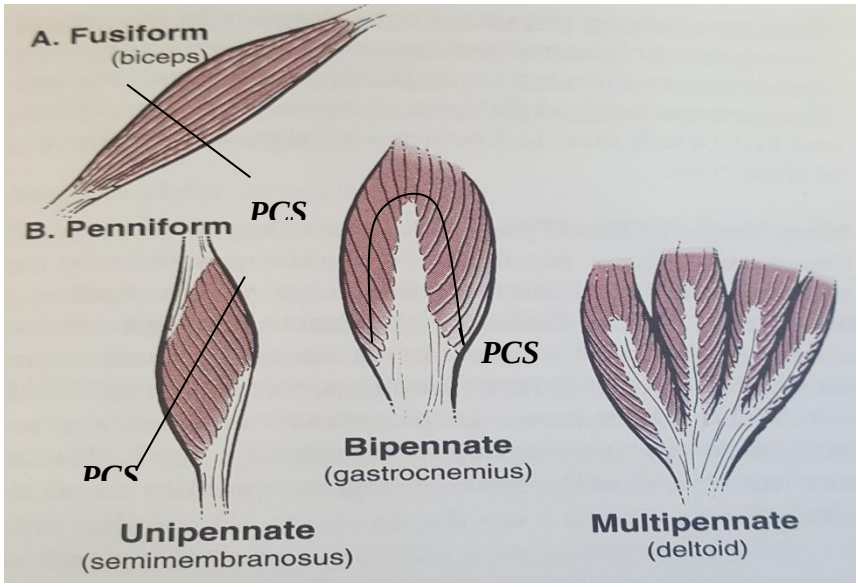

Figure (2-3) Different patterns of muscle fibre arrangement in the muscle, cited from Hamill & Knutzen (1995). PCS is physiological cross section area, which can be defined as cross section area, which is perpendicular on the muscle fibre. A illustrates fusiform muscle, while B shows penniform muscle (unipennate, bipennate and multipennate).

Planning of voluntary movements begins at motor cortex of the cerebral cortex whereas cerebellum work to coordinate these movements. Output signals from the motor cortex pass through the nervous system to stimulate the skeletal muscle to contract and produce force. Then force is transferred to the joint by tendons; a tendon behaves as a bridge between muscle and bone to transfer force. Considering the accurate measurements of the geometric parameters (cross-section area, tendon length and tendon excursion) is necessary to evaluate proper mechanical properties of the tendon. Variation in these mechanical parameters could affect its ability to deliver force to the bone or joint and achieve the movement.

2.3.1 Upper limb movement

The study of the upper limb movement is growing in parallel with the growth of the motives and goals. The primary motivator is the urgent need to help patients to live comfortably. Secondly, aspiring scientists who endorse the idea of robot development as a substitute or a support to humans in the implementation of restrictive and time-consuming tasks. More than one reason illustrates the difficulty of modelling the upper limb. Firstly, the movement system of the upper extremity can be described as complex because upper limb joints have many degrees-of-freedom (DOF) especially the shoulder joint (Rab et al., 2002; Nikooyan et al., 2011). Secondly, the path of the upper extremity muscles is likely to not be a straight line (Rankin & Neptune, 2012). Taking measurements of three-dimensional movement in the upper extremity could be an arduous task, particularly in the case of shoulder movement (Veeger et al., 1997). One of these applications is skin markers of the three-dimensional techniques; the idea was derived from lower limb then applied to analyse the movement of the upper limb. This method presented a promising approach for movement analysis using surface markers. However, to be more applicable and practical, it needs a standard criterion of collecting data to determine the accuracy of movement analysis of the upper extremity.

The upper extremity is typically a composite of four main parts (shoulder, arm, forearm and hand), a hand forms the lightest weight of the upper limb while a shoulder region is the heaviest and a forearm is lighter than an arm. These parts consist of different muscles, bones and joints to perform a variety of upper limb movements such as grabbing, eating, writing, raising weights and dancing. Briefly, bones, which participate in the movement of the upper limb, are clavicle, scapula, humeras, ulna, radius, carpal bones, metacarpal bones and phalanges bones. Joints could consist of combining two or three bones. The three main joints of the upper limb are glenohumeral joint (between the glenoid cavity of the scapula and head of the humerus), the elbow joint (between humerus, radius and ulna) and the wrist joint (between radius and carpus). The DOF in the upper extremity of humans excluding the hand is 7 DOF, which is distributed as follows: shoulder joint has 3 DOF, while each elbow joint and wrist joint has 2 DOF (Rosen et al., 2005; Gopura et al., 2010).

2.4 Determining the musculoskeletal parameters

Two kinds of measurements are involved in the evaluation of morphological parameters of the musculoskeletal system (muscle fibre length, tendon length and pennation angle). The first is a cadaveric measurement using an anthropometric method, while the second uses medical imaging as a tool to extract musculoskeletal parameters from cadavers or healthy volunteers.

The first attempt at cadaveric measurement was in 1967, applied to lower limb specimens to study the mechanical properties of the tendon. The comparison between the human Achilles tendon and the horse tendon was achieved and illustrated the stress-strain curve for both tendons in vitro (Abrahams, 1967). Another comparison of mechanical properties of the Achilles tendon and other tendons was verified in humans (Wren et al., 2001). Studies have

illustrated the validation of the lower limb model to assess different movement parameters such as moment arm and tendon length. This model relied on cadaveric data, taken from 21 specimens (Arnold et al., 2010). Another study also based on cadaveric measurement shows the decline in the cross section of the flexor digitorium in feet with claw toes compared with rectus toes (Locke et al., 2010). Estimation of geometric parameters to build an appropriate upper limb model was introduced (Veeger et al., 1997). These parameters have been evaluated based on anthropometric methods after dissecting specimens of the upper limb were taken from five cadavers.

Medical imaging has revolutionized visualization of the internal structure of the body in real time and in vivo. It is worth using medical imaging because it is impossible to imagine in real time what is inside the body unless surgery is performed; it is possible to see internal structure through cadaver dissection, but not in vivo. There are several kinds of medical imaging tools, which have been used in musculoskeletal system analysis such as Ultrasonography (US), Magnetic Resonance Imaging (MRI), Diffusion Tensor Imaging (DTI) and Computer Tomography (CT) scans. Researchers have stepped up their efforts recently to focus on using these modalities in musculoskeletal applications. For example, using ultrasound imaging (Martin et al., 2001; Heinz, 2016). and MRI (Scott et al., 1993) in the identification of musculoskeletal parameters from a cadaver. Furthermore, combining the musculoskeletal model with MRI to determine moment arm and comparing it with experimental data (Arnold et al., 2000) is used. The result shows the difference between the two measurements was reduced to 10% when combing MRI with musculoskeletal model.

On the other hand, accurate evaluation of these parameters from a cadaver whether they are collected using an anthropometric method or using medical imaging tools has some limitations. Examples of these limitations are: the impact of the preservation media on the

vitality of cadaver tissue, mobility of this tissue compared with the living tissue of a healthy volunteer and the accuracy of the dissection procedure (Scott 1993; Martin et al., 2001; LaScalza & Gallo, 2002).

2.5 Medical Imaging tools for musculoskeletal parameters extraction

Medical imaging consists of different imaging devices which are used in musculoskeletal visualisation system to help clinicians to make their decision on the diagnosis and support researchers in the investigation. The importance of medical imaging tools in developing musculoskeletal modelling links directly with an increase in the possibility of the musculoskeletal parameters evaluation based on using these tools.

Medical imaging tools such as MRI, DTI and US are free from radiation and assist in the visualisation of the soft tissue rather than bone. Therefore, it is suitable for identifying the details of muscle and tendon. However, each modality has pros and cons in terms of the details recognition. For example, MRI is powerful enough tool to depict muscle and tendon borders, but it does not provide a good enough view to describe muscle details, while the US does have potential for identification of muscle details such as fibre orientation. DTI has a promising ability to recognise the direction of muscle fibre and could be a powerful modality, which will be used in the future for high-level visualisation of details in muscles and tendons. On the other hand, CT scans are a suitable choice for visualisation of bones rather than soft tissue, but it depends on radiation which has some restrictions on scanning.

2.5.1 Ultrasonography (US)

Principle

Ultrasonography relies on transmissions of the ultrasound wave (frequency 1-20 MHz) through the body (Narouze, 2011). Some of these beams could be scattered as noise, while

other beams could be converted to heat, which is absorbed by the body. The reflected beams are detected by an ultrasound probe or transducer, which translates the reflected signal into an image. Linear and curvilinear transducers are two familiar probes, which are used in musculoskeletal applications. The selection of a suitable probe depends on where the scan, size, and the depth of the musculoskeletal components are. In the case of scanning a superficial muscle, a linear probe is a preferable choice because the linear probe works with high frequency (7-20MHz). The low frequency< 7 MHz of a curvilinear probe is used to visualize the deep structure of the body (Louis, 2008).

There are three modes of the ultrasound machine scanning: A mode, B mode and M mode. A mode (amplitude mode) concerns with displaying the amplitude of an ultrasound signal, while B mode (brightness mode) displays the ultrasound echoes as bright dots to illustrate two-dimensional ultrasound image. Lastly, M mode is motion mode, which is used to analyse moving body parts such as cardiac and fetal cardiac imaging. The ultrasound mode most commonly used in the visualization of musculoskeletal structure is B-mode (Lin et al., 2000; Ahmed & Nazarian, 2010) because this mode translates the ultrasound echo of the musculoskeletal structure to two-dimensional ultrasound image.

Change in the angles of the ultrasound beam makes a massive difference on the fidelity of the image, for example, ultrasound images could be brighter than other images if the ultrasound beam was perpendicular to the tendon (Lew et al., 2007). Therefore, holding a probe in the wrong way and not using adequate pressure during scanning will lead to inaccurate information (Ihnatsenka & Boezaart, 2010). If an angle between a probe and a skin is not perpendicular, this leads to produce artifact called anisotropy. This kind of artifact is direction dependant and commonly occurs in tendons due to the structural nature of the tendon which contains multiple, parallel linear interfaces (Narouze, 2011). However, to

reduce the impact of the anisotropy, it is better to use a linear transducer because it has a higher possibility of being mostly perpendicular to the surface of the body.

The measurement of ultrasound imaging has inter-observer and intra-observer variability; inter-observer due to the different views in the measurement of the same scan region between different experts. The same expert could give a different view when scanning the same region at a different time, this is intra-observer. It is possible to avoid this variability and get an acceptable agreement regarding views by getting more practice on measurement protocols. Acoustic impedance is different from one tissue to another; it indicates the amount of echo, which is reflected from tissue depending on the density, for example, the acoustic impedance of the bone is larger than a muscle (Chan & Perlas, 2011). Consequently, the expertise is the main requirement to get a meticulous image and avoid some of the expected errors.

Development

Ultrasonography has become a more popular imaging modality than ever, not only is it free from ionizing radiation and magnetic fields that restricted the patient who has a pacemaker, but also it is a cost-effective solution and portable as well. In addition, imaging via US machine is in real time, non-invasive and interestingly with dynamic and static scanning. Ultrasonography has been utilised in the medical applications for more than 70 years (Kane et al., 2004). Indeed, Ultrasonography has had several applications in the musculoskeletal system during four decades of the development. In the first two decades, researchers concentrated their efforts in trying to solve issues related to musculoskeletal diseases, and analysis of which has an impact on muscle architecture. The first article, published in 1980 about the investigation of congenital dislocation in an infant hip joint (Graf, 1980). The US was used as a supportive tool in observation of shoulder dislocation (Gompels & Darlington,

1981). Furthermore, evaluation of the changes in the pennation angle of the brachialis muscle resulting from variation of the elbow joint angle and torque during a static and dynamic condition in vivo (Herbert & Gandevia, 1995). Perhaps, gravity has an impact on the measurement in the vertical or horizontal directions, Li &Tong. (2005) executed the same experiment and found different results from Herbert due to this reason. Changes in moment arm were estimated for the Achilles tendon in the joint contraction and relaxation (Maganaris et al., 1998).

Perhaps, a comparison decade is a convenient term to describe the 2000's decade because in this period researchers began to show the difference and similarities between different ways of measurements, different muscles and different sexes. Some of these applications are the comparison of morphological parameters of the muscles in the lower limb between cadavers and volunteers (Martin et al., 2001). Experiments combining US and Electromyography (EMG) measurements to extrapolate the influence on the muscle architecture during muscle contraction and rest have been done for the upper and lower limbs (Hodges et al., 2003). Appraisal of muscle size (Reeves et al., 2004) and muscle mass was performed by US (Sanada & Kearns, 2006) as an alternative method instead of MRI. Prediction of muscle volume of the cadaver was made before dissection (Infantolino et al., 2007). Furthermore, US estimation for morphological characteristics of extensor digitorium muscles to a group of male and female volunteers was performed, also force was measured to the same group and in the same time to illustrate the impact of the change of the muscle properties relative to the change of force (Brorsson et al., 2008).

The fourth decade is a motion decade; researchers have been interested in estimating tendon excursion and analysis of the mechanical properties of the tendon and muscle. Excursion of the finger tendon evaluated manually for cadaveric specimens and in vivo (Korstanje et al.,

2010), described the relationship between stress and strain of the tendon in the lower limb (Gerus & Berton, 2011). Moreover, determination of the thickness of the lower trapezius muscle (Han et al., 2013), and recognition of tendon and muscle tears is possible with dynamic imaging (imaging during movement) (Tandon et al., 2013). Estimating muscle morphological information using US of the rectus femoris and vastus lateral muscles in the lower limb before and after electrical stimulation was performed to observe the difference in the ultrasound images. (Chauhan et al., 2013).

Recently, Sonoelastography has emerged as a development of US to measure mechanical properties of the tendon tissue. It has several applications in the musculoskeletal system, for example, the effect of the change in the mechanical tendon properties on B-mode ultrasound intensity has been demonstrated in vitro (Duenwald et al., 2011). A satisfactory estimation of the displacement and the strain of the tendon tissue has been achieved using two-dimensional Sonoelastography in vivo (Slane & Thelen, 2014). Although Sonoelastography has offered a new way to understand mechanical properties of the tendon tissue through the movement or musculoskeletal myopathy, it is still an inactive method in clinical utility (Smajlovic et al., 2011; Bey & Derwin, 2012). Sonoelastography has several challenges, one of them is consuming time because it needs to measure a broad set of data; secondly, the results are nonlinear due to tendon tissue heterogeneity. Finally, the compression on the surface of the scanning might have a negative impact in focusing on the evaluation of the mechanical properties (Duenwald et al., 2011).

Challenge and limitations

The panoramic image added a new evolution in ultrasound imaging applications because it presented ultrasound images in a wide view. In the panoramic technique, the transducer collects the panoramic image as a sequence of frames, where it can keep the old frame and

continue to add newly scanned frames to the previous one. All scanned frames are parallel to the direction of scan plane to elongate the view of imaging (Kremkau, 2010). It is a powerful way for imaging a whole muscle in one long image (Pillen, 2010). It is approaching use in CT scans in the estimation of the cross-section of the quadriceps muscle (Nooroiv et al., 2010), and gastrocnemius size in the lower limb (Rosenberg et al., 2014), as is the similarity of panoramic US technique to MRI in evaluation of the cross-section area in the lower extremity (Scott et al., 2012).

Although amenability of US has attracted patients and clinicians compared with other medical imaging devices, it still involves some challenges. Some of them have been addressed and others are still under research. US imaging has not had zero risks because the presence of thermal effect during visualisation, although this is very low. Furthermore, calibration is necessary because the data is not the same in all US machines; mapping equations have been designed to apply the calibration between US machines (Blum et al., 2009).

Consequently, ultrasound imaging is a powerful option to extract musculoskeletal parameters automatically. Since, it is portable, flexible, cheap and interestingly provides high-level of the muscle details such as orientation of muscle fascicles.

2.5.2 Magnetic Resonance Imaging (MRI)

Principle

MRI is one of the medical imaging methods which produced a paradigm shift in medical diagnosis because it is powerful in discrimination between normal and abnormal soft tissues. There are five main components of MRI, contributing with each other to achieve the work. The first one is a magnet that produces a static magnetic field; while the second is the

magnetic gradient system (variant magnetic field). Radio frequency and coil system represent the third part; the resonance occurs between radio frequency and frequency of the selected region for imaging. Finally, the fourth and fifth parts are receiver and computer system respectively. The fundamental principle of MRI comes from the idea of polarization of hydrogen protons of water molecules; this means protons are arranged in parallel and antiparallel alignment under the effect of the magnetic field. Thus, the quality of the output image depends on the amount of water molecules in the body. Then, at resonance, protons are excited to store energy by moving it to antiparallel alignment instead of parallel alignment. In the relaxation stage, there are two essential parameters T1 (the time required for proton to go back into the previous position) and T2 (the lifetime of the echo signal), which have a huge impact on the image contrast. Proton Density (PD) is another contrast factor, which also has a clear imprint on the image contrast. The value of PD is varied based on the region of the body. In addition, selection of the thickness slice is critical because it has an enormous effect on the resolution (Westbrook, 2010; Hashemi et al., 2010).

Development

Many researchers are attracted to using MRI in the visualization of the musculoskeletal system, for it being renewed and an effective environment for research and development. The initial idea was introduced in 1971 (Damadian, 1971) and then applied on the rat to detect tumours in 1974 (Damadian et al., 1974). Visualization of all of the human body was done in 1980. The MRI became three- dimensional (3D) in 1981, but it needed a lot of time to complete the scanning process (Ai et al., 2012). After modification of 3D MRI by using parallel imaging, it was possible to use more flexible 3D MRI than previously. The first application of 3D MRI in the musculoskeletal system came after amendments in 1986, it was visualization a knee joint from volunteers and cadavers. The amendments focused on

production a high-resolution of the image compared with the previous one (Harm & Muschler, 1986). In the same year, the first article was published about visualization regions in the upper extremity (hand and wrist), by passing a patient through a high strength magnetic field of 1.5 T (Weiss et al., 1986). Highlighting the capabilities of the magnetic resonance in the description of the muscles, joints, ligaments and tendons anatomically. MRI is a potential modality because it is effective in being able to browse anatomical structure and observe abnormality.

Regarding upper extremity, there are several applications; firstly, visualisation of the anatomical structure of the shoulder (Neumann, 1992) and the ability to differentiate between the normal shoulder and abnormal (Cook et al., 2011; Chaudhary & Aneja, 2012) were introduced. Secondly, illustrations of the anatomy of the elbow joint (Flower & Chung, 2004) and appraisal of the joint status by investigating the function ligament injuries were applied based on MRI (Kaplan & Potter, 2004). Another application was a depiction of the muscles, ligaments and joints, which are related to wrist and hand (Yu, & Habib, 2004). Furthermore, MRI has a distinct role in recognition of the musculoskeletal diseases such as inflammation of the joints (Heron, 1992; Mcqueen, 2000). In addition, MRI is valid in the observation of musculoskeletal diseases after treatment such as detection of Vitamin D deficiency because these diseases lead to changes in muscle architecture or muscle weakness, so it is possible to observe easily through imaging the cross section of the skeletal muscle (Bignotte et al., 2014). MRI is a powerful tool in the analysis of the morphological properties of the muscle and tendon. Evaluation of the tendon length and moment arm values were achieved for three lower limb cadavers using MRI and a musculoskeletal model (Arnold et al., 2000).

Challenge and limitation

Clinicians and researchers have united to develop MRI for motion analysis; it is possible to scan musculoskeletal system in vivo and in real time by using dynamic MRI. The development of MRI device is going on firmly and the possibility of dynamic imaging using MRI is not just a dream, but it is reality. So far, there are three types of dynamic MRI: kinematic MRI (Shellock et al., 1991), real-time MRI (Quick et al., 2002) and cine phase-contrast MRI (Asakawa et al., 2003). However, these types of MRI have introduced further problems and their development has some limitations. Kinematic MRI technique was developed to recognize certain pathologic conditions during active motion during a very limited time. In the case of cine phase-contrast MRI, there is a difficulty in capturing an image in all cycles because it is possible to depict the image in one cycle and miss other cycles. Repetition is required to achieve a sufficient resolution; but this adds another limitation to this type of MRI, which could exhaust the body especially in the case of disabled people. On the other hand, real-time MRI can perform visualisation in a single cycle without repetition. However, it has insufficient accuracy compared to cine phase-contrast MRI. The movement evaluation by dynamic MRI has remained restricted to just a few movements compared to dynamic applications of ultrasonography.

The second limitation is related to low image contrast. However, it is now possible to improve image contrast by increasing the strength of the magnetic field, because the strength of the magnetic field has a significant impact on the replication of the protons in the parallel direction. Researchers have invested in the previous point to raise contrast properties, particularly in three dimensions MRI. Some of these amendments are from passing patients through the higher strength field instead of the low strength field, enhancement of the magnetic gradient performance and modification to the coils system of MRI into high-

resolution multichannel coils (Naraghi & White, 2012), but at the same time this solution is costly. Other limitations are associated with patients that have an implanted cardiac prostheses (pacemaker). It is important to be aware of this fact because it has a harmful effect on the patient (Baikoussis et al., 2011). The most important limitations of using MRI in the musculoskeletal visualisation system are that it is time-consuming due to repetition; it might exhaust patients; especially elderly and disabled people and it is also expensive.

2.5.3 Diffusion Tensor Imaging (DTI)

The main idea of the image construction using DTI is based on the understanding of motion and distribution of the hydrogen atoms in water molecules within soft tissue. The collision of the water molecules leads to diffusion; the diffusion is anisotropic because it is non-identical in all directions. If the image is constructed based on anisotropic diffusion, the contrast of the image will be increased; therefore, it is possible to tackle the contrast limitation of the MRI. There are three parameters to be considered in DTI structure. The first parameter is eigenvectors and eigenvalues, which describe the physical properties of the materials; for example, the largest eigenvector indicates the main diffusion direction, which corresponds to the fibre direction. The second one is Apparent Diffusion Coefficient (ADC) that illustrates the direction of the diffusion measurement; a bright image has high ADC. Lastly, FA (Fractional Anisotropy) describes the shape of the diffusion (Mori & Zhang, 2006; Hagmanm et al., 2006).

There are several applications of using DTI in the musculoskeletal system: examining the validity of DTI in tracking skeletal muscle fibres at three dimensions for the animal leg (Heemskerk et al., 2005) and human (Heemskerk et al., 2010). Tracking of muscle fibre illustrates a reasonable idea about fibres orientation, and this could be useful in observing

the progress in musculoskeletal diseases. However, DTI is still as time-consuming as MRI even in tracking muscle fibres and it is expensive. Table (2-1), illustrates the comparison between three main medical imaging tools (US, MRI and DTI).

Table (2-1) Comparison of three medical imaging modalities (MRI, DTI and US).

	MRI	DTI	US
1	Expensive	Expensive	Cheap
2	Non-portable	Non-portable	Portable
3	Static and very limited dynamic scanning	Static and very limited dynamic scanning	Static and dynamic scanning
4	High image contrast	Has higher image contrast than MRI	Low image contrast and it has speckle noise
5	Time consuming	Time consuming	Flexible and not time consuming
6	Although it is free from radiation, it is very restricted to the people, who have metal inside a body such as a pacemaker. Furthermore, it is challenging to the people who, cannot cope with high level of magnetic field strength.	The same case of MRI.	Free from magnetic field and radiation. Furthermore, it is not restricted to any kind of implanted metal inside the body.
7	It is possible to recognise muscles and tendons borders, but it is difficult to illustrate the details of the muscle architecture such as orientation of muscle fibres and pennation angles.	It has been involved to reconstruct the orientation of muscle fibres, but it still in early stage yet.	It is possible to present the borders of the muscles and tendons, also the details of the muscle architecture.
8	It is not practical in case of the repetition because it is costly and may exhaust patients especially elderly and disable people.	The same case of MRI.	It is potential in the case of the repetition. However, an expert needs a considerable experience to avoid intraobserver variability.

Based on conclusions of the table (2-1), US was selected in this thesis as a medical imaging tool for collecting data from the upper limb. Ultrasonography is flexible in use, portable, inexpensive and powerful in illustrating muscles and tendons details. Furthermore, US is available to researchers and clinicians at Keele University and is likely to be routinely available to clinicians in practice, thus making the findings of this thesis widely applicable.

2.6 Digital Image Processing to improve parameter determination

Analysing the digital image by computer automatically using a set of processing actions is called Digital Image Processing (DIP). This processing is concerned with improving the appearance of the digital image, separation of the object from background inside the image and image analysis. DIP introduces a faster evaluation of the geometric parameters of the ultrasound image automatically rather than by manual evaluation. Manual measurement of the image parameters is the most common approach in the research. However, it includes a high level of variability because it depends mostly on the machine performance and the expertise of a user. Furthermore, it is time-consuming and perhaps gives a different result upon repeating measurements. Therefore, DIP could improve parameter determination of the musculoskeletal ultrasound image.

There are two methods of digital image display, two-dimensional (2D) image and three-dimensional (3D) image. An image measurement unit is a pixel when measuring a 2D image and a 3D image can be measured by a voxel. Image histogram is a tool that illustrates the distribution of the pixels in terms of the grey level intensities. There are three types of images; the first one is a binary image, which has an intensity value of either 1 or 0. Secondly, the grey level intensities image; the common storage capacity per pixel in this image is 8 bits, so intensity values range between 0 and 256 (Gonzalez & Woods, 2002). Finally, colour image has a specific model which consists of three bands, every band represents one colour such as Red Green Blue (RGB) colour model and Hue Saturation Lightness (HSL) colour model. The intensity value of the colour image is obtained from the union of three components. Mostly, RGB colour model is the dominant model because RGB colour model reflects the colours of the nature, a mixture of red, green and blue. (Wen & Chou, 2004), the Musculoskeletal ultrasound image can read it by Matlab software as a

colour image (RGB colour model), but red, green and blue components are the same grey level intensities.

In fact, two considerable problems are detected in the ultrasound images: low image contrast and presence of speckle noise (Wagner, R.F. et al., 1983). It is difficult to analyse musculoskeletal ultrasound image and obtain required information directly without performing pre-processing steps such as image enhancement (reducing speckle noise and enhancing low image contrast) and image segmentation (detection important details of the image). Furthermore, sometimes post-processing is also necessary to get accurate evaluations.

2.6.1 Image Enhancement

The main objective of the image enhancement is getting a suitable and improved appearance of the image for applications such as edge detection of the image and musculoskeletal parameters determination. There are two considered approaches to achieve this objective: spatial domain approach using traditional methods and transform domain approach using artificial intelligence tools such as artificial neural network and fuzzy logic techniques. Speckle noise and low image contrast are two dilemmas that have a negative impact on the quality of the ultrasound image.

2.6.1.1 Speckle Noise Reduction

Noise reduction is one of the primary targets of musculoskeletal ultrasound imaging because noise in the ultrasound image could add difficulty in interpretation of the image for clinicians and researchers. Speckle noise is multiplicative noise and it is the outcome of the coherence of the acquisition devices. This noise is the dominant noise in several kinds of images such

as Synthetic Aperture Radar (SAR) images and ultrasound images (Wagner, R.F. et al., 1983.), (Dainty, J., 1970). The following equation illustrates the state of speckle noise

$$I(x,y) = G(x,y).S(x,y) \quad (1)$$

Where x and y are the dimensions of input image $I(x,y)$ and this image is observed image with speckle noise, $G(x,y)$ is pure image and $S(x,y)$ is speckle noise (multiplicative noise). Several techniques in DIP have been involved in suppressing speckle noise. Some of these techniques are linear filters such as Wiener filter, but in this type of filter there is a need to convert multiplicative noise into additive noise using the logarithmic function because the linear filter is more appropriate for additive noise. Non-linear filters are another approach of speckle noise suppression (Lee et al., 1994), (Schulze and Wu, 1997); for example: median filter, adaptive filter, anisotropic diffusion filter, local adaptive median filter and wavelet technique. These techniques have been applied to the ultrasound images of different organs in the human body. For instance, using an anisotropic diffusion filter to reduce speckle noise in kidney and heart ultrasound images (Abd-Elmoniem et al., 2002) and liver ultrasound image (Krissian, K. et al., 2007). Another example is using wavelet transform technique in the speckle noise reduction of the ultrasound image of women's breasts (Zhang, J. et al., 2016). The wavelet transform technique can decompose an image to a set of components, then perform particular processing and compose again to get the output image.

2.6.1.2 Contrast Image Enhancement

Contrast enhancement illustrates a significant indicator of the visual image quality enhancement because it shows the difference in the image luminance and brightness between pixels or image regions. There are many traditional techniques in DIP that were applied to improve the contrast of the image; firstly, the Histogram Equalization(HE) method has the

effect of increasing the contrast of image regions that would otherwise have low contrast (Cheng & Shi, 2004; Han et al., 2011; Kaur & Gupta, 2012). But a drawback is that it can increase contrast of noisy regions as well. Secondly, Non-Linear Unsharp Masking (NLUM), is a successful approach because it combines nonlinear filters and logical operations between input image and the image after filtering. It was used to enhance the contrast of the 2D image (Ramponi et al., 1996; Polesel et al., 2000; Deng, 2011) and 3D image (Tao et al., 2009). It is powerful technique in illustrating important information on the medical image, but one of its drawbacks is that it can intensify noise and increase image contrast in all regions even if some regions do not need contrast enhancement.

Image restoration is a part of image enhancement; it has a significant role in retrieving the lost information especially in ultrasound images. Sometimes, image enhancement is carried out as a pre-processing step before image segmentation, this helps to obtain better results of the separation of the object from its background (Gupta et al.,2014).

2.6.2 Image Segmentation

Labelling homogenous pixels into groups to separate the object from the background, classifying an image into regions and highlighting the important details in the image are objectives of defined image segmentation. Computer vision and digital image processing offer many techniques to achieve these purposes. Some of them involve edge detection using image filters, active contour-based segmentation and thresholding.

The main means of edge detection is identifying areas of considerable change in image intensity (1986). This means focusing on highlighting distinct details and ignoring homogeneous details (Joshi et al., 2013). Edge detection can be extracted by using derivative methods of the first order, such as Roberts, Sobel, Prewitt and Canny operators and second

derivative methods such as Laplacian or Gaussian operator (LOG) (Canny, 1986). These traditional methods can be implemented by the convolution between each pixel, and its neighbours in the image and kernel, this kernel may have a window size of 3x3, 5x5, 7x7 or larger window.

Another familiar method in image processing is thresholding. This method can separate the image into regions based on selected image intensity (Gonzalez & Woods, 2002), see equation (2).

$$Output\_image(i,j) = \begin{cases} region_1 & if\ 0 \le I(i,j) \le threshold_1 \\ region_2 & if\ threshold_1 \le I(i,j) \le threshold_2 \\ & \dots \\ region_n & if\ threshold_{n-1} \le I(i,j) \le threshold_n \end{cases} \quad (2)$$

It is possible to extract several regions from input image based on the selected threshold. Several different methods for edge detection have been utilised on Musculoskeletal Ultrasound Imaging (MUI). One of the preliminary works in MUI segmentation was introduced by Gupta (Gupta et al., 2014). This technique addressed limitations related to MUI such as speckle noise reduction and contrast enhancement before detection of the edges of the image. Furthermore, subsequent steps were involved in morphological processing such as erosion and dilation to eliminate distorted pixels and facilitate extraction of the main features, which describes an object in the image. Extraction of image features (edges) was achieved by using a curvelet transform; this method is designed to represent an image in the high-level dimensions (large scale and different angles), so it is suitable to extract the edge. Then using the thresholding method to separate the object from its background. In this work, automatic segmentation was expected to support the analysis of the MUI, but the details of the muscle edges of the ultrasound images were not well preserved due to the impact of the dilation and erosion processing on changing some details of the image.

The active contour method was presented by Chan and Vese (Chan & Vese, 2001) as one of the powerful tools of separating an object from its background in the image. Active contour does not need to define the edge or remove noise when evaluating the contour of the object. It is commonly involved in snaking (Kass et al., 1988) and surface segmentation (Krueger et al., 2008). Some applications of ultrasound images used active contour to detect an object in different organs of the body; for example, the ultrasound image of a thyroid (Poudel et al., 2016), carotid artery (Chaudhry et al., 2013) and vein (Petroudi et al., 2012). From these applications active contour-based segmentation illustrates that is possible to successfully separate an object from its background without first defining edges. However, this is also depending on the properties of the image. For example, musculoskeletal ultrasound images have a complex texture patterns compared with other medical images. Therefore, it might be difficult to apply this method on MUI without performing pre-processing steps.

2.6.3 Image Analysis

Image analysis includes identifying the main parameters and properties of the image such as determining the colour properties of the different regions in the image, geometric evaluation of the properties of the object inside the image (area, diameter and length) and feature extraction of the image. Image analysis is the last stage in the image processing pipeline and could require pre-processing steps and tools particularly in the case of the analysis of medical images. For example, musculoskeletal ultrasound images need image enhancement to increase image quality by reducing speckle noise and raising the contrast of the regions, which have low contrast. Furthermore, sometimes segmentation or edge detection is a necessary step with image enhancement and works as a pre-processing step. Indeed, musculoskeletal ultrasound imaging analysis is more challenging compared with other medical images and other ultrasound images. This is due to the interaction between grey

level intensities of the image; it is possible to detect pixels that have the same grey level intensities in the tendon and the muscle as an example. Several types of research have recently analysed the ultrasound imaging of the muscle and bones using DIP techniques. This is for determining geometric parameters, which describe the behaviour of the muscles, tendons and movement system automatically without biasing. Some of this work is evaluation of the pennation angle of gastrocnemius muscles (Zhou & Zheng, 2015) and vastus-lateralis in real time (Jalborg, 2016); edge detection in this application was achieved as a pre-processing step using edge detection filters such as Canny edge detector, Sobel edge detector and Hough transform method. However, the superiority in the extraction of musculoskeletal parameters can be achieved by combining artificial intelligent tools with DIP techniques rather than only traditional DIP tools. Therefore, this would help to improve the performance of the automatic approach and offer an array of benefits in terms of accuracy and speeding up the algorithms.

2.6.3.1 Hough transform

The Hough transform is a technique that has been used to detect lines, circles and curves. This tool was originally introduced by Hough (1962) and developed by Duda and Hart (1972). This method requires a pre-processing step; applying edge detection method on the image to get a set of edge detector pixels. If the edge detection image plane has a straight line, each point in this straight line will have the possibility of passing lines through this point. This line can be represented by the equation (3):-

$$x_1 \cos(\emptyset) + y_1 \sin(\emptyset) = r \qquad (3)$$

where (x_1,y_1) is a point on the line. The line is determined using two parameters: radius (r) that is defined by the distance from the coordinate system center towards the line, and theta (Ø), the angle between the radius and one axis as shown in the figure below.

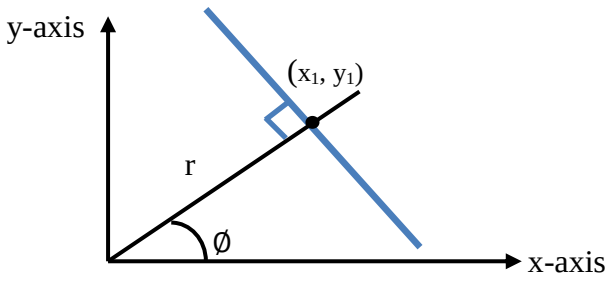

Figure (2-4) The coordinates of the image plane, the blue line is the detected line by (r, Ø**).**

The simple idea of Hough transform depends on accumulation of votes that tells us about the presence of a straight line in the edge detection image plane.This means detection with a high score of voting by finding local maximum in the accumulation matrix is enough to extract the line in the image.

The main advantage of this approach in image analysis is identification of some features within the image such as lines or circle. The motivation for using this technique in the thesis is its ability of detection and separation of muscle fascicles in the ultrasound image. This is useful in the evaluation of the pennation angle in one snapshot. Recently, this technique has been used in the detection of pennation angle of the gastronomes muscle (Zhou et al, 2015).

2.7 Artificial Intelligence tools to improve parameters extraction

The ability to solve problems by computer using an intelligent manner and as close to human thinking is defined as artificial intelligence. Machine learning is a field, which lies within the border area of artificial intelligence; machine learning is concerned with training data sets to learn using either of two approaches supervised or unsupervised. The main distinction

between supervised and unsupervised learning is the way of learning. In a supervised learning, the context of the training input is labelled with corresponding target output: but this target output does not necessarily have to come from a guiding human, it may also be under machine guidance. Unsupervised training in contrast does not rely on feedback by comparing outputs with target outputs. It instead searches for regularities in the entire dataset of inputs. Although unsupervised learning is more complex than supervised, it helps to figure out problems, which is normally difficult for humans to address. An example of unsupervised learning is clustering different data sets into groups of closely related features such as clustering a set of the pixels that have similar features into a group. While the example of supervised learning is data classification such as classification of the image pixels whether it is edge or non-edge pixel.

Artificial intelligence has a plethora of applications in different fields of life: industrial, medical diagnosis, medical image processing, military applications, safety applications, the internet and development of other computer systems. However, application of artificial intelligence in medical image processing is the main concern in this thesis.

2.7.1 Artificial Intelligence in image processing

Different approaches using artificial intelligence have been used in medical image processing; due to the ability of artificial intelligence tools in problem analysis and the efficacy of the processing compared with traditional image processing tools. Some of these approaches are genetic algorithms, data mining techniques, support vector machine, fuzzy image processing techniques, artificial neural networks and deep learning techniques such as convolutional neural network.

Patterns of the musculoskeletal ultrasound images show ambiguity in the interpretation of the details of the image due to the overlap between grey level intensities. Fuzzy logic techniques have the potential to address complex musculoskeletal ultrasound image patterns that are often characterized by vagueness and uncertainty. Furthermore, characteristics of the CNN allow to extract local features from musculoskeletal ultrasound image; therefore, there is the possibility of training artificial neural networks such as training convolutional neural network on these patterns for detection of various musculoskeletal components. Recent examples of using an artificial neural network in medical image classification (Plis et al., 2014) and edge detection of ultrasound images (Jabbar et al., 2016) shows its potential. In this thesis, convolutional neural networks and fuzzy image processing techniques were selected in processing musculoskeletal ultrasound images.

2.7.1.1 Convolutional Neural Network (CNN)

The artificial neural network has been introduced in two revolutions in the machine learning. The first revolution occurred in 1986, when Backpropagation Neural Network (BNN) was introduced (Rumelhart et al., 1986). BNN is a learning method, which is usually concerned with updating weights across three layers: input layer, output layer and hidden layers. The supervised training algorithm tries to get minimum error between output and target. BNN has many applications in image processing such as pattern recognition (Mozer, 1989; Kosbatwar, 2012). However, increasing the number of layers in the network has a limitation in speed and effects the quality of the learning algorithm. The recent revolution involves Deep Learning Neural Network (DLNN), which emerged in 2006. DLNN addresses several problems with BNNs that have many layers (Hinton et al., 2006). Therefore, deep learning is a new trend in machine learning. The basic concept of deep architecture is derived from understanding brain function, how the brain interprets data and how it deals with processing

across multiple stages. The main purpose of DLNN is the construction of high-level features from low-level information to boost machine interpretation tasked in understanding image for recognition, segmentation and classification purposes (Bengio, 2009). For example, in the case of object recognition, the first layer can deal with selected samples of image edges. The second layer may focus on the construction of the object boundaries until recognition of the final shape of the object.

DLNN uses several algorithms, which have been introduced in image processing; the deep architecture of these neural networks is different according to change in the building block. Deep Belief Net (DBN) is one of the DLNN techniques. The building block of this network is Restricted Boltzmann Machine (RBM), (Hinton et al., 2006; Hinton, 2007; Fisher and Igel, 2012), see figure (2-5).

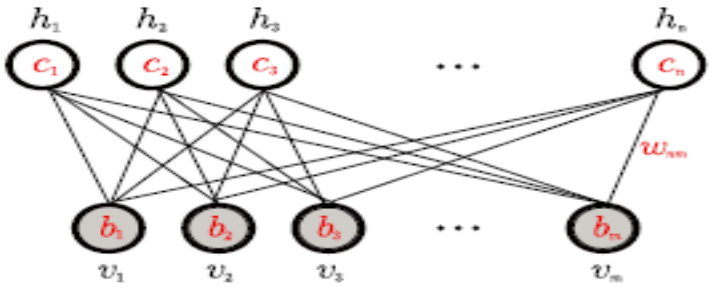

Figure (2-5) RBM structure, which is adapted from Fischer (2012).

RBM has two undirected layers, the first layer consists of a set of hidden units which are not connected to each other, while the second one has a set of visible units. Each layer of RBM is pre-trained with an unsupervised learning algorithm. Simply, DBN is constructed by stacking RBMs. The hidden neurons in the first RBM can represent low-level features from an input image. In the next step, the output of the first hidden neurons will be input into

another RBM; this procedure is repeated until getting high level features. Stacked Denoising Auto-Encoder (SDAE) is the second member of the DLNN family. The main components of SDAE is a three-layer auto-encoder network with a smaller middle layer (Pascal et al., 2010). These three layers of the network effectively consist of two stages: the first stage is concerned with encoding input data and the second stage performs decoding to reconstruct the output as similarly as possible to the input data. The training algorithm is implemented locally to extract relatively uncorrupted features. Denoising auto encoders are stacked and trained until obtaining acceptable image features. (CNN) is another member of DLNN family. The simple concept of CNN is inherited from the biological process at the visual cortex. CNN consists of several different layers including several convolutional layers, subsampling layers and a final fully connected classification layer (Cernazanu-glavan, & Holban, 2013). CNN effectively deals with transforming input image data to a group of feature maps across a convolutional layer by using a set of filter banks. Subsampling layer fosters CNN learning because it contributes to the reduction of input image data and at the same time maintains important data (invariant translation). This layer is quite useful in the convergence that means it contributes to reducing the time of the training (LeCun et al., 1998). The fully connected classification layer comes after many layers of the convolutional and subsampling layers, see figure (2-6).

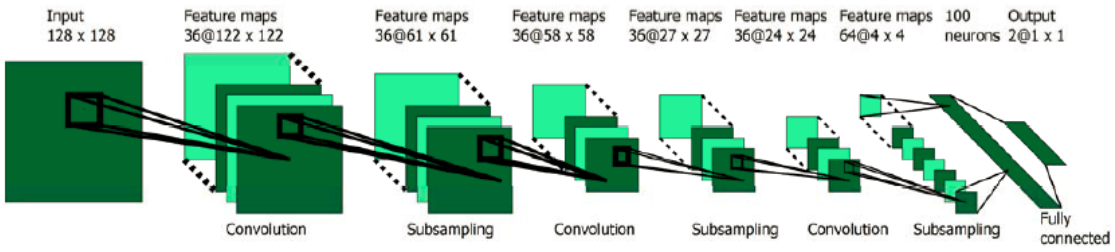

Figure (2-6) Simple diagram of CNN, this figure is updated from Cernazanu-glavan, & Holban (2013).

CNN has been applied successfully in image processing and has flourished in medical applications. For example, segmentation of the biopsy image (Silvoster, 2012), and an x-ray image of the chest (Cernazanu-glavan, & Holban, 2013) and bone (Yang et al., 2016). These applications have illustrated a high performance of CNN in edge detection. This thesis has application in musculoskeletal ultrasound images (Jabbar et al., 2016), see Chapter5-part1. CNN was recruited to perform image edge detection for panoramic ultrasound images of the shoulder region. CNNs are trained using two different ground truth interpretations. The first one uses an automatic Canny edge detector to provide the ground truth image and the second ground truth was obtained using the same image marked-up by an expert anatomist. In this initial study, the CNNs have been trained using half of the prepared data from one image, using the other half for testing. Validation was also carried out using three unseen ultrasound images. The results show that CNN performance when using an expert ground truth image is better than using the Canny ground truth image. Moreover, the results are promising in the image edge detection applications of musculoskeletal ultrasound images and this is an initial step, which helps to measure geometric properties based on using CNN.

2.7.1.2 Fuzzy Image Processing techniques

Fuzzy image processing techniques are one member of the artificial intelligence family. Lofti Zadeh introduced fuzzy logic in 1965. Fuzzy techniques permit a many-valued logic that ranges between [0, 1] rather than being solely restricted to just precisely 0 or 1, as is the case with Boolean logic. It has been used as a tool in image processing since the 1980's (Rosenfeld & Haber, 1985). Fuzzy image processing concentrates on using different approaches in the image processing such as fuzzy inference techniques, fuzzy logic, modification of fuzzy membership function, using fuzzy filters, using the measure of

fuzziness and fuzzy entropy (Ibrahim, 2004). Fuzzy image processing techniques are based mainly on three main stages, which are illustrated in the figure (2-7).

Figure (2-7) Pipeline of fuzzy image processing.

Fuzzification means mapping grey level intensities of the input image, which ranges between the minimum and maximum grey level intensities (spatial domain) to the values between 0 and 1 (fuzzy domain). This mapping depends on the selection of an appropriate membership function. In terms of the processing stage, different approaches describe this stage and are frequently used in the image processing. Some of this processing is based on fuzzy construction rules. These rules can be defined by expert domain to describe how the problem can be solved using fuzzy linguistic variables. The fuzzy technique which includes this kind of processing is known as fuzzy inference technique. Fuzzy rules are statements of linguistic variables and consist of two parts: antecedent and consequent. Antecedent represents the first part of the rule (if-condition or reason), while consequent illustrates the second part (conclusion). Fuzzy image filters are an example of this approach and they are commonly utilized in image processing techniques (Farbiz et al., 2000). The second approach is the modification of membership function after fuzzification; it is based to make some adjustment in the membership function to solve the problem. For example, fuzzy contrast image intensification (Tizhoosh et al., 1997) and Intuitionistic Fuzzy Sets (IFS) (Deng et al., 2016). Defuzzification is the last stage of fuzzy image processing pipeline, it transforms the results

from the fuzzy domain back to the spatial domain after solving a problem and shows us the power of the fuzzy system on the image.

Defuzzification has different strategies depending on the kind of processing stage. These strategies are mean of maximum method, centre of gravity method, using inverse membership function (Nachtegael et al, 2010), Takagi and Sugeno method (Takagi and Sugeno, 1985) and Mamdani method (Mamdani, 1974). In the case of fuzzy inference technique, Mamdani or Takagi and Sugeno methods are two common methods of defuzzification process. The main difference between Mamdani and the Takagi and Sugeno methods is the second part of the rule (consequence). In the Mamdani method, fuzzy set values are between 0 and 1, while in the Takagi and Sugeno method there is the crisp value (numerical value). In both methods, defuzzification used aggregation of the output of consequent (unification of the outputs of all rules) to get the final output (Runkler, 1997). In the case of the processing stage is the modification of the membership function, defuzzification can be determined using the inverse transformation G^{-1} (Tizhoosh et al., 1997), see equation (4) and equation (5).

$$Fuzzification = \mu\big(I(i,j)\big) \tag{4}$$

$$Defuzzification = G^{-1}\,\mu(I(i,j)) \tag{5}$$

Where $\mu\big(I(i,j)\big)$ represent membership function of input image and $G^{-1}\,\mu(I(i,j))$ illustrates output image after defuzzification. There are several examples of fuzzy techniques in medical image processing such as using fuzzy filters in image enhancement and segmentation (Nachtegael et al., 2010). The implementation of the fuzzy filters relies on fuzzy logic and fuzzy rules. Another example is follicle identification of the ovaries on the ultrasound image using the fuzzy inference technique (Hiremath and Tegnoor, 2014).

Modification of membership functions is another application based on Intuitionistic Fuzzy Sets (IFS), which is employed in medical images such as mammograms (Deng et al., 2016) and MRI images (Deng et al., 2016). Another example is the implementation of contrast intensification method, which is based on the modification of the fuzzy membership function; it was performed on breast ultrasound images (Guo et al., 2016) and x-ray image (Krell, 1997). Based on different assessment metrics, these techniques give successful results in image enhancement; however, there are few examples of using fuzzy technique of musculoskeletal ultrasound imaging applications.

2.8 Summary

This chapter outlines the main objective of musculoskeletal modelling: movement analysis of human and skeletal loading and highlights the challenges that arise due to the difficulty of the evaluation of internal forces of the musculoskeletal system in vivo. Musculoskeletal models endow an opportunity to study the movement of the upper limb in vivo. Examples of shoulder and upper limb models have been reviewed in (Bolsterlee et al., 2013). This work shows the development of musculoskeletal modelling of the shoulder across many types of research. In addition, it reveals that the building of personalised musculoskeletal models is not trivial because it is hard to estimate musculoskeletal parameters in vivo. One of these models is the Delft Shoulder and Elbow Model, which was involved in several applications such as tendon transfers (Magermans et al.,2004) and wheelchair propulsion (Veeger. et al.,2002).

The solid foundation of musculoskeletal model design is inherited from musculoskeletal parameters. Some of these parameters are tendon and muscle fibre length, pennation angle, and muscle volume. A review of the literature illustrates a wide variety of methods, which

were proposed to calculate these parameters manually. The first method depends on cadaver data (Veeger et al., 1997; Arnold et al., 2009). Medical imaging can be used to extract these parameters from healthy participants. For example, using MRI (Arnold et al., 2000; Heemskerk et al., 2009; Bignotte et al., 2014) and US (Graf, 1980; Gompels & Darlington, 1981; Herbert & Gandevia, 1995; Maganaris et al., 1998; Martin et al., 2001; Infantolino et al., 2007; Scott et al., 2012; Han et al., 2013; Slane & Thelen, 2014). Interestingly, the third method is using medical imaging tools for scanning cadaver data as another way of extracting these parameters (Scott et al., 1993; Narici, 1999; Martin et al., 2001). However, the extraction of the musculoskeletal parameters from a cadaver has several restrictions such as preservation media, accurate dissection and in vitro (Scott 1993; Martin et al., 2001; LaScalza & Gallo, 2002). Furthermore, it is time-consuming when using medical imaging tools; they have limited ability to identify parameters automatically. Consequently, this data allows making a generic statement about the function of the musculoskeletal system, but this is not enough to get accurate data and timely for each patient. The work proposed aims to develop methods for the extraction of some of the musculoskeletal parameters of ultrasound imaging automatically. Digital image processing, convolutional neural network and fuzzy image processing techniques were used as tools to achieve this purpose.

Chapter Three

Collection of reference ultrasound image data from cadaver specimens and healthy volunteers

Chapter 3 Collection of reference ultrasound image data from cadaver specimens and healthy volunteers

3.1 Introduction

The primary concern of collecting a set of the reference musculoskeletal ultrasound images is to compare traditional and novel image processing methods based on these images. This chapter includes protocols of collection of these image data from ultrasound machine. In this thesis, two sources of data are introduced, the first source is a cadaver, ultrasound machine was involved in the visualising of the shoulder region of the cadaver after dissection, this data was published (Heinz, 2016). The second source comes from healthy volunteers; ultrasound image data was collected from 25 healthy volunteers.

3.2 Ethical approval

All details of the institutional ethics approval (Ref No: ERP1290) from Keele university is shown in the APPENDIX I.

3.3 Data collection

Musculoskeletal ultrasound images were collected from cadaver and healthy volunteers.

3.3.1 Reference ultrasound image from cadaver specimens

Reference ultrasound images of the cadaver in this thesis were collected from the left and right shoulder region of the fresh-frozen cadaver (74 years old man) using advanced ultrasound machine (LOGIQ e Bt12). Ultrasound scanning of a cadaver can be helpful to define the internal structure of the musculoskeletal system after dissection. It is possible to dissect the specimen and take measurements to obtain the ground truth image. Figure (3-1)

presents one sample of these data, which was collected from left shoulder region. Initial dimensions of this image were 550 x 1024 pixels, but after cropping to select the region of interest, image dimensions became 178 x 783 pixels. Furthermore, it is panoramic ultrasound images that illustrates different muscles such as Infraspinatus muscle, Trapezius muscle and Deltoid muscle (Heinz, 2016). Panoramic ultrasound image can be beneficial to visualize a set of views in one ultrasound image.

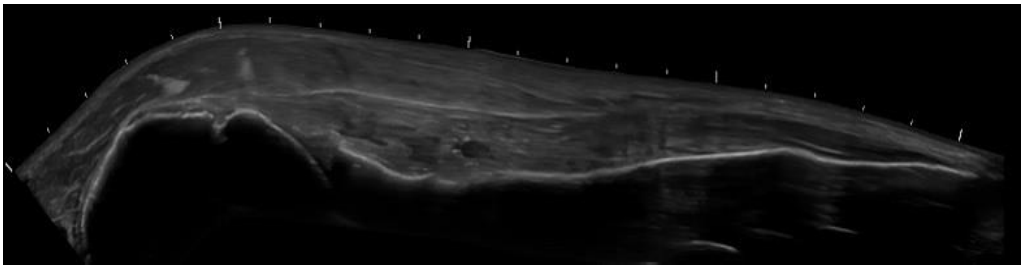

Figure (3-1) Panoramic ultrasound image of the left shoulder, which was collected from a cadaver.

3.3.2 Reference ultrasound image from healthy volunteers

In this work, musculoskeletal ultrasound images were acquired from 25 human volunteers (9 females and 16 males); age (39±15) years old. Those volunteers with no history of upper limb injuries were eligible for data collection. Non-invasive ultrasound scanning techniques (LOGIQ S7) with the linear probe were used. Collection of data was based on the ethics approval (Ref No: ERP1290), all details in APPENDIX I.

The quality of the ultrasound image varies from one ultrasound device to another, according to the age of the machine and loaded software on it. For example, it is possible to get ultrasound image, which has a good quality and this image presents multiple views in one image (panoramic image) using a modern ultrasound machine. Furthermore, ultrasound machine has different parameters, which control the clarity of ultrasound image. Some of

these parameters are frequency, gain, depth and dynamic range. Adjustment of these parameters is not complicated, but expertise of the using ultrasound machine is required to illustrate a clear view of an ultrasound image.

In this thesis, ultrasound image data were collected from different segments of upper limb (arm, forearm, wrist and hand) at transverse and longitudinal sections. For example, scanning the cross-section of the Flexor Policies Longus Tendon (FPLT), this section was pointed at the midpoint between carpometacarpal joint and metacarpophalangeal joint. The ultrasound images of FPLT were collected at different values of each parameter to assess the difference then get the most precise appearance, which has a high level of the ultrasound image details.

The first parameter is frequency, selection of a suitable frequency depends on a needed depth of the penetration. High frequency is convenient for scanning small and superficial muscles (Lew et al., 2007). The possible range of frequency setting at linear probe of LOGIC S7 is (8, 12, 15) MHz. However, there is no observable change in image details and appearance at this frequency range. Hence, the median value (12 MHz) was chosen.

The range of depth parameter of the LOGIC S7 is between (1.5-7) cm. Different depth demonstrates different levels of the musculoskeletal structure information and resolution. See the example in the figure (3-2)*a*, which shows ultrasound image at depth 1.5 cm, while in the image of the figure (3-2)*b*, depth =7cm. Ultrasound image of figure (3-2)*a* illustrates a few details of cross section of the tendon and around compared with the image of the figure (3-2)*b*, which shows cross section of tendon and underneath. However, ultrasound image of figure (3-2)*a* has higher resolution than ultrasound image in figure (3-2)*b*. Image depth equals 4.5cm was selected to give acceptable view in illustrating the details of the musculoskeletal structure.

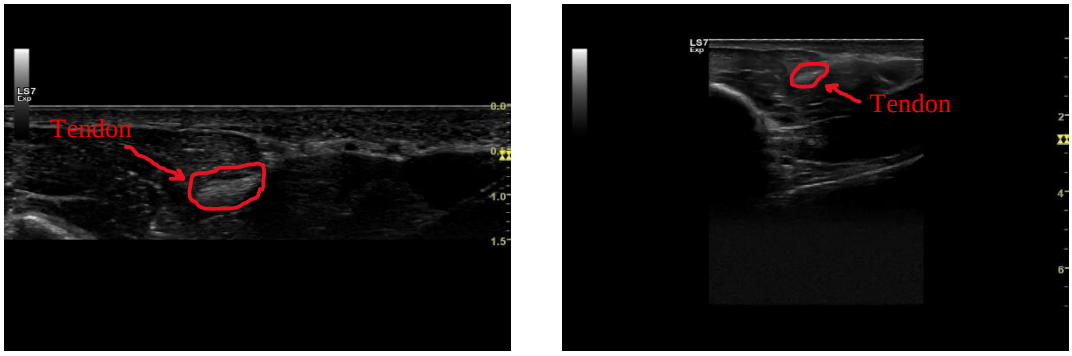

a ***b***

Figure (3-2), this figure from left to right shows image visualization at depth 1.5cm and 7 cm respectively. Figure (*b*) shows a high level of the musculoskeletal structure information and less resolution, while figure (*a*) illustrates less musculoskeletal structure information and high resolution.

The amount of black, white and grey could be altered on the screen by adjusting the gain parameter. (Ihnatsenka & Boezaart, 2010). The range of the gain in the LOGIC S7 is between (35-90). Figure (3-3)*a* shows the image with a low gain, while the image in figure (3-3)*b* illustrates the image with a high brightness. The problem of this option (gain) is that the increase of the brightness in all image regions even in the region, which has an acceptable brightness, this leads to difficulty in interpretation of the image contents correctly. The value of the gain equals 54 was selected after adjustment to get acceptable value.

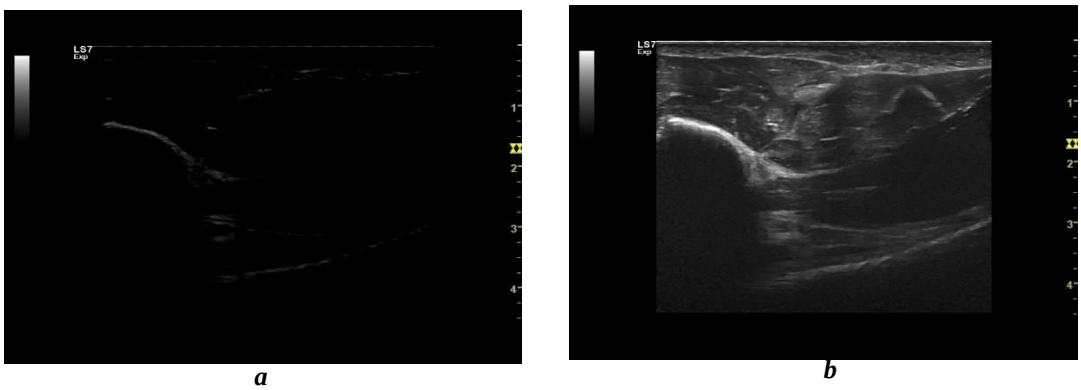

a ***b***

Figure (3-3), this figure from left to right shows collected images at low and high gain respectively.

In the term of changing dynamic range of the LOGIC S7, the range is between (36-96). When dynamic range in the ultrasound machine is low (36), this results in an image with high contrast. Figure (3-4)*a* illustrates a high contrast image in all image regions and histogram presents high difference between grey level intensities values. On the other hand, it is hard to recognise image components of the figure (3-4)*b* when dynamic range =96, histogram shows low difference between grey level intensities values. Dynamic range equal to 66 was selected after adjustment to get acceptable value.

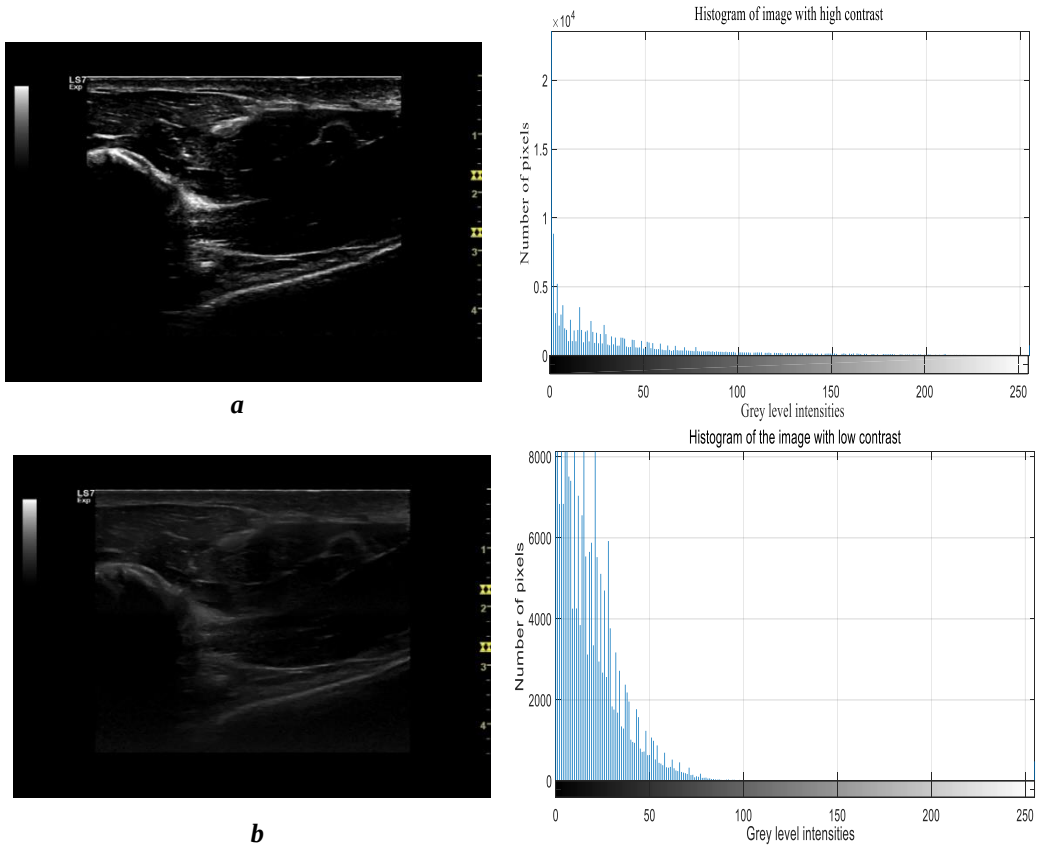

a

b

Figure (3-4), the first line of this figure presents ultrasound image at high contrast (dynamic range=36) and its histogram, while the second line illustrates ultrasound image at low contrast (dynamic range=96) and its histogram.

In this thesis, parameters were changed and applied on the collected data (musculoskeletal ultrasound images) in the different upper limb regions. The acceptable view of the

musculoskeletal ultrasound images, which were collected using LOGIC S7 were at frequency=12 MHz, gain=54, depth=4.5 cm and dynamic range=66. Figure (3-5) shows ultrasound image of FPLT at these parameters. Histogram of this image presents a sensible difference between grey level intensities values.

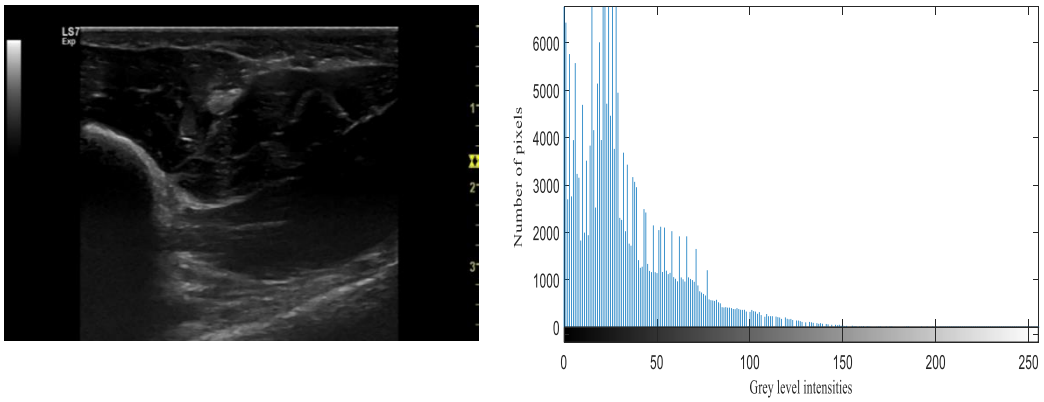

Figure (3-5), illustrated collected image and its histogram when frequency=12 MHz, gain=54, depth=4.5 cm and dynamic range=66.

3.3.2.1 Data collection protocols

The primary goal of the data collection protocols is to yield accurate information based on standardised methods. Six protocols were introduced to collect ultrasound image from upper limb of 25 healthy volunteers; two protocols for the arm, and the same for forearm and hand regions.

The following protocols were used to collect data from different regions in the upper extremity (arm, forearm and hand):

1-**Arm: -** two protocols were presented:

The first protocol was the single snapshot of the ultrasound static scanning to identify the tendon of the triceps brachii muscle (triceps brachii is one of the superficial arm muscles) in a longitudinal plane. The registration point of the probe is the olecranon process of the ulnar and the position of the volunteer participant is opposite to the researcher who works on ultrasound machine; elbow joint of the volunteer flexed 90º with the palm resitting on the table (crab position), see figure (3-6)*a*.

The second protocol was also the single snapshot of the ultrasound static scanning. The position of the participant is the same as in the previous protocol, but the probe is far 4.5cm from registration point (olecranon process of ulnar), also in a longitudinal plane (see figure (3-6)*b*). The primary purpose of this protocol is to measure the thickness and pennation angle of triceps muscle (single ultrasound image).

a

b

Figure (3-6), the left hand of the figure illustrates scanning posterior aspect of the elbow joint at crab position, while the right-hand shows scanning one snapshot ultrasound image of the medial head of the triceps muscle at crab position.

2-Forearm: - two protocols were introduced:

The first protocol was ultrasound static scanning to identify the tendon of flexor carpi radialis muscle (flexor carpi radialis is one of superficial forearm muscles). It is one snapshot at a longitudinal plane and probe position was on the insertion of this muscle (midpoint between the second and the third metacarpal bone), see figure (3-7).

Figure (3-7) Longitudinal section scanning of flexor carpi radials tendon.

The second protocol was dynamic ultrasound scanning for tracking flexor carpi radialis muscle from insertion to origin (video recording).

3-Hand: - two protocols were presented:

The first protocol was static ultrasound scanning of flexor pollicis longus tendon (muscle of forearm and hand), the probe position at the midpoint between carpometacarpal joint and metacarpophalangeal joint. It is a single snapshot, but ultrasound scanning occurs at two planes. The first scanning at a longitudinal plane to view flexor pollicis longus tendon longitudinally, while the second scanning occurs at transverse plane to measure area and circumference at the cross-section of this tendon, see figure (3-8).

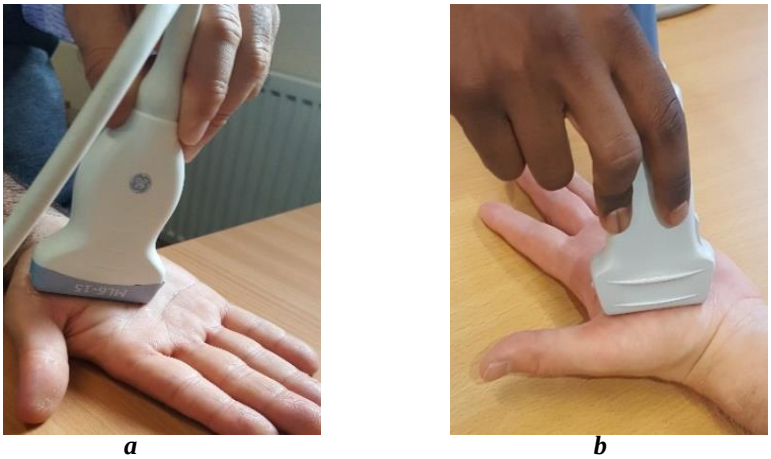

a ***b***

Figure (3-8), the left hand of the figure illustrates scanning one snapshot of flexor pollicis longus tendon (transverse plane), while the right-hand shows scanning of this tendon at longitudinal plane.

The second protocol was dynamic ultrasound scanning of flexor pollicis longus tendon by moving the probe from the midpoint between carpometacarpal joint and metacarpophalangeal joint to the base of distal phalangeal joint (video recording).

3.4 Summary:

The primary purpose of collecting data in this thesis is to capture a material (musculoskeletal ultrasound images), which allows applying developed methods and answer thesis research questions. Ultrasound images were obtained from two sources and used for different purposes.

The first source of the musculoskeletal ultrasound image is from a cadaver (scanning of the longitudinal section of the left and right shoulder region). It is panoramic images, which illustrated a variety of the muscles in one image. Panoramic ultrasound images were involved in testing and showing the performance of several developed methods such as ultrasound image enhancement methods in part1 (speckle noise reduction) and part2 (contrast image enhancement) of chapter 4. Moreover, it was used in part 1 of chapter 5 to

illustrate the performance of using convolutional neural network in pixel classification of musculoskeletal ultrasound image whether it is edge pixel or not.

The second source of the musculoskeletal ultrasound imaging comes from healthy volunteers, static and dynamic ultrasound scanning at longitudinal and transverse sections of different parts of the upper limb: arm, forearm and hand. Six protocols were introduced and applied to upper limb segments for different purposes. Developed contrast image enhancement methods in part 2 of chapter 4 were employed on the video ultrasound of the hand region, see protocol 2 and ultrasound images of triceps tendon, see protocol 1 of arm region. Also, musculoskeletal ultrasound images collected using protocol 2 of arm region were utilised to evaluate thickness and pennation angle of triceps muscle, see Chapter 6. Ultrasound images, which were captured from hand region, protocol 1 was used in measuring the area and circumference of the cross-section of flexor pollicis longus tendon in the same chapter. Furthermore, the same images were involved in demonstrating the performance of fuzzy edge detection method in part 2 of chapter 5.

Chapter Four

Ultrasound Image Enhancement

Chapter 4 Ultrasound image Enhancement

4 Introduction

One of the primary objectives of this dissertation was to enhance the quality of the musculoskeletal ultrasound images. In order to address this objective adequately, the major limitations of an ultrasound image are stated, and the successful solutions are proposed through this dissertation. To start with, an ultrasound image by its nature has two main limitations: the presence of the speckle noise and low image contrast.

This thesis introduces two techniques as pre-processing steps to address these limitations. Firstly, a speckle noise reduction tool that would improve the evaluation of the cross-section area of the muscle tendon and the calculation of muscle thickness as it requires a homogenous region free from speckle noise. Secondly, a novel local contrast enhancement method was developed and employed to improve the determination of the musculoskeletal parameters such as pennation angle. Evaluation of the pennation angle needs to illustrate some details between muscle borders such as orientation of muscle fibre. Local contrast image enhancement technique helps to increase luminance difference between pixels and illustrate more details. Ultimately, it is necessary to consider the selection of image enhancement techniques, which are useful to support automated extraction of musculoskeletal parameters.

This chapter consists of two parts; speckle noise reduction in the musculoskeletal ultrasound images methodology and implementation, the outcomes of which are all addressed in the first part. Whereas, a novel contrast enhancement method of the musculoskeletal ultrasound image is discussed in the second part.

4.1 Part 1: Speckle noise reduction in the ultrasound image

4.1.1 Introduction

Speckle noise during the recording of a musculoskeletal ultrasound image is the major confounder that was reported in the previous studies (Michailovich & Tannenbaum, 2006; Bama & Selvathi, 2014). It degrades the fine details of the ultrasound image and. affects on the image quality in a significant manner. The existence of speckle noise in an ultrasound images is mostly connected to the complex interactions of the coherent ultrasound signal, which can be captured as a part of the image acquisition process of an ultrasound machine.

All in all, the detection and elimination of speckle noise in ultrasound images is still a great challenge to the researchers because it is multiplicative noise and difficult to eradicate completely.

In part one of this chapter, speckle noise of the musculoskeletal ultrasound image was reduced by applying a non-linear filter such as local median adaptive filter and anisotropic diffusion filter. Imaging filters to reduce speckle noise were applied for the first time on musculoskeletal ultrasound images of the upper limb. The main purpose of using these filters is to get a more homogenous area, which aids segmentation for the evaluation of the cross-sectional area of the muscle and tendons.

4.1.2 Presence of noise in medical images

There are different kinds of noise in the medical images such as impulse noise, Gaussian noise and speckle noise (Sanches et al., 2008). Impulse and Gaussian noises are additive noise, while speckle noise is multiplicative noise.

The main distinction between additive and multiplicative noise is that additive noise does not vary with the intensity of the signal of interest, whereas multiplicative does increase in the case of increasing the intensity of the signal of interest.

Speckle noise is the dominant noise in ultrasound images and Synthetic Aperture Radar (SAR) images. Speckle noise results from coherent acquisition imaging systems due to coherent reflection from different sources around the target. Impulse and Gaussian noises arise while acquiring a medical image from a medical device, transmission and storage. Based on the shape of the distribution of noise in the image, we can differentiate impulse and Gaussian noises. When corrupting collected image, impulse noise could add high or low values to the image (Gravel et al., 2004) whereas, the shape of the Gaussian noise similar to the form of the normal distribution (Deepa and Sumithra, 2015). A simple representation of additive noise is illustrated in equation (6), while equation (7) demonstrates the modulation of multiplicative noise.

$$I_{xy} = B_{xy} + N_{xy} \quad (6)$$

$$I_{xy} = B_{xy}\, N_{xy} \quad (7)$$

Where I_{xy} is corrupted image, B_{xy} is enhanced image and N_{xy} is a noise (Gallegos-Funes et al., 2011). It is possible to recognise the difference between the nature of impulse noise (such as salt and pepper noise), speckle noise and Gaussian noise visually by adding these noises to the original image using Matlab toolbox, see figure (4-1).

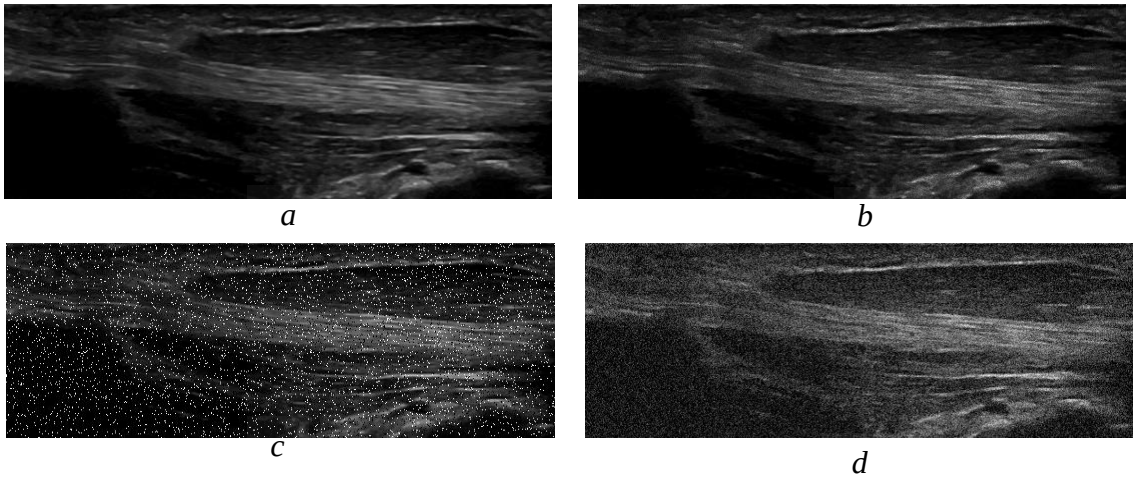

Figure (4-1) Input ultrasound image (longitudinal section of flexor pollicis longus tendon) is shown in figure (*a*) and figure (*b*) illustrates the same image after adding speckle noise. Figure (*c*) and (*d*) show input image after adding (salt and pepper) noise and gaussian noise respectively.

Speckle noise is an unavoidable component of the ultrasound imaging technique. However, it is possible to transform image pixels corrupted by speckle noise to allow them to be dealt with using linear techniques and therefore be treated as additive noise, by using nonlinear logarithmic transformation (Biradar et al., 2014).

4.1.3 Filtering to reduce speckle noise

Sources of additive noise can usually be dealt with using linear filtering techniques, whereas multiplicative noise has complex structure compared with additive noise because grey level intensities of the noise interfere with grey level intensities of the original image (Binaee & Hasanzadeh, 2014). Using speckle noise reduction filters emerged firstly and applied to Synthetic Aperture Radar (SAR) images, then these filters are employed to reduce speckle noise in the ultrasound images (Insana et al., 1989). One of the common filters is Anisotropic Diffusion Filter (ADF). ADF is an adaptive technique, which was employed successfully in SAR image filtering (Perona & Malik,1990; Aja-Fernandez & Alberola-Lopez, 2006), then was applied to the ultrasound images (Krissian, K. et al., 2007).

Other spatial filters in image processing were introduced for despeckling purposes. For example, the adaptive filter (Lee, 1980; Frost et al., 1982; Kuan et al., 1987) and Local Adaptive Median Filter (LAMF) (Qiu et al., 2004) were introduced. LAMF attains a good outcome in improving image appearance because LAMF can not only diminish speckle noise, but also maintain image details such as image edges. It applied by the evaluation of the statistical properties of the image locally to detect speckle noise pixels. This is achieved by evaluation of local mean and standard deviation of sliding window image across original image. However, this method was performed on Synthetic Aperture Radar (SAR) image, not on the musculoskeletal ultrasound image. Despite SAR images and musculoskeletal ultrasound sharing the same noise, there is a difference in the texture information between the two images.

4.1.4 No-reference assessment metrics of speckle noise reduction

There are four metrics that were used in the performance assessment of speckle noise reduction in the resultant image. The reason for using these metrics is the difficulty of obtaining a reference image of musculoskeletal ultrasound that is entirely free from speckle noise. These metrics are employed without needing to the ground truth image; therefore, these metrics are the best choice for performance assessment after reducing speckle noise. The first metric is Speckle Suppressions Index (SSI), which can be calculated using equation (8):

$$\mathrm{SSI} = \frac{\sqrt{(\mathrm{var(R)}}}{\mathrm{mean(R)}} . \frac{\mathrm{mean(I)}}{\sqrt{\mathrm{var(I)}}} \tag{8}$$

Where *R* is the resulting image after filtering, *I* is the input image with speckle noise, var represents the variance and mean the average of the grey level intensity of the image. The

variance of filtered image had to be less than input image due to speckle noise reduction; therefore, based on equation (8), small value of SSI indicates a high level of the speckle noise reduction in the image (Sheng and Xia, 1996). It is dependent on the ability to have a filter satisfying a mean-preservation property. Therefore, Shamsoddini addressed this problem by introducing a new metric, Speckle Suppression Mean Preservation Index (SMPI), which is evaluated using equation (9), (Shamsoddini and Trinder, 2010).

$$\mathrm{SMPI} = (1 + |\mathrm{mean(I)} - \mathrm{mean(R)}|).\frac{\sqrt{\mathrm{var(R)}}}{\sqrt{\mathrm{var(I)}}} \tag{9}$$

However, Dellepiane suggested another metric because SMPI has a limitation which relates to normalisation. It is the Mean Preservation Speckle Suppression Index (MPSSI) (Dellepiane and Angiati, 2014).

$$\mathrm{MPSSI} = \left|1 - \frac{\mathrm{mean(R)}}{\mathrm{mean(I)}}\right|.\frac{\sqrt{\mathrm{var(R)}}}{\sqrt{\mathrm{var(I)}}} \tag{10}$$

Low score of these three metrics (SSI, SMPI and MPSSI) indicates a high level of speckle noise reduction in the output image. The last metric in the assessment of speckle noise reduction package is Enhanced Edge Index (EEI) (Chunming et al., 2002). Equation (11) illustrates how can carry out this metric based on input and filtered image

$$EEI = \frac{\sum R(i,j) - R(i-1, i+1)}{\sum I(i,j) - I(i-1, i+1)} \tag{11}$$

The highest value of EEI is 1, and the best edge preservation occurs at a high score of this metric.

4.1.5 Local Adaptive Median Filter (LAMF)

Local Adaptive Median Filter (LAMF) was successfully applied to the SAR image by Qiu. (2004). LAMF detects speckle noise based on analysis of the statistical properties of the

candidate pixel at different window sizes (3x3, 5x5 and 7x7), then swap outlier pixel (speckle noise pixel) with the valid pixel. However, in this thesis LAMF was applied on the musculoskeletal ultrasound image with more expanded windows (3x3, 5x5, 7x7, 9x9 and 11x11) to examine the impact of enlarging dimensions of sliding window on the speckle pixels detection. Evaluation of statistical properties within small window includes local mean and standard deviation determination, see figure (4-2).

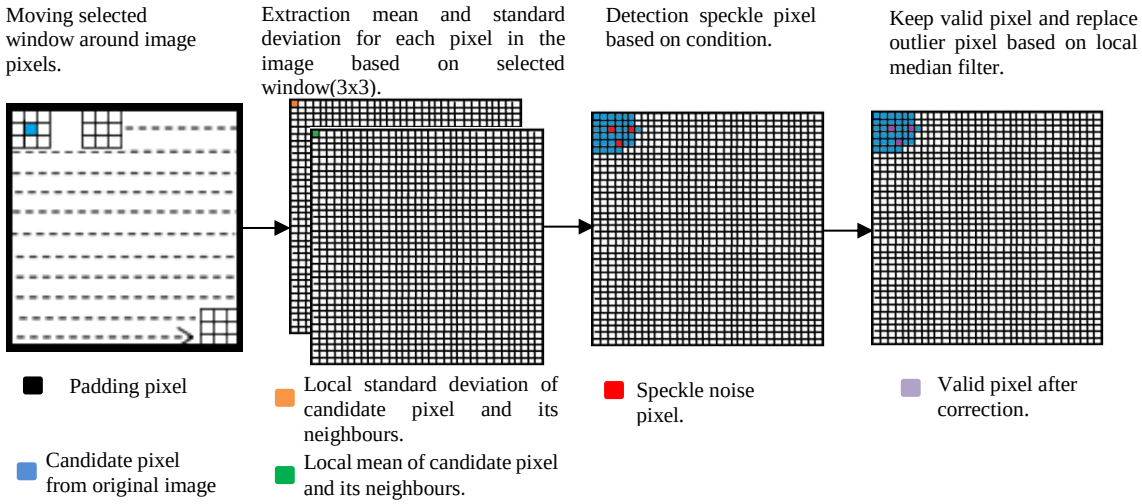

Figure (4-2) Processing steps of applying LAMF on 3x3 mask (central pixel and its neighbours around the image).

Implementation of LAMF consists of two main steps:

1- Detection of the speckle pixels of the input image

Each pixel in the input image was examined whether it is speckle or valid pixel. Detection of the pixels was performed by evaluating the statistics (local mean and standard deviation) of the sliding window across input image. Equation (12) and (13) give lower and upper border detection of each pixel inside the image.

$$LB(i,j) = \mu(i,j) - f * \sigma(i,j) \quad (12)$$

$$UB(i,j) = \mu(i,j) + f * \sigma(i,j) \quad (13)$$

where μ is local mean, σ =is local standard deviation of the selected window, dimensions of the central pixel are (i,j) and *f* is controlled factor.

Speckle and valid pixels are labelled by moving the window (central pixel is *c (i, j)*) and detected pixel is *d (i, j).* Equation (14) illustrates the condition of detection the central pixel whether it is a valid pixel or speckle pixel.

$$d(i,j) = 0 \qquad if \;\; c(i,j) < LB(i,j) \quad or \;\; c(i,j) > UB(i,j) \tag{14}$$

$$d(i,j) = 1 \qquad if \; LB(i,j) \leq c(i,j) \leq UB(i,j)$$

2- Replace speckle pixel with valid pixel

Applying local median filter on the selected window, which contains speckle pixel as the central pixel in the windows. This means, the replacement depends on the evaluation of the local median filter by swapping detected speckle pixel with median value of the window. The primary purpose of that is to reduce the impact of speckle noise on the image. However, reducing noise using a median filter is affected by two factors: the spatial content of the neighbourhood and the number of pixels which are utilised in the evaluations.

4.1.6 Anisotropic Diffusion Filter (ADF)

One of the standard methods that have been utilised in reducing speckle noise in the ultrasound imaging is anisotropic diffusion filter. There are some applications such as in kidney and heart ultrasound images (Abd-Elmoniem, et al., 2002), the liver ultrasound image (Krissian, K. et al., 2007) and ultrasound image of the shoulder (Gupta et al., 2014). The key aspect of diffusion has been acquired from standard heat diffusion; if the diffusion expands in all directions, in this case, diffusion is called isotropic diffusion. Since this kind of diffusion has lack of clarity in defining an edge and spread in all directions without concerning on the edge preservation. Anisotropic diffusion is concerned with edge

preservation because it concentrates on the direction to maintain edges. It happens by adding gradients of grey level intensity to the diffusion equation, as illustrated in equation (15).

$$\frac{d(X(i,j,t))}{dt} = div[g(|\nabla X(i,j.t)|).\nabla X(i,j,t)] \quad (15)$$

Where $\nabla X(i,j,t)$ is the image gradient, *t* is time parameter and $g(|\nabla X(i,j,t)|$ controls the edge direction, image gradients illustrate the directional change of the grey level intensities. This helps in the detection and preservation of the image edges. It means, it is likely to reduce speckle noise and preserve firm edges. Perona and Malik introduced two different functions of diffusion (Perona and Malik, 1990; Grieg et al.,1992); see equation (16) and equation (17).

$$F_1(p) = e^{\left(-\left(\frac{\|\nabla X\|}{k}\right)^2\right)} \quad (16)$$

$$F_2(p) = \frac{1}{1 + (\frac{\|\nabla X\|}{k})^2} \quad (17)$$

Where *k* is controlled factor on the gradient of edge sensitivity. The first equation shows high contrast edges over low contrast edges, while the second equation illustrates a wider homogenous region over the small one.

4.1.7 Implementation and Results

First, before performing LAMF, the most appropriate window size was selected based on a high score of assessment metrics of speckle noise reduction. Implementation of LAMF was achieved using equation (12) and (13) and control parameter *f* was 1.5 (used in the speckle noise reduction of SAR image (Qiu, 2004), also it was used in the MUI). If the value of *f* is greater than 1, it is possible to detect many speckle pixels but, in other cases can keep many valid pixels in the output image. In this work, three different samples of MUI are used as the

input image in the implementation of LAMF and ADF. The first sample was collected from the right shoulder of the cadaver, all details in section 3.3.1. While the second sample were obtained from healthy volunteers from arm-region (protocol 2)and the third sample from hand region (protocol 1), all details in section 3.3.2.1.

Cadaver image sample

LAMF was carried out on the cadaver ultrasound image sample, shown in figure (4-3), using different window sizes (3x3, 5x5, 7x7, 9x9 and 11x11).

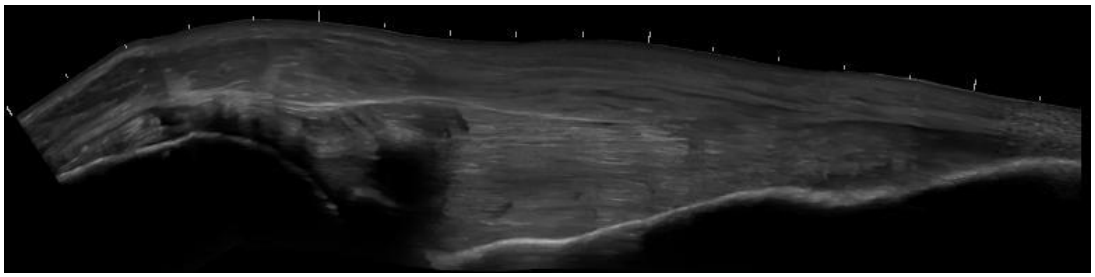

Figure (4-3) Musculoskeletal ultrasound image, which was collected from cadaver (right shoulder region).

The following table illustrates the evaluation of assessment metrics (SSI, SMPI, EEI and MPSSI) on the image in figure (4-3). This assessment was performed on different window sizes, see table (4-1).

Table (4-1) Evaluation of assessment metrics of cadaver musculoskeletal ultrasound image sample

Metrics	3x3	5x5	7x7	9x9	11x11
SSI	0.972	0.978	0.968	0.953	0.914
SMPI	1.052	1.105	1.147	1.188	1.564
EEI	0.918	0.881	0.881	0.890	0.727
MPSSI	0.0004	0.005	0.008	0.0106	0.027

It is clear from the table (4-1), window 3x3 gives lower scores of SMPI and MPSSI and a high score of EEI compared with other window sizes. Therefore, LAMF was carried out at

window size 3x3 and compared with the performance of ADF at this window and the process was repeated five times (five iterations). The purpose of iterations is to repeatedly apply the same process to the output at each pass. This is so systematically increase the effect of the filter, rather than to evaluate the output.

Figure (4-4), illustrates the comparison between two filters using four assessment metrics (ISS, SMPI, EEI and MPSSI). Whereas, figure (4-5) and figure (4-6) show the output image after applying ADF and LAMF on the image in figure (4-3) respectively. Figure (4-4) shows EEI metrics of LAMF with a higher score than EEI metrics of ADF. Furthermore, it is possible to observe in the figure (4-6), many of the edge pixels in the original image are retained in the filtered image compared with figure (4-5), which illustrates many homogenous regions in the filtered image and less preserving of the image edges.

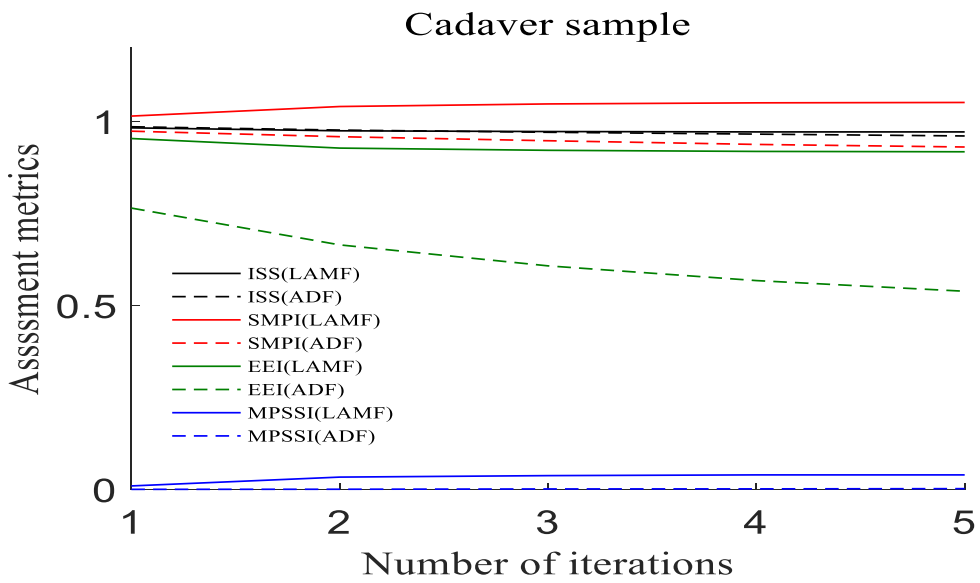

Figure (4-4) Comparison between performance of LAMF and ADF across five iterations when performing on cadaver musculoskeletal ultrasound image and window size is 3x3.

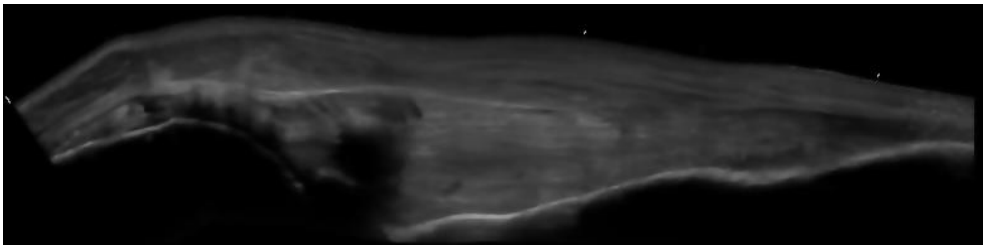

Figure (4-5) Cadaver musculoskeletal ultrasound image after applying ADF.

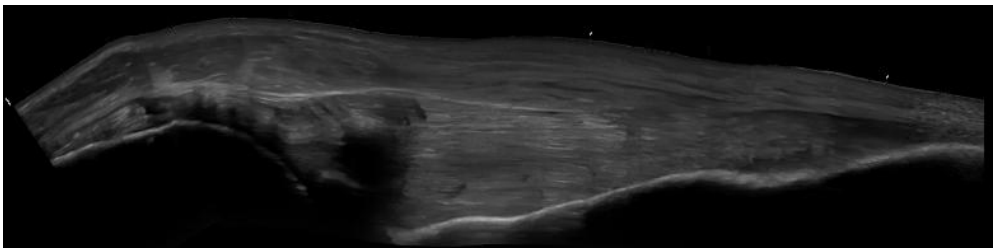

Figure (4-6) Cadaver musculoskeletal ultrasound image after applying LAMF.

This experiment helps to apply two different filters on the musculoskeletal cadaver image to reduce speckle noise and get an enhanced image, which is used in further applications. One of these applications is using enhanced musculoskeletal image in the measurement of the tendon length.

Healthy image samples

In the previous experiment, cadaver image sample is used to get evidence for illustration of the performance of ADF and LAMF filters. For more applications, healthy image samples were used, two different images as follows:

The first image was collected from triceps muscle (longitudinal section) as shown in the figure (4-7).

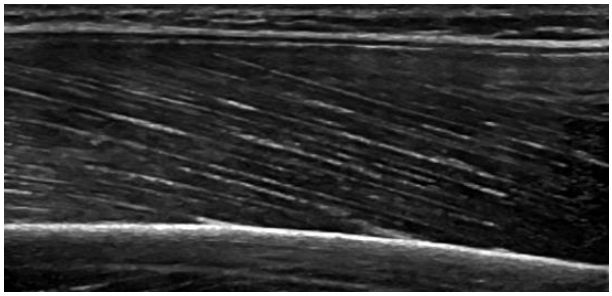

Figure (4-7) Healthy musculoskeletal ultrasound image (triceps ultrasound image).

Following the same steps of the cadaver sample to select window size, table (4-2) presents calculation of four metrics assessments of image in figure (4-7) after applying LAMF and at different window sizes (3x3, 5x5x, 7x7, 9x9 and 11x11). Also, from table (4-2) based on the assessment metrics, window 3x3 shows that it is the most suitable window, which is used in performing LAMF. Therefore, the performance of ADF compared with LAMF at this window is shown in the figure (4-8). Furthermore, figure (4-9)*a* and figure (4-9)*b* illustrate the output images after performing ADF and LAMF on the image in figure (4-7) respectively. Based on the figure (4-8) and through figure (4-9), the same conclusion of the previous experiment (using cadaver image sample) was obtained.

Table (4-2) Evaluation of assessment metrics of arm musculoskeletal ultrasound image sample.

Metrics	3x3	5x5	7x7	9x9	11x11
SSI	0.990	0.993	0.953	0.901	1.448
SMPI	1.05	1.228	1.722	2.108	11.35
EEI	0.989	0.967	0.955	0.956	0.604
MPSSI	0.0009	0.005	0.018	0.029	0.212

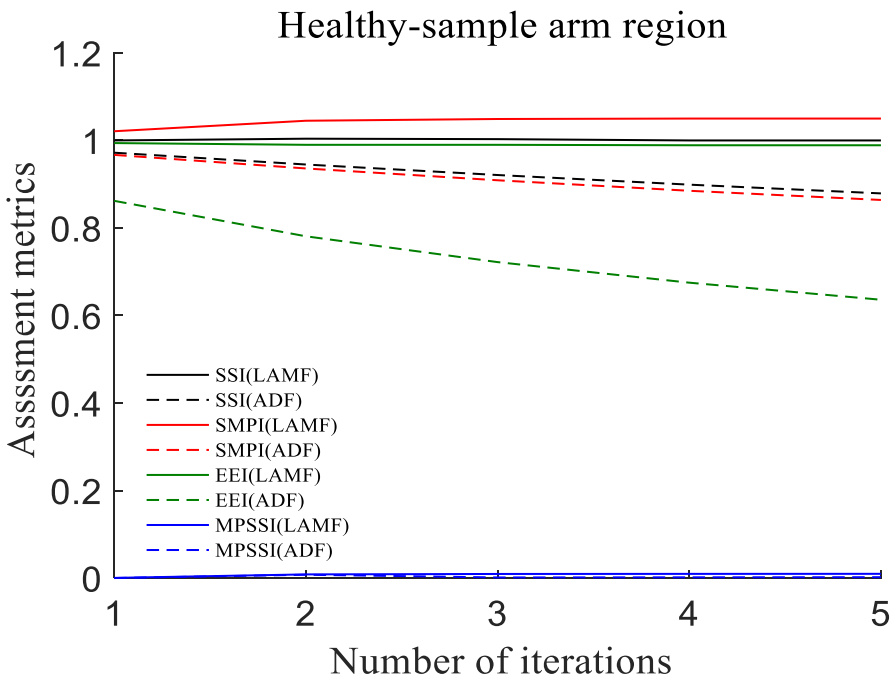

Figure (4-8) Comparison between performance of LAMF and ADF across (1-5) iterations when performing on the healthy sample of the musculoskeletal ultrasound image (triceps muscle) and the size of the window is 3x3.

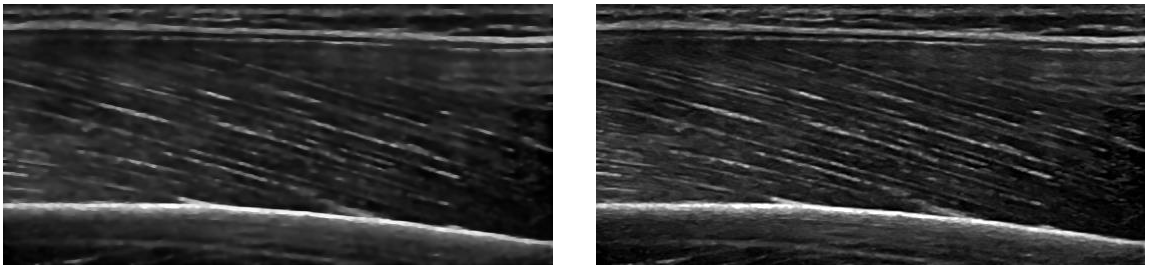

a ***b***

Figure (4-9) Healthy musculoskeletal ultrasound image (triceps ultrasound image after applying ADF is shown in figure (*a*), while figure (*b*) illustrates output image after applying LAMF.

Image was collected from hand region (transverse section of Flexor Pollicics longus tendon) as shown in the figure (4-10).

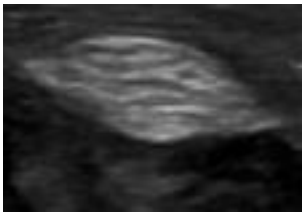

Figure (4-10) Healthy musculoskeletal ultrasound image (cross section of flexor pollicis longus tendon).

The same results of the previous healthy sample (longitudinal section of triceps muscle): window 3x3 is the most suitable window, and ADF outperforms in the speckle noise reduction, while LAMF has more ability in the edge preservation, see table (4-3) and figures (4-11,4-12) below.

Table (4-3) Evaluation of assessment metrics of hand musculoskeletal ultrasound image sample.

Metrics	3x3	5x5	7x7	9x9	11x11
SSI	0.994	0.949	0.836	0.900	0.776
SMPI	1.062	1.479	1.776	1.4521	1.954
EEI	0.979	0.899	0.804	0.967	0.767
MPSSI	0.001	0.012	0.022	0.013	0.028

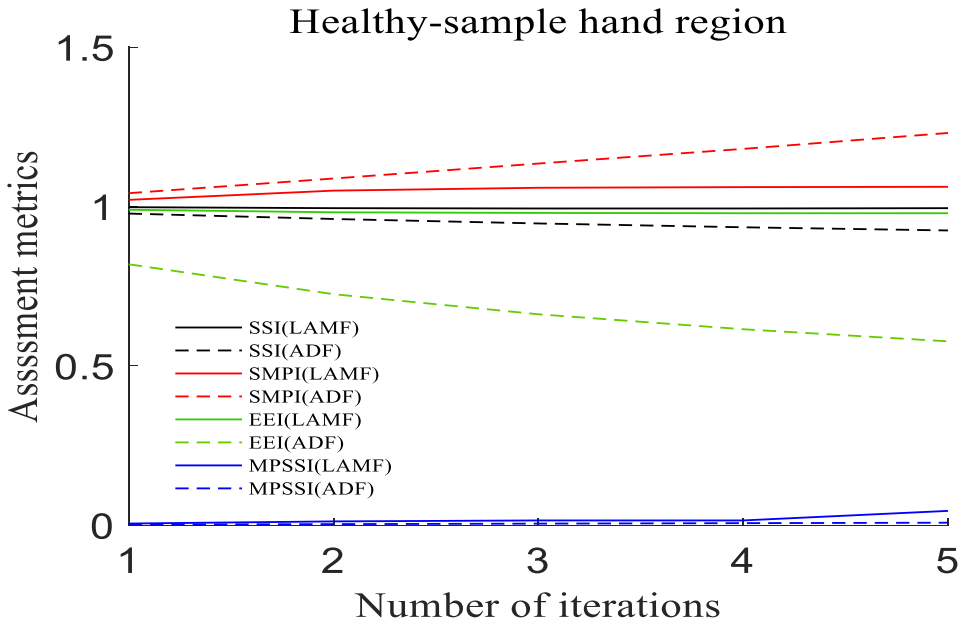

Figure (4-11) Comparison between performance of LAMF and ADF across (1-5) iterations when performing on cadaver musculoskeletal ultrasound image.

a ***b***

Figure (4-12) Healthy musculoskeletal ultrasound image (cross section of flexor pollicis longus tendon) after applying ADF is shown in figure (*a*), while figure (*b*) illustrates output image after applying LAMF.

Speckle noise was reduced in two different healthy image samples using ADF and LAMF. The enhanced musculoskeletal ultrasound images will support extraction of musculoskeletal parameters based on musculoskeletal ultrasound image of an individual.

4.1.8 Discussion

In this work, the Local Adaptive Median Filter (LAMF) was applied to three different samples of the musculoskeletal ultrasound images. Implementation steps of this filter were derived from Qiu, (2004), who applied this filter to SAR images and window sizes 3x3, 5x5 and 7x7. In this work, this filter was applied on these window sizes and expanded to the window size 9x9 and 11x11 to see any differences through increasing image details across window size. The performance of LAMF in all musculoskeletal ultrasound images shows a tendency to increase when using window size 3x3 compared with other window sizes (5x5, 7x7, 9x9 and 11x11) (see table (4-1), table (4-2) and table (4-3)). Therefore, 3x3 was chosen as a more suitable size for the performance of LAMF. The iterations are stopped when there is no significant change in the quality of speckle noise reduction. The performance of local adaptive median filter decreases when increasing the number of iterations; therefore, five iterations were chosen to show the behaviour of performance of this filter across several times of performing. One thing worth noticing from figure (4-5), figure (4-8) and figure (4-

11) is that the performance of the local adaptive median filter did not improve with increasing window size and number of iterations. Anisotropic Diffusion Filter (ADF) was utilized in this work to reduce the impact of the speckle noise on musculoskeletal ultrasound images to compare with LAMF on the same samples of these image at window size 3x3.

In the case of 3x3 window size and using ADF, the ultrasound image samples, which were collected from a cadaver and healthy triceps muscle had a high level of performance regarding speckle noise reduction (see figure (4-4) and figure (4-8)). On the other hand, the edge preservation reported high scores in all three-different samples using LAMF, see figure (4-4), figure (4-8) and figure (4-11). These results indicate that performance of ADF is better in speckle noise reduction, while LAMF outperforms ADF in edge preservation.

4.1.9 Conclusions

The results obtained from this part 1 show a competitive performance between the two filters (LAMF and ADF) in despeckling musculoskeletal ultrasound images. ADF is better than LAMF in speckle noise reduction, but with less ability in the preservation of the image edge. This could cause a trade-off between noise suppression and delineation of features of the image. Therefore, in this thesis ADF was selected to reduce the speckle noise of MUI. In addition, ADF filter was chosen as a pre-processing step in further applications in this thesis due to ADF having superior ability in speckle noise reduction compared with LAMF filter. These applications are measurements of triceps muscle thickness and evaluation of geometric parameters of a cross-section in the flexor pollicis longus tendon (cross-section area and circumference), see chapter 6.

4.2 Part 2: Contrast enhancement in the ultrasound image

4.2.1 Introduction

Musculoskeletal ultrasound data can be recorded from ultrasound devices as single images, panoramic images and ultrasound videos. As previously discussed, there are two limitations of the ultrasound imaging data: presence of speckle noise and low image contrast. Low image contrast has a negative impact on the quality of the subsequent data interpretation. However, contrast enhancement could be carried out during ultrasound image processing to overcome the problem as it could restore image details and clarify different tissue regions. Furthermore, image contrast enhancement was used in this project as a pre-processing step for further applications such as pennation-angle estimation.

Imaging systems in ultrasonography usually provide an option to adjust image contrast before acquiring the imaging data. While this adjustment is suitable for a single image, it is hard to control the movement of the ultrasound probe and the level of the contrast adjustment during an ultrasound video recording. In addition, adjustment of the ultrasound contrast enhancement depends mainly on the cumulative experiences of the operator rather than an objective analysis of imaging properties. Hence the performance of an ultrasound operator is variable among different directions and controlling any contrast adjustment of the ultrasound image remains difficult during video recording. Increasing image contrast by eye carries the risk that some data will be lost due to clipping of the histogram, reducing its suitability for further automated analysis. In this thesis, developing an objective method for ultrasound contrast enhancement was a successful solution to the above-mentioned problems and would provide support for the ultrasound applications.

In the previous published literature two approaches for image contrast enhancement were used: traditional and transformational approaches. Histogram Equalization (HE) and Non-Linear Unsharp Masking (NLUM) methods are two examples of the traditional approach. The traditional approach often involves linear and nonlinear filters. Histogram Equalization (HE) is a frequently used method which helps in improving image contrast. It has been widely used to enhance the contrast of ultrasound images and videos in a number of studies (Kim, & Chung, 2008; Cheng &. Shi, 2004; Choudhury & Medioni,2012; Rao, & Chen, 2012). Despite recent efforts to develop this method, it still suffers from some problems such as strengthening the contrast in all regions to the same level, including pixels which already have high contrast. Non-Linear Unsharp Masking (NLUM) (Ramponi et al., 1996; Panetta et al., 2011) is another traditional method that has been used to increase the quality of medical images (*e.g.* mammogram). It depends on nonlinear filters and logical operations between original images and resultant images after filtering. It is useful for illustrating important information on the medical image, but its drawbacks are that it can intensify noise and increase image contrast in all regions even if some regions do not need contrast enhancement.

The alternative transformational approach to image contrast enhancement focuses on analysing image contrast according to uncertainty and fuzzy representation rather than simply applying a uniform contrast enhancement. Using fuzzy transformational techniques can improve poor image quality by optimizing the parameters of the fuzzy membership function according to the image properties. The intuitionistic fuzzy sets and modification of fuzzy membership function techniques are two examples of this approach. Intuitionistic fuzzy sets method needs a thresholding step as a pre-processing step before fuzzification. Obtaining a proper value for this threshold is challenging in musculoskeletal ultrasound

images due to overlapping grey level intensities of many important musculoskeletal components. In terms of image contrast enhancement using modification of the fuzzy membership function, this technique inhibits noise and intensifies contrast because it optimizes parameters of membership functions based on the highest value of fuzzy entropy in an image.

The major constraint of these methods that it is fully dependent on the global assessment of the differences in image contrast and it is difficult to detect more specific ultrasound image details such as illumination differences between the edge and other image contents. An alternative is to adaptively transform the image according to the prevailing local image characteristics. Therefore, Local Fuzzy Contrast Enhancement (LFCE) was launched in this part as a new method for image contrast enhancement, which depends primarily on local rather than global evaluation of the image luminance. The LFCE technique handles the low contrast of the musculoskeletal ultrasound image, which depends on the local information between a pixel and its neighbours. The LFCE method relies on a fuzzy inference system and requires selected parameters to obtain high-level performance. Parameters are selected based on a contrast assessment metric, which gives a highest level of contrast at these parameters.

4.2.2 Related image contrast enhancement techniques

The modification of fuzzy membership function method is an alternative fuzzy technique, which has been applied previously to enhance image contrast, this technique involves the fuzzification and optimization of parameters of membership function of all grey level intensities of the image as the first stage. Then modification of the membership equation is performed in the second stage and the third stage is defuzzification.

In the fuzzification process, image data from spatial domain (grey level intensity of input image) is mapped to the fuzzy domain (grey level intensity between 0 and 1) using a membership function such as the one shown in equation (18) (Pal and R. A. King,1981).

$$\mu_A(Ixy) = \left(1 + \frac{Imax - Ixy}{Fd}\right)^{(-Fe)} \tag{18}$$

where the input image pixel is *Ixy* and *Imax* is a maximum grey level intensity of *Ixy*, *x* and *y* range over the image dimensions. *Fd* and *Fe* are parameters that determine the behaviour of the membership function. Tuning these parameters has an important influence on the performance of this technique. Optimization of *Fd* and *Fe* can be carried out using fuzzy entropy. The candidate values of *Fd* and *Fe* were chosen at maximum value of the fuzzy entropy (Agaian et al.,2000) because the largest value of fuzzy entropy means an image is heterogeneous, while low values denotes an image that has a large homogeneous region. Determining the best values for *Fd* and *Fe* can improve the membership function for the fuzzification. The calculation of the fuzzy entropy depends on the evaluation of Shannon's entropy as follows:

$$H(\mu_A(Ixy)) = \frac{1}{s_1 * s_2 * \ln(2)} \times \left(\sum_{y}^{Y}\sum_{x}^{X} S(\mu_A(Ixy))\right) \tag{19}$$

Where s_1 and s_2 are the overall dimensions of the image or video frame and S(.) is Shannon's entropy function, given by:

$$S(\mu_A(Ixy)) = -\mu(Ixy) \times \ln(\mu_A(Ixy) - \mu_A(Ixy) \times \ln\left(1 - \mu_A(Ixy)\right) \tag{20}$$

The second step is the modification of the membership function using the following equation:

$$\mu_A(Ixy)'' = 2 \times (\mu_A(Ixy) \qquad 0 \le \mu_A(Ixy) \le 1 \tag{21}$$

$$= 1 - 2 \times (1 - (\mu_A(Ixy))^2 \qquad 0.5 \le \mu_A(Ixy) \le 1$$

Using equation (21) achieves contrast intensification by increasing the contrast of the grey level intensities, which are above crossover point (0.5) and decreasing the contrast of the grey level intensities below 0.5. The last step is defuzzification to generate the output image (B_{xy}) using equation (22): -

$$B_{xy} = Fd\left(1 - \left(\mu_A(Ixy)^{"}\right)^{\frac{1}{Fe}}\right) + I_{max} \quad (22)$$

This technique has previously been used in several applications such as medical x-ray images (Tizhoosh et al., 1997), breast ultrasound images (Guo et al., 2006) and satellite images (Nair & Lakshmanan, 2011), but it has not so far been used on ultrasound videos and musculoskeletal ultrasound imaging.

For a comparative analysis two conventional contrast enhancement approaches can be used: Histogram Equalization method and Non-Linear Unsharp Masking method. Performing Histogram Equalization method depends on the histogram modification operations such as image stretching and shrinking to adjust histogram information (Cheng and Shi, 2004). In the case of using Non-Linear Unsharp Masking method, nonlinear filter and arithmetic operations are combined together to enhance image contrast. Nonlinear filter was involved to adjust grey level intensities of the image, while arithmetic operations (such as multiplication, subtraction…) between filtered image and input image was used to increase the possibility of the edges preservation (Panetta et al., 2011).

4.2.3 Assessment metrics of contrast image enhancement

Several “no reference” image quality assessment metrics can be used to determine the extent to which enhancement procedures have improved an image’s quality: Measure of Enhancement (EME) (Agaian et al.,2000; Agaian et al.,2001) Logarithmic Michelson Contrast Measure (AME) (Agaian et al., 2007) and second-derivative-like measure of

enhancement (SDME) (Panetta et al., 2011). These metrics are useful for no reference assessment measures that can be applied to ultrasound imaging when no absolute ground truth comparator image is available. The equations that describe these metrics are given in the table (4-4), below. In the application of these quantitative metrics, the input image must be divided into square blocks with odd dimensions, so the input image will consist of the number of the blocks, which are arranged in rows and columns depending on the block size. In the table (4-4), r_1 and r_2 represent the number of the blocks in the rows and columns respectively. g_{max} and g_{min} are the maximum and minimum grey level intensities values in each block respectively, while g_{center} is the centre pixel intensity in each block.

Table (4-4) Equations of three metrics (EME, AME and SDME).

Metrics	Definition
EME	$EME_{r_1 r_2} = \frac{1}{r_1 r_2} \sum_{e=1}^{r_1} \sum_{f=1}^{r_2} \left[20 \log \left(\frac{g_{\max,e,f}}{g_{\min,e,f}} \right) \right]$ (23)
AME	$AME_{r_1 r_2} = -\frac{1}{r_1 r_2} \sum_{e=1}^{r_1} \sum_{f=1}^{r_2} \left[20 \log \left(\frac{g_{\max,e,f} - g_{\min,e,f}}{g_{\max,e,f} + g_{\min,e,f}} \right) \right]$ (24)
SDME	$SDME = -\frac{1}{r_1 r_2} \sum_{e=1}^{r_1} \sum_{f=1}^{r_2} 20 \log \left[\frac{g_{\max,e,f} - 2g_{center,e,f} + g_{\min,e,f}}{g_{\max,e,f} + 2g_{center,e,f} + g_{\min,e,f}} \right]$ (25)

The strength of using EME, AME and SDME is not having to use ground truth image in the applying of these metrics on the output image. However, using these metrics requires dividing output image into a set of blocks where the dimensions of these blocks are odd and square. Selection of the best dimensions of the blocks is challenging, particularly in the case of complex texture pattern such as musculoskeletal ultrasound images, However, this point was addressed in this thesis. The best dimensions of the block were selected based on the

evaluation of the maximum entropy of selected block. Image entropy gives indication about distribution the image details, more details would record a higher level of entropy.

4.2.4 Local Fuzzy Contrast Enhancement Technique (LFCE)

The implementation of LFCE is based on a fuzzy inference system, it involves the usual three main steps: fuzzification, generation of fuzzy rules and defuzzification. The input to the first step is musculoskeletal ultrasound imagery (image or video) and involves constructing a 3x3 window (consisting of a central pixel and its immediate neighbours). The window systematically moves with a step of one pixel at a time around the image and repeats LFCE steps, see figure (4-13), this figure briefly illustrates the steps, which are used in the implementation of the LFCE method. There are three different types of membership function and 6 fuzzy inference rules in this technique. The main reason of constructing three different membership functions is to represent different levels of the image luminance (dark, grey and bright). Furthermore, construction of fuzzy rules of this method aimed to increase the difference of luminance between the central pixel of the window and its neighbours to enhance image contrast locally. In this method, if we supposed the central pixel is grey, neighbours are either dark or bright. Therefore, each level has two rules to improve the contrast between the central pixel and its neighbours. So, the total number of fuzzy rules of local fuzzy contrast enhancement method in this work is 6 fuzzy rules. Parameters (*Sd* and *Se)* control the behaviour of the fuzzy rules; estimation of these parameters depends on the evaluation of the quantitative SDME metric, see table (4-4). Prior to evaluation of SDME, a good block size is necessary in the evaluation of assessment metrics. The image is divided into a set of blocks (square and odd dimensions). The number of blocks in the image depends on the block dimensions. Evaluation of the entropy of each block was used as tool to detect which is the best block's dimensions.

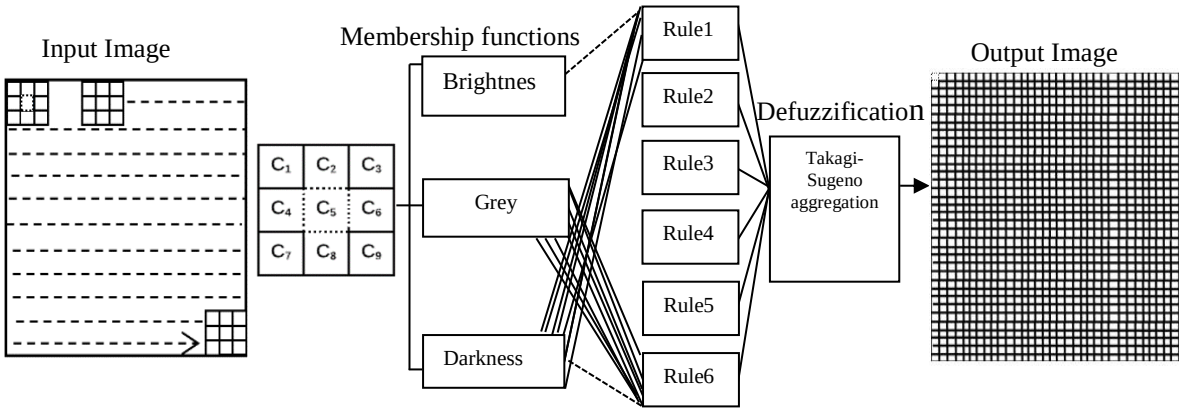

Figure (4-13) Applying LFCE on 3x3 sub-image (central pixel and its neighbours) around the image. Connection between central pixel and its neighbours, which are illustrated in rule 1 and rule 6. In rule1, the central pixel was fed up from brightness membership function, while neighbours pixels are taking from darkness. In case of rule6, the central pixel was fed up from darkness and its neighbours pixels were fed up from grey level membership function.

An algorithm is introduced to show the sequence of the instructions to implement LFCE technique. This algorithm consists of two parts; the first one presents the estimation of the block size and the parameters of the fuzzy rules (*Sd* and *Se*). The second part of the algorithm gives a review of the performing LFCE technique using these parameters. *Sd* and *Se* parameters control the behaviours of the fuzzy rules. Through the *Sd* parameter, we attempt to make the central pixel brighter than neighbours pixels to increase the difference of luminance between them. On the other hand, *Se* parameter tends to pull central pixel to the darkness region and make a difference between it and its neighbours.

Algorithm: Part I, estimation parameters for local fuzzy contrast enhancement method

1 Start.

2 Input image let i=1 and j=1;

3 Select a block-size from the set of block-sizes based on the evaluation of image entropy.

4 Set up Se_n values (n=1,2….40 values).

5 Set up Sd_n values (n=1,2….40 values).

6 Input $Se_{j.}$

7 Input $Sd_{i.}$

8 Start with the first pixel and construct window 3x3.

9 Fuzzification using three membership functions (dark, grey and bright).

10 Apply 6 rules on this window.

11 Defuzzification using Takagi-Sugeno method.

12 Go to step 9 and move to next pixel and construct another window.

13 Calculate SDME.

14 Set $i=i+1$.

15 While $i \leq 40$, go to step 7 (choosing another value of *Sd*)

16 Let i=1, j=j+1

17 While $j \leq 40$, go to step 6 (choosing another value of *Se*)

18 Save the values of (*Se*,*Sd*) parameters at maximum value of SDME.

19 Stop.

Algorithm: Part II, implementation of local fuzzy contrast enhancement method using parameters

1 Start.

2 Input image, block size and values of *Sd* and *Se* parameters.

3 Start with first pixel and construct window 3x3.

4 Fuzzification using three membership functions (dark, grey and bright).

5 Apply 6 rules on this window.

6 Defuzzification using Takagi-Sugeno method.

7 Go to step 4 and move to next pixel and construct another window.

8 Display output image.

9 Quantitative analysis between input image and output image using EME, AME and SDME.

10 Stop

Figure (4-14) below shows the selection of best values of the *Sd* and *Se* parameters-based evaluation on the maximum value of SDME as explained in the algorithm -part 1 above.

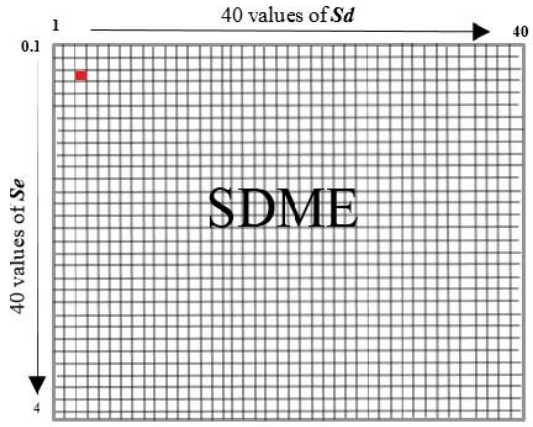

Figure 4-14), illustrates the selection of the best values of the *Sd* and *Se* parameters-based on evaluation the maximum value of the SDME. As example, the red square color represents the maximum value of the SDME at (Sd_3,Se_3), so it is possible to extract the figure of (*Sd* against SDME) when *Sd*=3 and set of *Se* (40 values), also extraction the figure of (*Se* against SDME) when *Se*=0.3 and set of *Sd* (40 values).

4.2.4.1 Fuzzification

There are three membership functions in the LFCE technique. These functions work to map grey level intensities from the spatial domain [I_{min} , I_{max}] to fuzzy domain values between 0 and 1, where I_{min} and I_{max} are minimum and maximum grey level intensities in the input image. The first membership function gives a high membership degree for pixels, which have a low grey level intensity (darkness), while the second function, presents grey level membership as triangle function, which centred at middle grey level intensity in the image. The third function introduces high membership degree for pixels, which have a high grey level intensity (brightness). Figure (4-15), illustrates three membership functions.

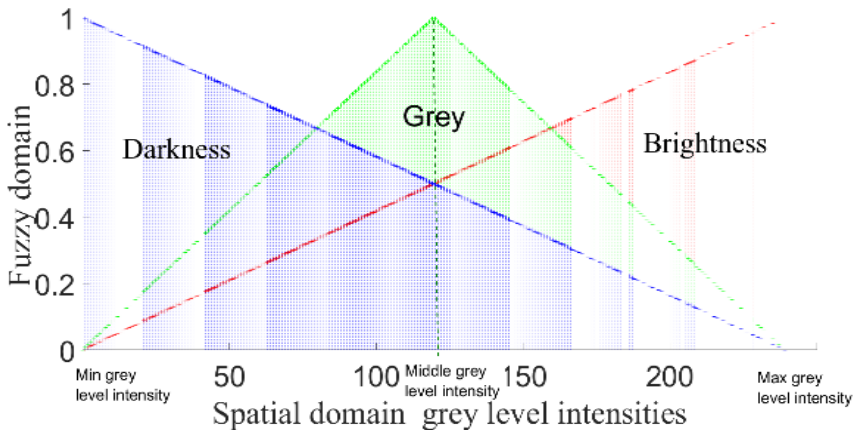

Figure (4-15) illustrates three membership functions, function in blue color represents darkness membership function, while in red color represents brightness membership function and function in green shows grey membership.

4.2.4.2 Generation of fuzzy rules

Fuzzy rules are constructed from the combination of IF-THEN sentences and a set of logic connecters such as (AND, OR and NOT). The part of the sentence after IF is called antecedent (rule weight), while the second part after THEN is the consequence (output level). The six fuzzy rules used in the LFCE technique are applied on 3x3 pixel template (mask of central pixel and a given neighbourhood in the original image) as shown in the figure (4-16) below:

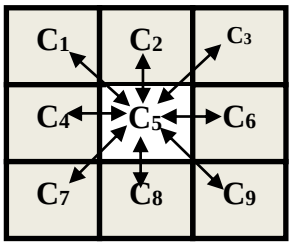

Figure (4-16) Representation of central pixel (C_5) and its neighbours (C_1, C_2, C_3, C_4, C_6, C_7, C_8, C_9), fuzzy rules will be applied on C_5 and each neighbour's pixel and then combining together to get the final decision.

Some of fuzzy rules are shown below and the rest of these rules are in the appendix III : -

Rule 1: If (central pixel (C_5) is brightness AND C_1 is darkness) OR

(central pixel (C_5) is brightness AND C_2 is darkness) OR

(central pixel (C_5) is brightness AND C_3 is darkness) OR

(central pixel (C_5) is brightness AND C_4 is darkness) OR

(central pixel (C_5) is brightness AND C_6 is darkness) OR

(central pixel (C_5) is brightness AND C_7 is darkness) OR

(central pixel (C_5) is brightness AND C_8 is darkness) OR

(central pixel (C_5) is brightness AND C_9 is darkness) THEN

$Z = Sd \times Y$

...

Rule 6: If (central pixel (C_5) is darkness AND C_1 is grey) OR

(central pixel (C_5) is darkness AND C_2 is grey) OR

(central pixel (C_5) is darkness AND C_3 is grey) OR

(central pixel (C_5) is darkness AND C_4 is grey) OR

(central pixel (C_5) is darkness AND C_6 is grey) OR

(central pixel (C_5) is darkness AND C_7 is grey) OR

(central pixel (C_5) is darkness AND C_8 is grey) OR

(central pixel (C_5) is darkness AND C_9 is grey) THEN

$Z = Y - Se$.

The action of the consequents of the fuzzy rules are determined by two parameters (*Sd* and *Se)*, which then deliver the final output *Z* for this pixel and *Y* represent central pixel. There

are three fuzzy rules that use the *Sd* parameter (rule1, rule3 and rule5) and the same number of rules that use the *Se* parameter (rule2, rule4 and rule6). Through the Sd parameter, we attempt to make the central pixel brighter in terms of neighbouring pixels i.e. the final output $Z = Sd \times Y$. (The range of the *Sd* parameter is between 1 and 4 (40 values)). In the case of the *Se* parameter, the effect is to reduce the pixel intensity relative to its neighbouring pixels i.e. the final output $Z = Y - Se$. (Parameter *Se* also has a range between 1 and 40 (40 values)). The variation of both parameters (*Sd* and *Se*) are more sensitive to the range of 40 values. Tuning *Sd* and *Se* can be carried out by evaluating the SDME metric of the output image, see the algorithm:-part I.

4.2.4.3 Defuzzification

There are two types of defuzzification methods in the fuzzy inference system: Mamdani (Mamdani, 1974) and Takagi-Sugeno (Takagi & Sugeno, 1985). Takagi-Sugeno is more flexible than Mamdani because Mamdani needs fuzzy crisp output, while the output of Sugeno is only crisp value. Furthermore, Takagi-Sugeno has a better processing time than Mamdani; therefore Takagi-Sugeno was used to achieve defuzzification of the LFCE technique using following equation: -

$$Final\_output = \frac{\sum_{i=1}^{N} W_i Z_i}{\sum_{i=1}^{N} W_i} \tag{26}$$

where *N* is number of rules, *W* is rule weight and *Z* is output level which depends on *Sd* and *Se*. For example, in the case of rule1, the rule weight (W_1) is (central pixel (C_5) is brightness and neighbour (C_1) is darkness) or (central pixel (C_5) is brightness and (C_2) is darkness) or…or (central pixel (C_5) is brightness and neighbour (C_9) is darkness). While, output level

of this rule is $Z = Sd \times Y$, where Y represents grey level intensity of particular pixel (central pixel of the mask in the original image).

4.2.5 Experimental results

This section describes performing of three experiments, which used different kinds of input data. The input data of the first experiment are five ultrasound image samples which were collected from the arm region (protocol 1) of the healthy volunteers; whereas, the second experiment used four ultrasound videos which were collected from hand region of the healthy volunteers (protocol 2), all details in section 3.3.2.1. Lastly, the input of the third experiment are five ultrasound image samples which, was collected from shoulder region of a cadaver in the form a panoramic ultrasound image, all details in section 3.3.1. All processing steps of the (LFCE) were applied on the data obtained from the three experiments. The main purpose of using different data is to assess the performance of LFCE method on these data and shed light on the sensitivity of the contrast detection using LFCE method compared with other methods. Comparison with results of other methods such as Unsharp Masking (UM), Histogram Equalization (HE) and Image contrast enhancement based on the fuzzy technique are presented below. Quantitative no-reference assessment metrics were employed to examine the performance of each of the contrast enhancements methods.

4.2.5.1 Experiment 1

The LFCE method was applied to the 5 ultrasound image samples. All the processing steps of the LFCE are explained in detail below in the case of sample 1. Fuzzification is the first step of the LFCE method; three membership functions (darkness, grey and brightness) were used, see figure. (4-15). The next step is applying the fuzzy inference rules (as described in section 4.2.4.2), but before using these rules, and to get the best values obtained for *Sd* and

Se, the SDME metric was involved in the estimation of these parameters. The evaluation of SDME needs suitable dimensions for the block size to determine the values of r_1 and r_2 , see table (4-4). The size of the block should be square and odd, but within these constraints to objectively determine a good block-size image entropy can be used. By using entropy, the best values obtained for dimensions of block were selected according to the average content of information. For example: if a block covers a homogenous region, this means it has less details because it shows just a small change in the grey level intensity; while, in the case of a heterogeneous region, a high level of information could be observed at the specific block size. Therefore, it is possible to use entropy as a tool to measure, which block size is more informative than others. The suitable selection of block size has a significant impact on the assessment of the contrast improvement. Maximum entropy denotes a high level of information; so, the block size chosen was the one that delivered maximum entropy. The block size determines how many blocks are in a row and column, figure (4-17), demonstrates the selection of the block's dimensions at maximum entropy in the case of sample 1.

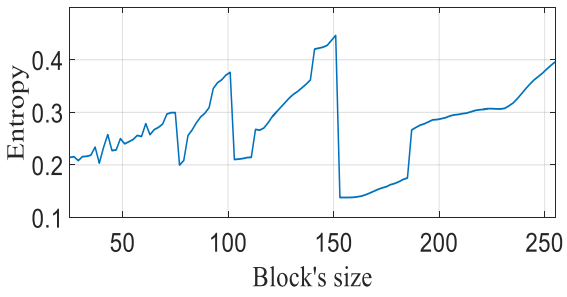

Figure (4-17) illustrates selection the best value of block size, the dimensions of the input image after cropping to select region of interest are [305,559], and the optimum block size is 151; this means image is divided into 5 blocks and these blocks distributed across two rows (r_1=2) and three columns (r2 = 3).

The SDME of the contrast enhanced output image was performed for every change in *Sd* value (40 values) at the first value of *Se*. Then the process is repeated at the second value of

Se until all *Se* values have been used. The best values obtained for *Se* and *Sd* were selected such that they maximize SDME (see the algorithm, part I). Figure (4-18) demonstrates the estimation of *Sd* and *Se* of sample1. After getting the best values obtained for *Sd* and *Se*, it is possible to carry out the fuzzy rules, which are used to perform local contrast enhancement of the musculoskeletal ultrasound image. The last step is defuzzification involving a Takagi and Sugeno aggregation method, see equation (26). Comparisons between input image, output of LFCE method and FCE (Fuzzy Contrast Enhancement) or GFCE (Global Fuzzy Contrast Enhancement), HE and NLUM methods are all shown in figure (4-19). Table (4-5), illustrates the evaluation of three metrics EME, AME and SDME for all five samples used in experiment 1, also shown are the best values of *Sd* and *Se* for these samples and the number of rows and columns (r_1 and r_2) respectively. Good image contrast corresponds to having high scores of SDME and EME and a low score for AME. Image contrast was enhanced using LFCE method and the resultant image of LFCE gives the highest score of SDME and is approximately 34% greater than other GFCE, see table (4-5).

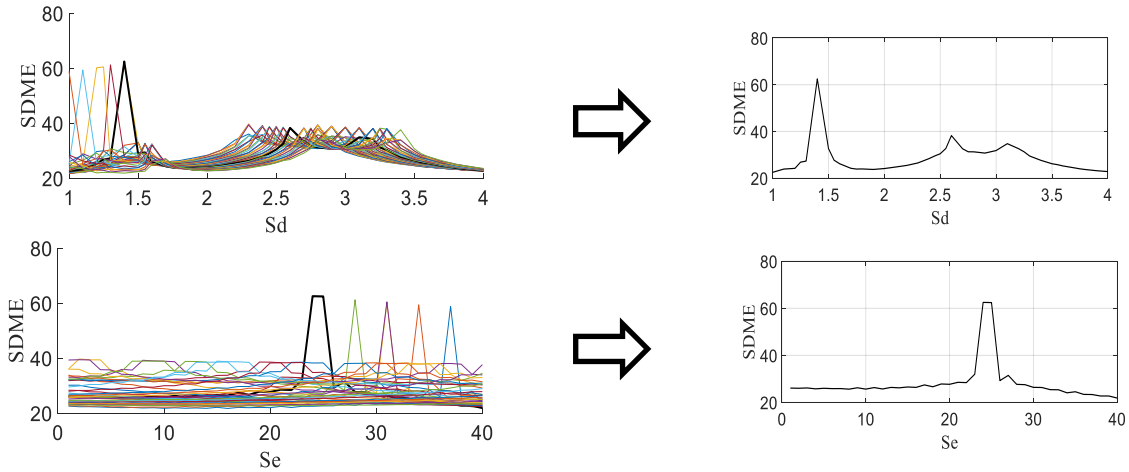

Figure (4-18), the left hand side of this figure illustrates the estimation of *Sd* and *Se* and different colors depict the SDME values across different values of *Sd* and *Se*, while the right hand side represents illustration of the proper values of *Sd* and *Se* at maximum value of SDME in separated figure (*Sd*=1.4 and *Se*=25 of sample1).The evaluations of left and right side based on the figure (4-14).

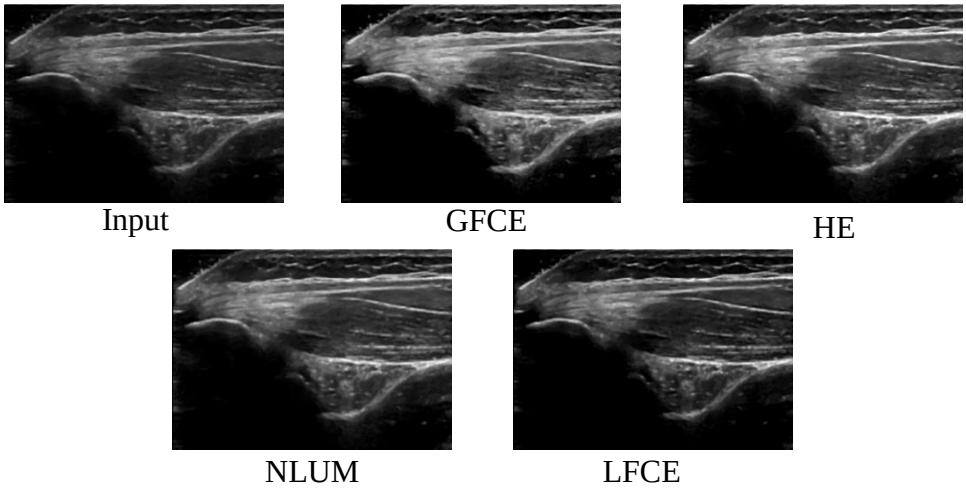

Figure (4-19), the first line illustrates input image of sample 1 and this image after applying GFCE (Global Fuzzy Contrast Enhancement technique) and HE respectively, while the second line shows input image after applying NLUM and LFCE respectively.

Table (4-5) The values of three metrics (EME, AME and SDME) of five samples of musculoskeletal ultrasound image's samples. Image contrast was enhanced using LFCE method and the resultant image of LFCE gives the highest score of SDME and is approximately 34% greater than other GFCE.

Samples	Metrics	Input	GFCE	HE	NLUM	LFCE	Se	Sd	r_1	r_2
Sample1	EME	289.81	291.05	295.03	293.35	295.03	25	1.4	2	3
	AME	0.00020	0.00019	0.00015	0.00017	0.00015				
	SDME	31.07	24.72	17	24	43.44				
Sample2	EME	292.43	294.23	295.03	292.50	295.03	19	2.8	1	3
	AME	0.00019	0.00015	0.00015	0.00017	0.00015				
	SDME	16.06	7.79	20.16	17	25.77				
Sample3	EME	252.74	289.36	255.78	254.26	291.25	10	2.6	2	3
	AME	0.069	0.00023	0.0785	0.0870	0.00021				
	SDME	13.85	19.88	17.56	15.40	31.27				
Sample4	EME	291.92	293.09	295.03	109.83	295.03	4	3.15	1	3
	AME	0.00018	0.00017	0.00015	0.00016	0.00015				
	SDME	13.46	25.84	18.2	14.99	26.43				
Sample5	EME	288.10	291.25	292.60	290.67	293.05	40	2.9	2	3
	AME	0.0002	0.00019	0.00018	0.00002	0.00017				
	SDME	14.39	16.55	19.94	16.27	17.34				
Mean of SDME		17.7	19	18.5	17.5	28.85				

4.2.5.2 Experiment 2

In this experiment, the source for the ultrasound imaging data is ultrasound video. The video consists of a set of frames that can be regarded as a set of ultrasound images. The same steps

described in the experiment 1, above, were employed on each single frame of video. However, selection block size was performed on just four randomly selected frames of video, figure (4-20) shows the mean of the entropy of four video frames at different block sizes.

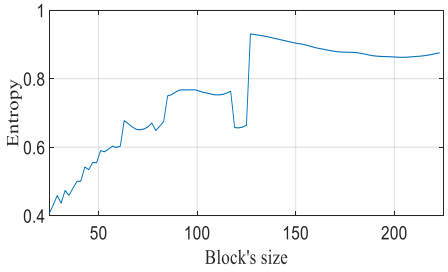

Figure (4-20) illustrates the selection of the block size, but in this figure the value of the entropy represents the mean value of the entropy of four frames (frames 5,50,75,90) in the case of sample 1. The dimensions of the input frame after cropping are [254,271], and the proper block size that was determined is 127; therefore, the number of the rows (r_1) equals 2 and the number of the columns (r2) equals 2.

Parameters (*Sd* and *Se*) were selected in all frames. Figure. (4-21) shows extraction set of *Sd* and *Se* parameters alongside 120 frames of video (sample1).

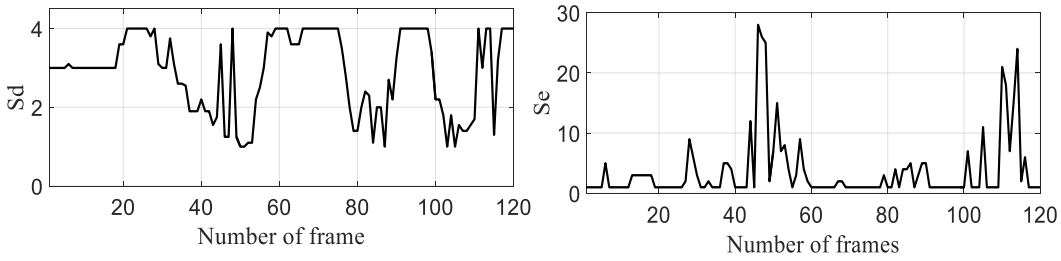

Figure (4-21), the left-hand side of this figure presents the proper values of *Sd* alongside the video frames (120) of sample1, while the right-hand side illustrates the set of *Se* parameter after estimation of the same video sample.

Figure (4-22) illustrates *Sd* and *Se* estimation in two frames (frame 46 and frame 88) which were selected randomly from samp1e (video) as examples. Figure (4-23) shows the comparison SDME evaluation for 120 frames after applying the LFCE method and the GFCE method on the video of sample 1 (120 frames). The figure shows the performance of

GFCE method is better than LFCE in most frames. On the other hand, figure (4-24) shows a comparison of SDME evaluations on input video (120 frames) and after applying (LFCE, HE and NLUM methods) on these input frames. As shown in figure (4-24), there is a significant difference in the performance between LFCE method based on the SDME evaluation and the input video, HE, and NLUM method. Therefore, the competition in the performance is mostly between LFCE and GFCE methods. In terms of mean values of SDEM in the table (4-6), it is only 5% of the GFCE's performance that outperforms the LFCE's performance.

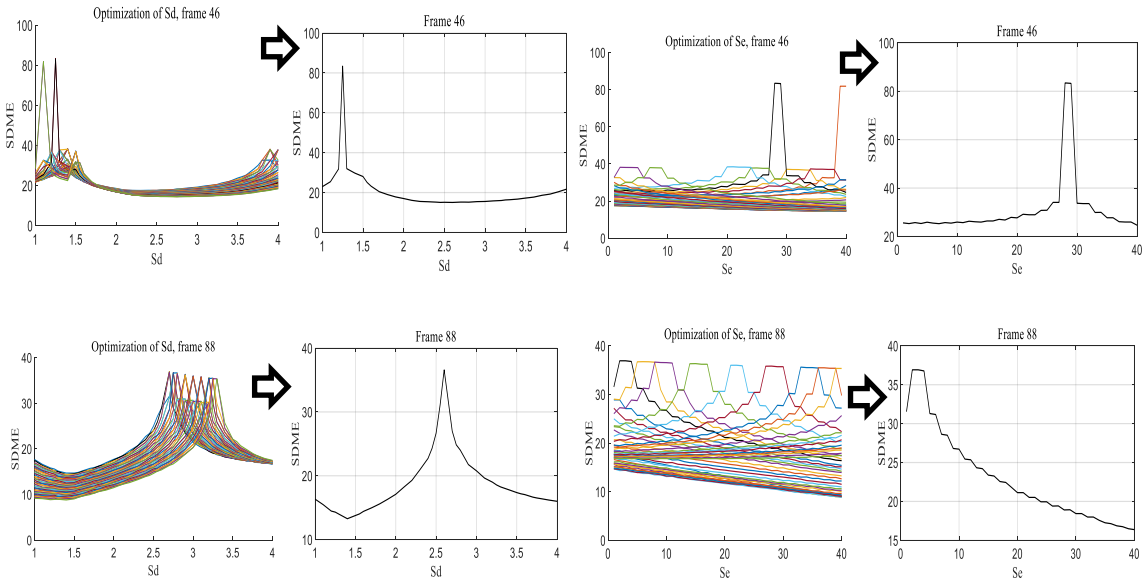

Figure (4-22) shows estimation of *Sd* and *Se* of two frames (46 and 88) of sample 1, different colors depict the SDME values across different values of *Sd* and *Se*. Furthermore, the separated figure shows *Sd* value of frame 46 (*Sd* =1.2) and frame 88 (*Sd*= 2.7) at maximum value of SDME. In terms of evaluation of *Se* value in frame 46 equals 27, while in frame 88 equals 3 at maximum value of SDME. The evaluations of left and right side based on the figure (4-14).

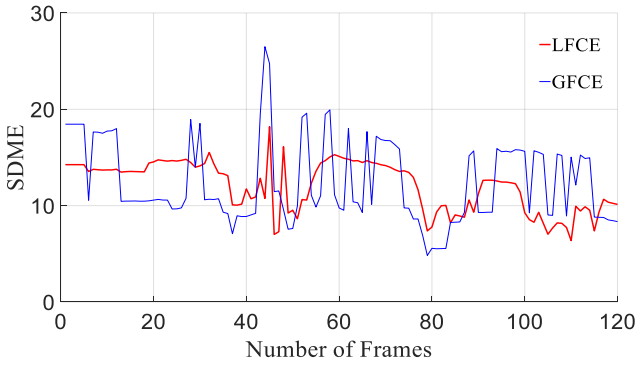

Figure (4-23) Evaluation of SDME for video using LFCE method and GFCE of sample 1.

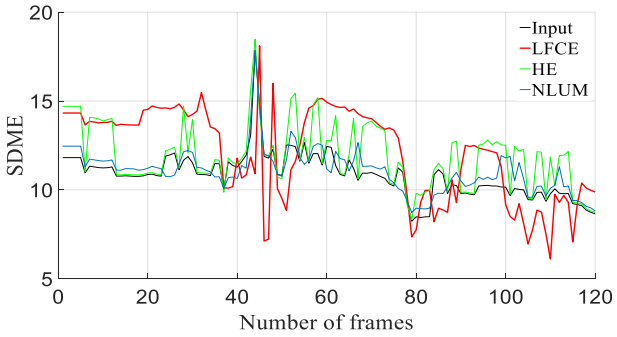

Figure (4-24) Evaluation of SDME for video of different methods of contrast image enhancement (Input, LFCE, HE and NLUM) of sample 1 in the experiment 2.

One frame of sample 1 video was used as an example in figure (4-25). The resultant images of each of the contrast enhancement methods are illustrated in this figure. Table (4-6), presents the values of three metrics (EME, AME and SDME) and for four samples of musculoskeletal ultrasound video. these values represent the mean value of all frames in the video sample.

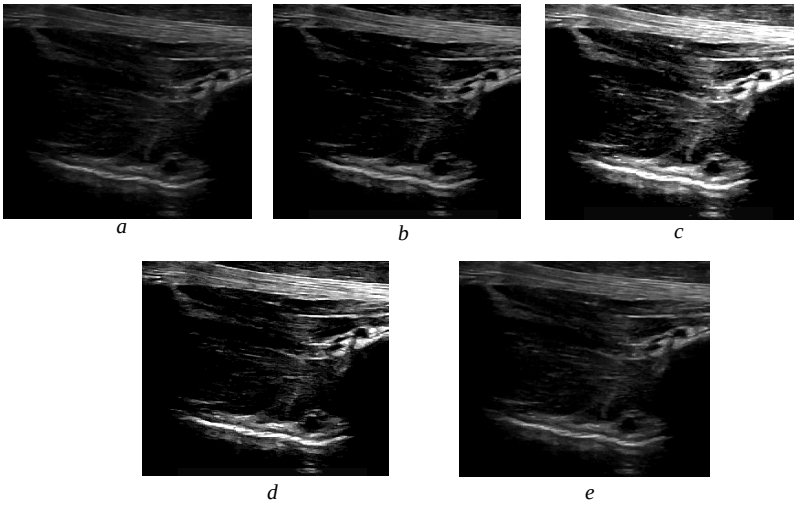

Figure (4-25) In the first line, figure (*a*, *b*, and *c*) from left to right illustrate frame 88 of input video, after applying GFCE, and HE methods on this frame, while the second line (*d* and *e*) shows this frame after applying NLUM and LFCE (block's size=127, *Se*=3 and *Sd*=2.7)).

Table (4-6) illustrates the mean values of three metrics (EME, AME and SDME) for all frames of four samples of musculoskeletal ultrasound video.

N	Metric	Input	GFCE	HE	NLUM	LFCE	r_1	r_2
1	EME	252.53	282.72	294.63	291.64	294.34		
	AME	0.0013	0.0678	0.00016	0.00018	0.00016	2	2
	SDME	10.83	15.23	11.90	11.06	12		
2	EME	248.022	290.52	294.99	291.46	295.03		
	AME	0.00017	0.00019	0.00015	0.00019	0.00015	2	2
	SDME	10.88	13.83	14.80	12	11.82		
3	EME	143.7	258.25	294.63	291.23	295.03		
	AME	0.00001	0.3274	0.00016	0.00019	0.00015	2	2
	SDME	4.17	13.04	9.77	9.38	12.58		
4	EME	250.49	289.46	294.60	292.64	295.03		
	AME	0.0014	0.00002	0.00016	0.00017	0.00015	2	2
	SDME	8.54	10.41	8.73	8.61	13.24		
Mean of SDME		8.6	13.12	11.3	10.47	12.41		

4.2.5.3 Experiment 3

The input image of this experiment was collected from an advanced ultrasound machine and the captured panoramic image is superior (in terms of minimum contamination by noise) than the input images from earlier experiments. Optimization of the block size is a necessary

step before evaluating SDME. Entropy was used to get the optimum block size based on the input image. Figure (4-26) demonstrates evaluation of entropy at different block's size.

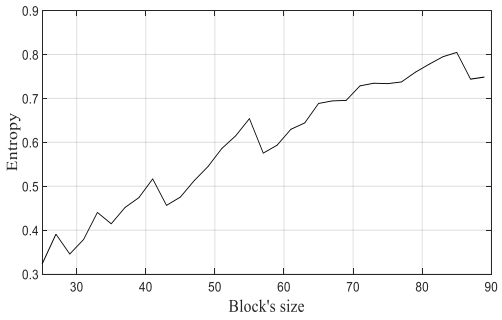

Figure (4-26) Selection of block size, the dimensions of input image after cropping are [170,772], and the optimum block size is 85; therefore, number of rows (r_1) equals 2 and number of columns (r2) equals 9.

After getting the proper dimensions of the block, we can divide the image into blocks which are arranged in the rows and columns. This is requisite step to evaluate SDME, see equation. (25) in table (4-4). The figure (4-27) shows estimation of *Sd* and *Se* respectively.

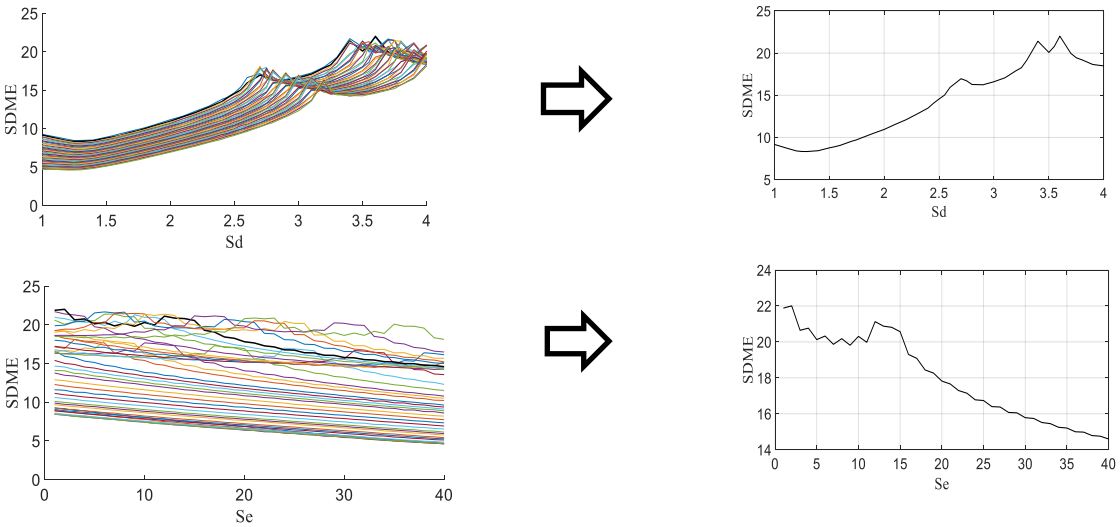

Figure (4-27), the left-hand side of this figure illustrates the estimation of *Sd* and *Se* and different colors depict the SDME values across different values of *Sd* and *Se*, while the right hand side represents illustration of the proper values of *Sd* and *Se* at maximum value of SDME in separated figure. So, *Sd*=3.6 and *Se*=2 of sample 1. The evaluations of left and right side based on the figure (4-14).

The difference between the output images of (GFCE, HE, NLUM and LFCE) methods including input image are shown in figure (4-28) below. The performance of each contrast enhancement method can be seen in the output panoramic ultrasound images in this figure.

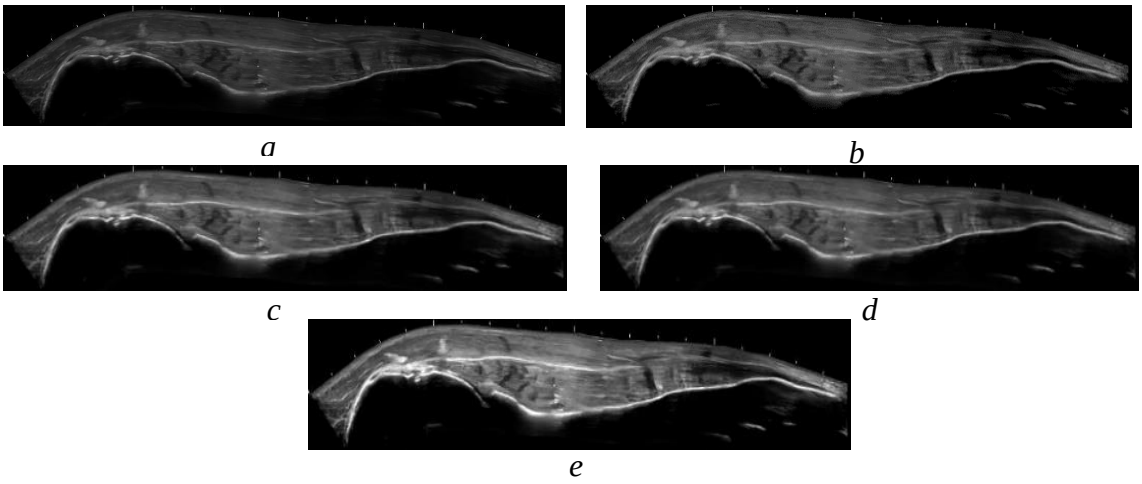

Figure (4-28), from top to bottom: the input image from the cadaver is shown in figure (*a*), while figure (*b)* shows this image after applying GFCE method. The image in figure (*c*) shows the result after applying HE, while figure (*d*) is input image after applying NLUM method. Finally, figure (*e*) illustrates contrast image enhancement using LFCE method.

In this experiment, the same procedure and steps were employed on each of the four remaining samples. Table (4-7), presents a quantitative evaluation of three assessment metrics (EME, AME and SDME) in all contrast enhancement methods.

Table (4-7) The values of three metrics (EME, AME and SDME) of five samples of panoramic musculoskeletal ultrasound image. It is 31% of the LFCE's performance outperforms GFCE's performance.

Samples	Metrics	Input	GFCE	HE	NLUM	LFCE	Se	Sd	r_1	r_2
Sample1	EME AME SDME	285.19 0.0002 9.4876	288.12 0.0017 15.64	292.89 0.0002 13.9792	287.82 0.0002 10.50	294.35 0.00016 22.006	2	3.6	2	9
Sample2	EME AME SDME	288.59 0.0002 29.43	290.34 0.00019 32.05	294.81 0.00016 37	291.34 0.00018 32.67	294.88 0.00015 33.65	11	2.7	2	9
Sample3	EME AME SDME	289 0.0002 33.26	290 0.00019 66.47	295 0.00016 60.66	291.56 0.00019 40	295 0.00015 68.75	4	2.9	1	9
Sample4	EME AME SDME	288.76 0.0002 21.2	289.38 0.0002 30.6	295 0.00015 24.89	291.37 0.00018 23.02	295 0.00015 54.7	2	3.6	1	4
Sample5	EME AME SDME	288.5 0.0002 38.55	61.7 1.8277 47.55	295.03 0.00015 47.37	290.89 0.0019 51.26	295.03 0.00015 64.62	3	2.1	1	9
Mean of SDME		26.38	38.44	36.77	31.49	48.74				

Although the output images of the GFCE, HE and NLUM methods improve the image contrast compared to the input image, based on the mean values of SDEM in the table (4-7) the performance of LFCE outperforms them approximately by 31%.

4.2.6 Discussion

The prevailing demand of the contrast enhancement process is to improve the appearance of the image for human visual perception and aid the automated interpretation of these images in the further processing. In this work, a novel method (LFCE) was introduced to enhance the contrast of the MUI locally. The LFCE method was employed on a number of different samples of data that used three separate experimental data acquisition modalities before enhancing the contrast of the MUI. The data from experiment 1 and experiment 2 were collected from healthy volunteers using the same ultrasound machine; a single ultrasound image was the input of expeiment 1 and a set of the ultrasound images (captured in the form of an ultrasound video) was the input of experiment 2. Comparing the results of these two

experiments illustrates the importance of intra-scan variability during the ultrasonographer's use of the video scanning modality. Hence, video data is more variable and challenging than a single image snapshot: due to the need to keep a probe perpendicular on the surface of the scan area. Adjusting contrast during recording could distract an ultrasonographer. Currently, there is no ultrasound machine option to adjust the ultrasound video after recording. In the third experiment, different input modality was presented from the first and the second experiments; it is a set of ultrasound images fused together to give an expanded view (i.e. a panoramic musculoskeletal image).

The most important step in the LFCE approach is the construction of the fuzzy rules. The fuzzy rules are composed of fuzzy conditional statements, which in this case reflect the knowledge of how to address low luminance in localised regions of the image. The *Sd* and *Se* parameters steer the evaluation by influencing the output level of the fuzzy rules, and the best values for these parameters were chosen at maximum values of SDME.

The evaluation of the image SDME's requires a good block size for a sliding window to traverse the rows and columns (r_1 and r_2) of an input image. The entropy of the image was used to investigate which block size delivers the best variation in grey level intensity for an input image. Based on the nature of the musculoskeletal ultrasound images, a small size of the block is likely to consist of homogenous grey level intensities and it is hard to show the discrimination in the luminance of the image. Therefore, a large block size might be a more appropriate selection to better recognize the difference in image contrast. However, it is necessary to cover most of the image pixels when dividing images into a set of blocks for the sliding window. The best block size uses odd square dimensions for the evaluation of the SDME metric. In the three experiments, the block size was selected successfully. However, the number of blocks which were arranged in columns in the third experiment is greater than

in the experiment 1 and 2. This is due to the high quality and resolution of image acquisition in experiment 3 compared to experiments 1 and 2. Parameters (*Sd* and *Se*) in all three experiments were selected based on the SDME evaluation. These parameters were extracted in all frames of four samples of the experiment2. Despite detecting the proper set of these parameters in this experiment, it is time consuming; this is one limitation of using LFCE, which needs to be considered.

The quantitative assessment of the image quality illustrates the difference in the performance between LFCE and GFCE, HE and NLUM. Three quantitative metrics were used for this purpose EME, AME and SDME. There is little variation in the values of EME and AME for all experiments and methods.

The LFCE approach (local method) performed considerably better than GFCE method (global method) in experiment1 and experiment3. Based on the mean values of the SDME of the five samples for both GFCE and LFCE methods in the table (4-5) and table (4-7), the performance of LFCE outperforms the performance of GFCE by 34% in the experiment 1, and in the experiment 3 by 12%. Whereas, in the experiment 2, LFCE method a high score of the mean values of the SDME was reported, compared with the mean values of the SDME of the GFCE method, but not in the all frames of the ultrasound video, see figure (4-23).and figure (4-24). The scenarios where LFCE works reasonably well are single and panoramic ultrasound images. This is due to the nature of the local interaction between grey level intensities between the image's pixels and ultrasound video that has a higher level of variation compared with single and ultrasound panoramic images. Therefore, the LFCE method might lack the ability to avoid the high level of variabilty in the case of ultrasound video imaging.

The proposed method has some limitations: although LFCE was performed on all three experiments (14 samples in all), it is still a small sample number in terms of appraising LFCE. Moreover, choosing a large block size for the mask (central pixel and its neighbours) might have a different impact on MUI contrast enhancement compared with a small size.

The second limitation is related to qualitative assessment. The assessment of image contrast of all methods in this work does not include any of the subjective metrics such as Mean Opinion Score (MOS) (Huynh-Thu et al., 2007). This metric is a descriptive tool which reflects the opinions of a group of experts in the same field of research. It is a potential subjective tool to show the acceptance of the results in terms of quality and applicability.

4.2.7 Conclusions

In this work, a novel method to increase the quality of MUI was introduced. It is an automated method and depends on local analysis of low-level luminance in the image and the principles of a fuzzy inference technique. In general, the performance of contrast image enhancement was improved by this technique when applied to three different input data of MUI (single image, video and panoramic image). Since it is difficult to adjust the contrast during video recording in MUI, contrast enhancement would provide a great help for clinicians, researchers and ultrasonographers during an ultrasound video recording as it is possible to enhance offline video recording.

Ultimately, the contrast was enhanced to increase the quality of the musculoskeletal ultrasound images. Obtaining the best image quality helps to get a better estimate of the musculoskeletal parameters automatically.

Chapter Five

Edge detection in Musculoskeletal Ultrasound Images

The first part of this chapter was published as a peer-reviewed conference paper:
Jabbar S I., Day C. R., Heinze, N. and Chadwick, E.K. (2016). Using Convolutional Neural Network for Edge Detection in Musculoskeletal Ultrasound Images. *In IEEE International Joint Conference on Neural Networks(IJCNN).* pp. 4619–4626.

The second part of this chapter is submitted as journal publication and it is currently under review.

Chapter 5 Edge detection in musculoskeletal ultrasound images

5 Introduction

The determination of musculoskeletal geometric parameters is a solid foundation of musculoskeletal modelling. Some of these parameters are muscle thickness, muscle fibre length and pennation angle, which describe the morphology of the muscular system. The estimation of these parameters in vivo is highly desirable, especially when a Musculoskeletal Ultrasound Image (MUI) is captured, which could help in the construction of personalised musculoskeletal modelling.

Image segmentation is an essential step in the identification of the geometric parameters as image segmentation can change an image contents representation to a simple form. This processing could help in differentiation between image sections and make it meaningful.

Edge detection is a fundamental prerequisite for successful image segmentation. It outlines the important details of an object in the image and mark it as high brightness colour (255), while leaving the rest of the image with 0 intensity. In this thesis, edge detection technique was chosen to characterise objects in the musculoskeletal ultrasound image. The main challenge of performing this technique is the difficulty to get a clear image of muscles and tendons. This is due to the different texture patterns of the MUI and presence of speckle noise in this kind of image. Figure (5-1), illustrates a typical scenario of extraction of musculoskeletal parameters, which starts with scanning the upper limb segments by ultrasonography, to image processing which includes image enhancement, edge detection and extraction of information from the image. These steps facilitate determining the important parameters of the musculoskeletal model.

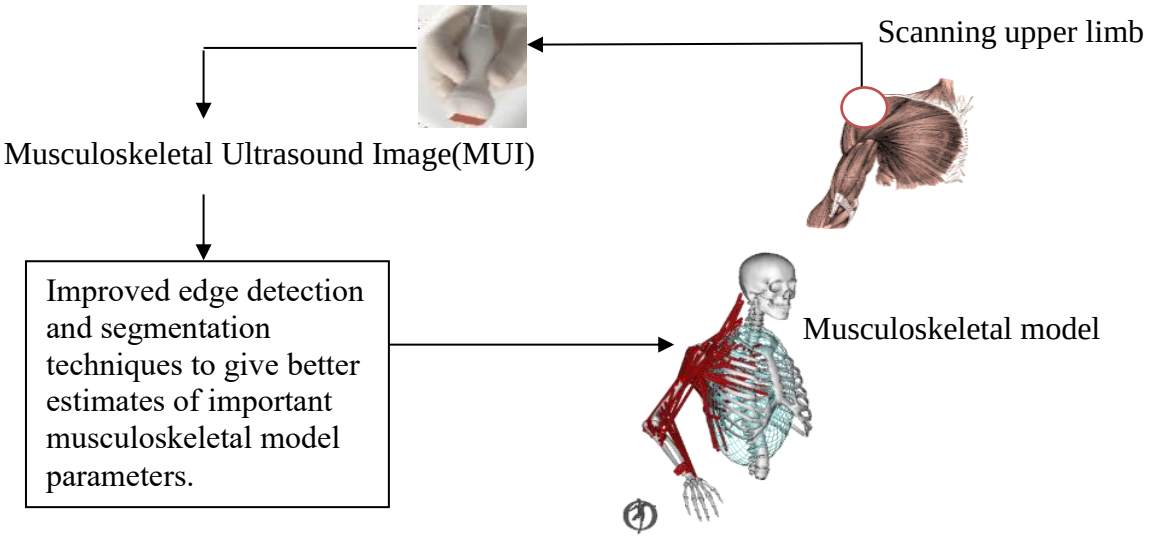

Figure (5-1) Pipeline, which explains how to get geometric parameters of musculoskeletal system then feed it to the musculoskeletal model. This pipeline includes ultrasound images, which have been recorded from healthy volunteers for image processing (image enhancement, edge detection and analysis).

In this thesis, two approaches were compared to perform edge detection of the musculoskeletal ultrasound image. Convolutional Neural Network (CNN) was recruited as a first approach, while a new fuzzy inference technique was developed and applied as a second one to achieve this purpose. Fuzzy inference technique has the potential to represent complex texture patterns in musculoskeletal ultrasound images. Furthermore, it is possible to train CNN on this kind of images.

5.1 Part 1: Using Convolutional Neural Network for Edge Detection in Musculoskeletal Ultrasound Images.

5.1.1 Introduction

Convolutional Neural Network (CNN) is one member of the Deep Learning Neural Network (DLNN) family, where DLNN is a subset of artificial neural networks. The core form of CNN is driven by a biological process at the visual cortex. CNN is constructed from different types of layers (input layer, output layer and multiple hidden layers) and each hidden layer includes the following layers: convolutional layers and pooling layers. A fully connected classification layer is output layer (Krizhevsky & Hinton, 2012). CNNs have been used in different types of biomedical imaging applications such as pixel classification as a membrane or not in electron microscopy biopsy images by Ciresan (Ciresan et al., 2012). Ciresan's work made extensive use of Graphics Processing Units (GPUs) in the training of their CNNs as GPU has a significant role in the acceleration of deep neural network training (Ciresan et al., 2013). Next, the scenario of pixel classification witnessed another turning point when it was used in biomedical image processing applications. For example, detection of mitosis in breast cancer images (Wang et al., 2014), recognition of bone tissue in the x-ray image from other tissue (Cernazanu-glavan, & Holban, 2013) and differentiation of blood vessels from its background (Melinscak et al., 2015).

Edge detection of MUI is not a trivial task due to the presence of the speckle noise, complex image texture and low image contrast. There is little doubt that despeckling ultrasound images would enhance the performance of image classifiers such as CNNs. However, in this study, it was used to assess how the noise toleration properties of CNNs can cope with this noise. In this work, CNN was applied to investigate its ability to classify whether MUI pixels

are an edge or non-edge pixel of muscles. Two different types of ground truth images are involved in the development of the CNN. One ground truth set was drawn by an expert and the other came from a commonly used automatic method of the edge detection (Canny operator). A comparison between the results was done to demonstrate the differences in CNN performance among the two cases. Additionally, CNN tolerance of low image contrast and speckle noise effect was also evaluated in this part of the chapter. So, there was no application of speckle noise reduction as a pre-processing step before CNN implementation.

5.1.2 Methods

This section is organised as follows: data preparation; CNN configuration, CNN training details; visualization of output images from training and testing processes. A quantitative assessment using the training and testing data; and further final validation with additional MUI that was not part of the training/testing process.

5.1.2.1 Dataset preparation

The details of the collection of data is found in the chapter 3, section 3.3.1. The image dimensions were initially (550x1024) pixels, but following simple cropping of the background, the dimensions became (178x783) pixels. Four sample images were collected, one of the four (sample 1) was used for CNN training and testing. While the rest of the ultrasound image samples (sample 2, sample 3 and sample 4) have been used in the final validation. Figures (5-2)*a*, (5-2)*b*, (5-2)*c* and (5-2)*d* show for sample 1: the original ultrasound image, the result of applying an automatic Canny edge-detector to sample1 to provide a Canny Ground Truth (CGT) image. A human expert-derived set of edges to be used as the Expert Ground Truth (EGT) image and manually segmented version of the EGT to more clearly delineate the interesting muscle groups, respectively. Using separate CNNs,

the same input image (sample1) was trained and tested on two different ground truth images as the target in each case.

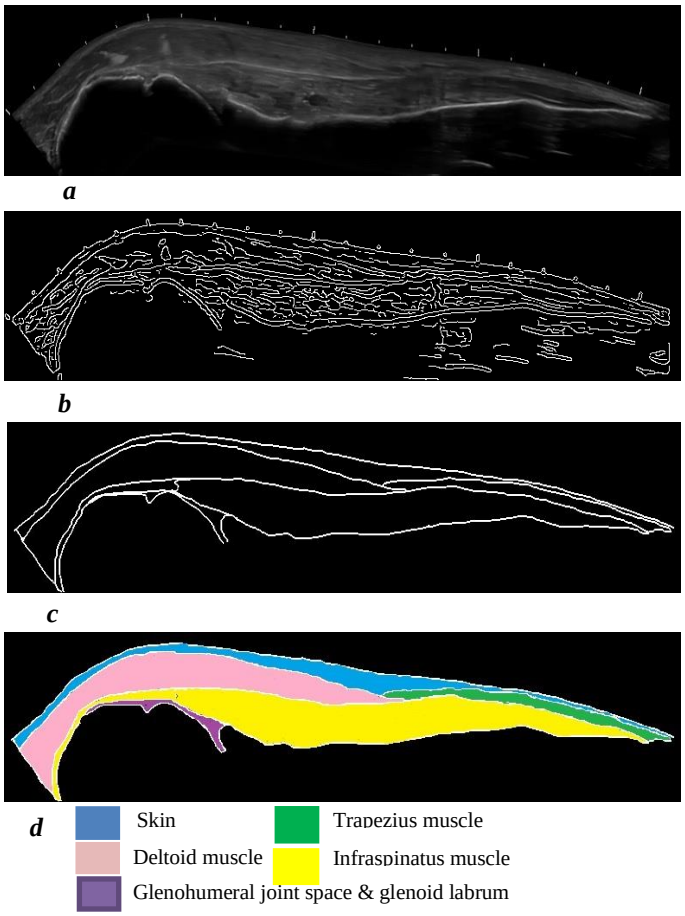

Figure (5-2) Input image of sample1 is illustrated in figure (*a*), while figure(*b*) shows CGT of sample1, it was extracted by using Matlab 8.6. Figure(*c)* shows EGT image, drawn by expert anatomist and figure (*d*) illustrates labeling of figure (*c*). by expert.

Initially, each pixel in the original image in the figure (5-2)*a* is labelled as edge pixel or non-edge pixel based on ground truth image and its x, y-coordinates are saved as well. The next step is making a random selection of the labelled pixels where it is possible to track any pixel in the training and testing. In our work, 6000 and 10000 pixels have been selected randomly as edge and non-edge pixels respectively, so that the total pixels involved are 16000. Training and testing datasets were chosen to have the same number of pixels (8000 pixels),

and 8000 pixels of training data are disjoint from the testing pixels, so there is no overlap between the training and testing data, see Figure (5-3).

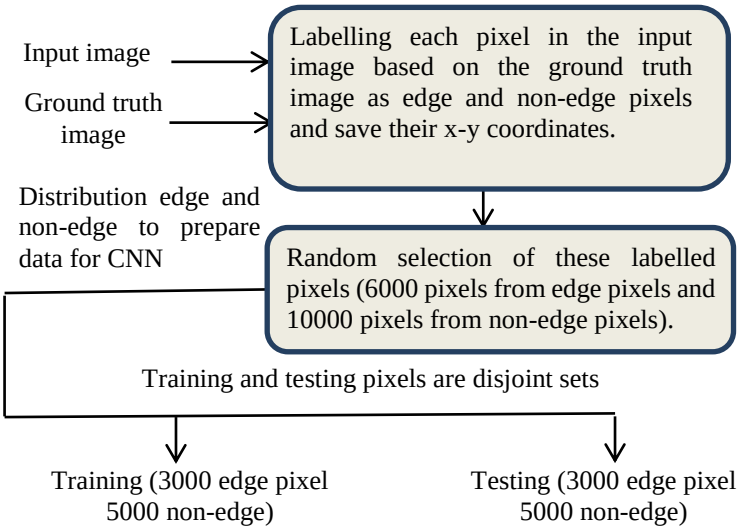

Figure (5-3) process of data preparation for training and testing. This process depends on labelling input pixels, a random selection of pixels. We can track any pixel, which has been selected based on its saved x-y coordinates and distribute unique pixels between training and testing equally.

5.1.2.2 CNN configuration

Three main types of layers build the solid foundation of CNN processing. These layers are Convolutional Layers (CL), Max-pooling Layers (ML) and a final Fully Connected Layer (FCL). Convolutional layer performs linear operation to extract features using set of filters, where it can slide a kernel across input dimensions and the weights of the kernel are shared in every slide of this layer. While, the effect of the pooling layer is to reduce the spatial size of data representation. The reason is to extract a set of features that are compressed/summarised versions of the information from the previous layer. In this way the CNN extracts higher and higher-level features from the data in the original image. The last layer if fully connected layer, works as an ordinary neural network: detecting the last version

of features and combining them together to get the final output. Some critical problem-specific CNN parameters that must be carefully chosen include kernel size to avoid pixel fractions, and the overall number and size of the convolutional and max-pooling layers. Each of these has a powerful impact on the quality of the final outputs. So, several kernel sizes and numbers of feature maps in successive CNN layers have been evaluated for overall classification accuracy, see below. The FCL layer is a standard neural network classification layer (Özkan, 2015); the type of activation function used is a sigmoid function. It can be bounded within the range [minimum, maximum], so allows simple thresholding to get the final output classifications (Doorn, 2014).

The configuration of CNN depends on the window size and kernel size. The best value of window size will be selected based on the evaluation of the assessment metric, which gives a highest score. In the case of classification, a pixel whether it is an edge or not , the dimension of the window should be odd. Furthermore, the selection of the kernel size is necessary to decide the depth of CNN layers.

5.1.2.3 Training

All this work was implemented in MATLAB 8.6. The training of each CNN used the input image from the figure (5-2)*a*, but with separate ground truth images from the figure (5-2)*b* and Figure (5-2)*c*. The training was done on a computer with an Intel Core i5 processor (2.5 GHz), 6GB RAM and without GPU support. The training dataset preparation will vary slightly according to the different window size and the CNN configurations. One of the important aspects of CNN training is weights sharing and how max-pooling layers can reduce the problem to higher and higher levels of important features from the input image. However, the time required to train CNN's increases when increasing the window size and

number of training epochs. CNN was trained and evaluated on range of different epochs (1, 25, 50, 100, and 150) and different window sizes.

5.1.2.4 Visualizing output images from training and testing

The total number of pixels in the training and testing datasets is 16000. These pixels are randomly distributed concerning their x-y coordinates in the input image. The output image after passing the training and testing data through a CNN can be created from the x-y coordinates for each pixel, as described in figure (5-4) below:

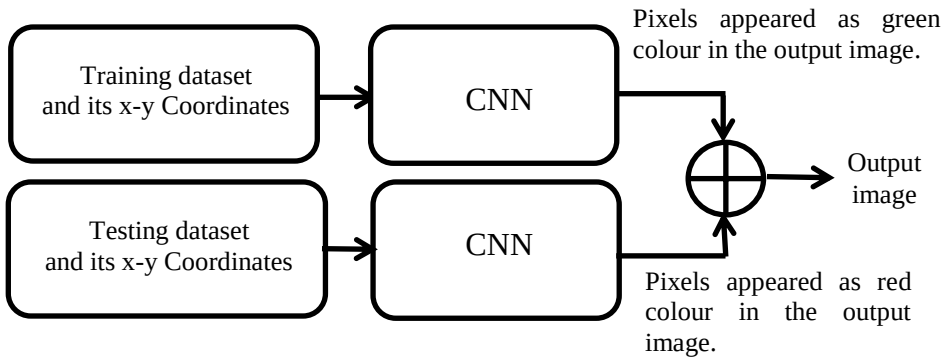

Figure (5-4), output image from training and testing dataset.

5.1.2.5 Performance measure

In addition to qualitatively observing the content of the output images derived using the process in the figure (5-4), it is possible to evaluate quantitatively the quality of each output image. Matthews Correlation Coefficient (MCC) was selected as a metric when tuning window size for the best CNN configuration. MCC is a useful metric for unbalanced classification datasets. The MCC takes values [-1, +1], where: 1 indicates the absolute correlation between output image and ground truth image; when MCC is 0 that means no

correlation and; when there is a perfect inverse correlation the MCC is -1. MCC can be calculated using the following equation:

$$MCC = \frac{Tp * Tn - Fp * Fn}{\sqrt{(Tp + Fp)(Tp + Fn)(Tn + Fp)(Tn + Fn)}} \quad (27)$$

where Tp is True positive, Tn is True negative, Fp is False positive, and Fn is False negative. Tp defines appropriately detected edge pixels, Fp value gives the number of incorrect edge pixels, Tn pixels is the complement to the Tp and Fn is missing edge pixels. Each of these terms can be calculated by following equations: -

$$\mathrm{Tp} = |\mathrm{I_{out}} \cap \mathrm{I_{GT}}| \quad (28a)$$

$$\mathrm{Fp} = |\mathrm{I_{out}} \cap -\mathrm{I_{GT}}| \quad (28b)$$

$$\mathrm{Tn} = |-\mathrm{I_{out}} \cap -\mathrm{I_{GT}}| \quad (28c)$$

$$\mathrm{Fn} = |-\mathrm{I_{out}} \cap \mathrm{I_{GT}}| \quad (28d)$$

where I_{out} is output binary image, which has an edge or not-edge pixels, I_{GT} is ground truth image, - I_{out} is the complement of I_{out} and - I_{GT} is the complement of I_{GT}. (Özkan, 2015; Matthews, 1975). Other valuable quantitative classification metrics are Specificity, Sensitivity and Accuracy (Lopez-Molina, 2013). Sensitivity is the ability of the identification of the edge pixel correctly while, specificity is the ability to identify incorrect edge pixels, see equations (29) and (30) respectively. The accuracy of applying edge detection method is its ability to differentiate the edge pixels from non-edge pixels correctly. To evaluate the accuracy of edge detection image, we need to calculate the proportion of true positive and true negative in all evaluated cases as shown in equation (31).

$$\mathrm{Sensitivity} = \frac{\mathrm{Tp}}{\mathrm{Tp+Fn}} \quad (29)$$

$$\mathrm{Specificity} = \frac{\mathrm{Tn}}{\mathrm{Tn+Fp}} \quad (30)$$

$$\text{Accuracy} = \frac{\text{Tp+Tn}}{\text{Tp+Fp+Tn+Fn}} \quad (31)$$

5.1.2.6 Final Validation using previously unseen MUI

For each of the separate Canny ground truth images and expert ground truth image trained/tested CNNs use three samples of previously unseen ultrasound images for validation. Each CNN was evaluated using Canny ground truth image data expert ground truth image data respectively.

5.1.3 Experiments and results

Our work has been inspired by the recent work of Ciresan et al. where CNNs were used to analyse images obtained from electron microscopy (Ciresan et al., 2012), but our work uses another biomedical image source: Musculoskeletal Ultrasound Images. In this work, datasets have been prepared for training a CNN and testing, see figure (5-3). We used different input window sizes from 5 to 95 pixels, different CNN configurations and a suitable epoch number to illustrate which one of these properties supports CNN to get the highest level of performance.

The selection of the best window size in this work for both ground truth images used the maximum value of MCC as the optimisation criterion. In the case of using CGT image, the best window size was 13, while the best window size was 27 when training CNN on EGT image, see figure (5-5) below. The EGT image described ultrasound image edges relatively simply, while CGT discovered very complicated and potentially spurious edges. So, it did not expect to get the agreement in the optimisation of the window size for the two CNNs.

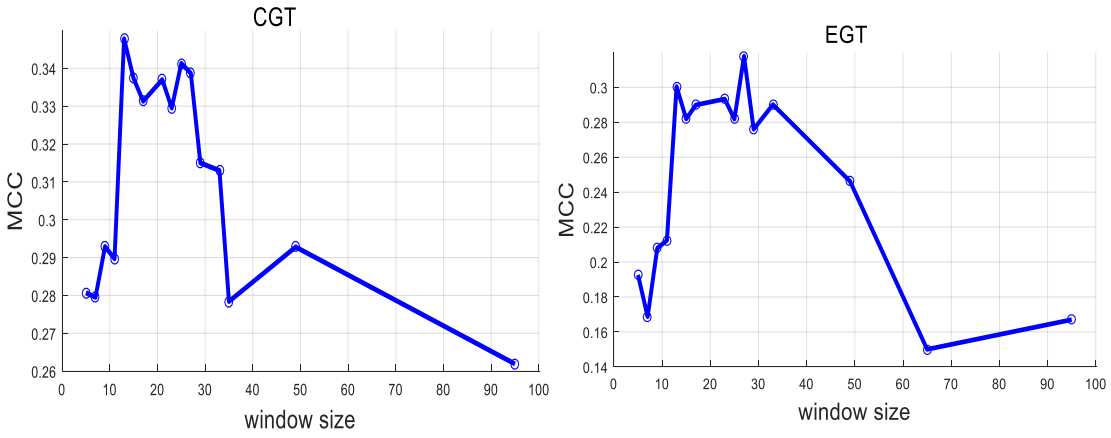

Figure (5-5), the left-hand side of this figure shows optimization of window size for CGT image, while the right hand side illustrates optimization of window size for EGT image.

Regarding CNN configurations, kernel sizes were selected based on selected window size for both different ground truth images and in the same time avoid any fraction of kernel size. Table (5-1) and table (5-2) illustrate CNN configurations used for both above optimal window sizes.

Table (5-1) CNN configuration (13x13) in the case of using CGT, window size =13x13.

Layer	Type	FM &Neuron	Kernel size
1	Input layer	1 Map of 13x13 neurons	-
2	Convolutional	6 Maps of 10x10 neurons	4x4
3	Max-pooling	6 Maps of 5x5 neurons	2x2
4	Convolutional	12 Maps of 2x2 neurons	4x4
5	Max-pooling	12 Maps of 1x1 neurons	2x2
6	Fully connected	1 neuron	-

Table (5-2) CNN configuration (27x27) in the case of using CGT, window size =27x27.

Layer	Type	FM &Neuron	Kernel size
1	Input layer	1 Map of 27x27 neurons	-
2	Convolutional	6 Maps of 24x24 neurons	4x4
3	Max-pooling	6 Maps of 12x12 neurons	2x2
4	Convolutional	12 Maps of 8x8 neurons	5x5
5	Max-pooling	12 Maps of 4x4 neurons	2x2
6	Convolutional	12 Maps of 2x2 neurons	3x3
7	Max-pooling	12 Maps of 1x1 neurons	2x2
8	Fully connected	1 neuron	-

After identification of the optimal CNN properties (window size, CNN configuration) and training with these properties, CNN is ready for testing. It is possible to visualise the output image of CNN from the training and testing processes combined, in the case of using EGT

image as the example. Figure (5-6) illustrates an output image synthesised from training and testing data shown in different colours.

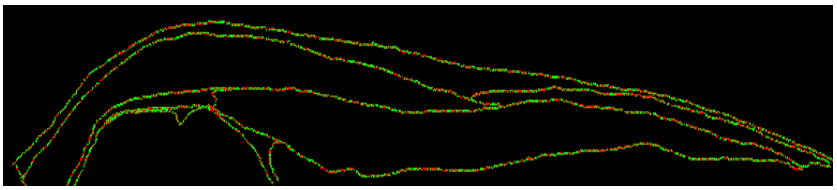

Figure (5-6) Composite output image produced using the output of the trained and tested CNN, showing the training pixels (in green) and the testing pixels (in red) using the data derived from the EGT image.

Of course, in figure (5-6) one can see an incomplete image due to the selection of just 8000 pixels for training and 8000 pixels for testing, so not all pixels from the original input image are shown in the figure (5-2)*a*. The evaluation of the two CNN approaches (one using Canny ground truth image and the other using expert ground truth image) can be succinctly described in the form of two experiments: Experiment 1 and Experiment 2.

5.1.3.1 Experiment 1

In Experiment 1, Canny ground truth data was obtained by applying a Canny edge-detection operator on the raw input ultrasound image (Canny, 1986). The Canny operator is a traditional method for image edge detection and is automatic since it does not rely on the opinion of an expert in the analysis of MUI. However, it is not expected to produce the ideal set of edges for our purposes; it is susceptible to noise and can create some spurious edges: sometimes extra edges and sometimes missing some important edges. The main purpose of this experiment is to investigate the sensitivity of CNN among the image of Canny operator, which is considered in this experiment as ground truth image. Figure (5-7) represents the output image, which is obtained from the Canny ground truth image -trained CNN when (window size=13, epochs =100).

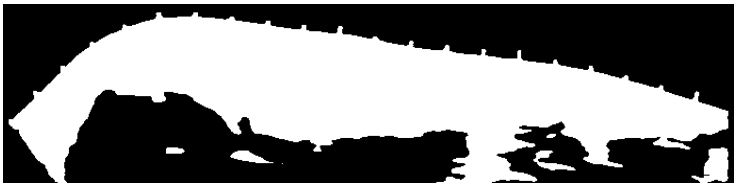

Figure (5-7) Output image derived by the Canny ground truth image -CNN using sample1 as the input image.

The CGT-CNN output image above shows us just a full foreground object and its background, but it is impossible to discriminate any boundaries that separate the three most important muscles. The Tp, Fp, Tn and Fn versions of this output image are shown in figure (5-8). It is clear in the Fp image; there are a lot of error pixels beside real edge pixels, so it is easy to see why all three muscles seem as one full object in figure (5-7).

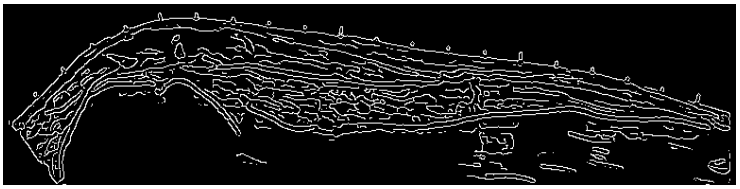

Tp

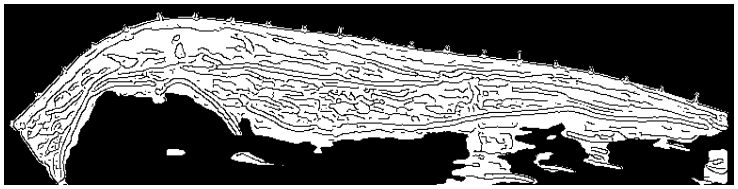

Fp

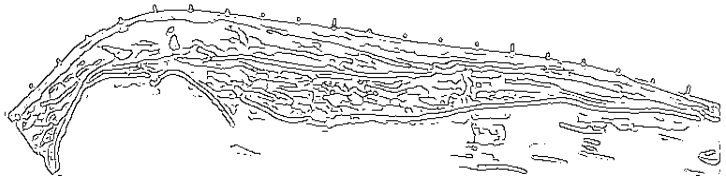

Tn

Fn

Figure (5-8), from top to bottom, Tp, Fp, Tn and Fn of input MUI (sample1).

Experiment 1 Validation: -

Three unseen MUI images are involved in the validation of this experiment. Figures (5-9) and (5-10) below, show the input image (i.e. samples 2, 3 and 4), the CGT for each of the input images and the CGT-CNN derived output images respectively.

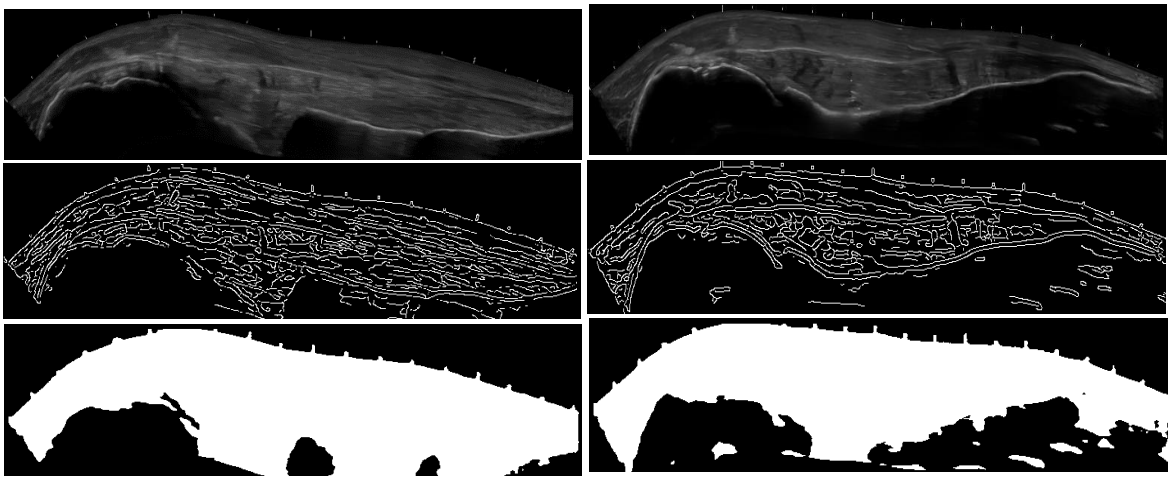

Sample 2 Sample 3

Figure (5-9), the left column from top to bottom illustrates input ultrasound image (sample2), CGT and output image, while the right column shows, input ultrasound image (sample3), CGT and output image.

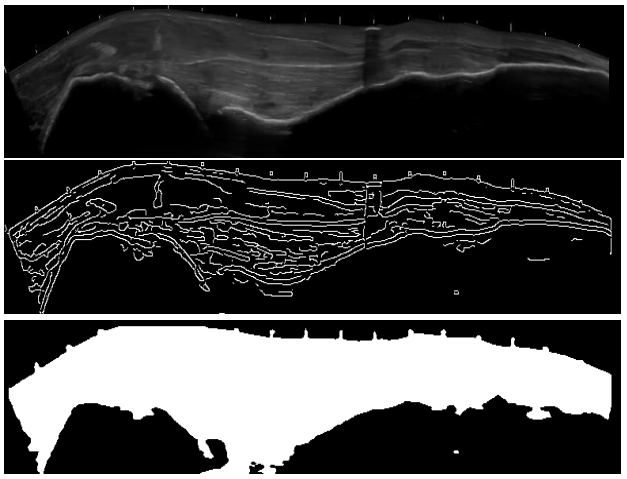

Figure (5-10), from top to bottom, input ultrasound image (sample4), CGT and output image.

5.1.3.2 Experiment 2

The EGT images used for this experiment reflect the expertise of a person who can match anatomical structures with ultrasound imaging. Using the panoramic ultrasound images, it is possible to see whole muscles, bones, and tendons. However, using the panoramic technique drawing for all of the necessary ground truth images is costly. Furthermore, when gathering EGT data, it is difficult to trace the important information of the succession of images and at the same time maintain the necessary alignment between the ground truth image and the

original MUI image. However, training an EGT-CNN using this EGT image gives us a clearer set of edges with which to reliably differentiate each of the three muscles. Additionally, if we can train the EGT-CNN on a relatively modest number of images, and have it identified the outlines of muscles with good accuracy; the potential benefits are huge. Figure (5-11) shows the EGT-CNN output image derived using sample 1, see figure (5-2)*a* when window size=27 and epochs =100.

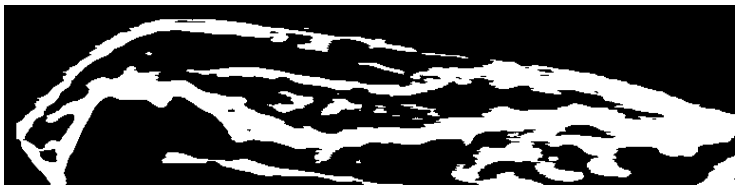

Figure (5-11) Output image derived by the EGT-CNN using sample1 as the input image.

To contrast, the experiment 1, figure (5-12) provides us with the idea about Tp, Fp, Tn and Fn of the output image in figure (5-11), Fp image below tells us there is a statistically significant difference between Fp of this image and Fp in figure (5-8). That leads to the clear interpretation of image details in the case of training CNN by using EGT image.

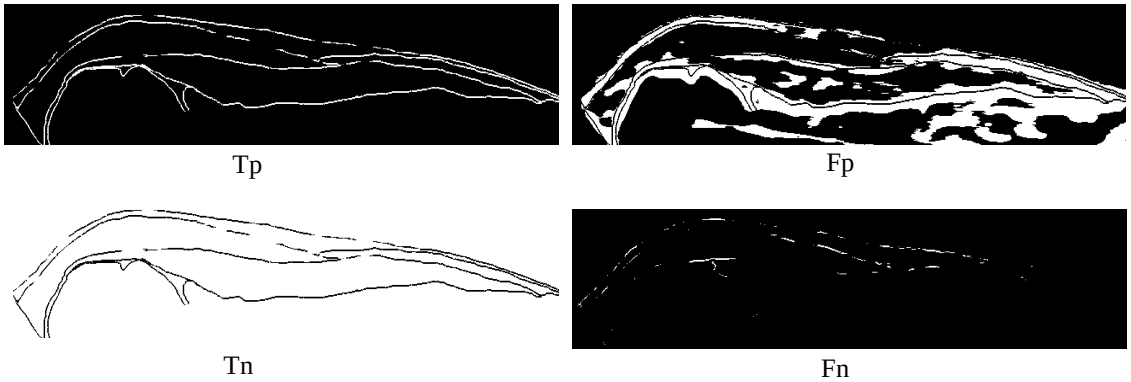

Figure (5-12), from top to bottom, Tp, Fp, Tn and Fn of input MUI (sample1).

Experiment 2 Validation

Again, three previously unseen MUI images are involved in this validation. Figures (5-13) and (5-14) include input images of the samples (2, 3, and 4), the equivalent EGT images and the relevant EGT-CNN derived output images, respectively.

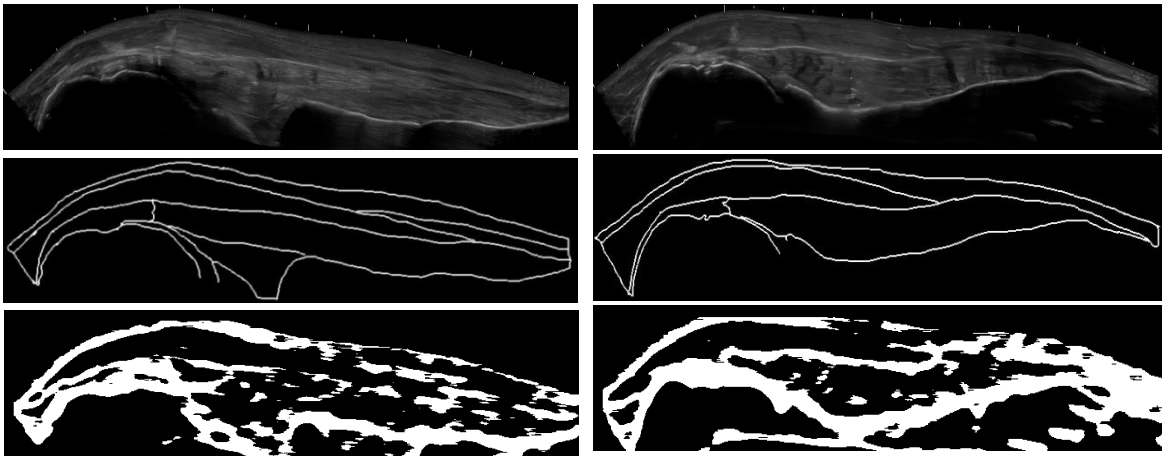

Sample2 Sample3

Figure (5-13), the left column from top to bottom, illustrates input ultrasound image (sample2), EGT and output image, while the right column shows, input ultrasound image (sample3), EGT and output ultrasound image.

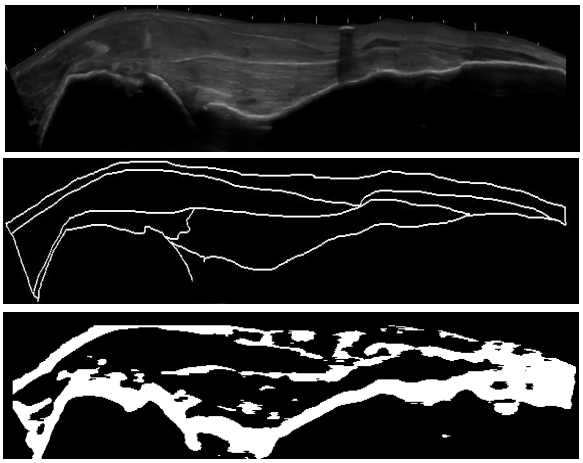

Figure (5-14), from top to bottom, input ultrasound image (sample4), EGT and output ultrasound image.

A quantitative assessment of three previously unseen validation MUI samples obtained from each of the two experiments (including data for the first MUI sample) is shown in table (5-3), below.

Table (5-3) Quantitative assessment of output of MUI).

Experiment1 (CGT image)			
Samples	Accuracy	Specificity	Sensitivity
Sample1	0.72	0.706	0.976
Sample2	0.67	0.65	0.99
Sample3	0.69	0.68	0.97
Sample4	0.69	0.67	0.97
Mean	0.69	0.676	0.976
Standard deviation	0.0179	0.0202	0.0082
Experiment2 (EGT image)			
Sample1	0.80	0.796	0.896
Sample2	0.815	0.823	0.638
Sample3	0.786	0.787	0.766
Sample4	0.812	0.817	0.694
Mean	0.803	0.81	0.75
Standard deviation	0.0132	0.0170	0.1114

5.1.4 Discussion

In this work, CNN was applied on the MUI to identify pixels of the musculoskeletal ultrasound image and to see whether it is edge or not. The performance of CNN was illustrated on two types of ground truth images through two experiments. The first one used a traditional method (Canny operator), and it is considered in this work as ground truth image. The second ground truth image was drawn by an expert. In addition, this work has not used any kind of pre-processing like foveation (Ciresan et al., 2012), contrast enhancement or any active denoising to reduce the effects of speckle noise (Gupta et al., 2014). If carried out, this kind of processing is likely to boost CNN performance, but at the expense of extra pre-processing computation.

From the figures above, (from Experiment 2), one can observe the boundaries of three muscles in the Expert Ground Truth (EGT) image. Whereas, in Experiment 1 the Canny Ground Truth (CGT) acquired images make it impossible to see muscle boundaries and instead just a solid foreground object can be separated from the background pixels. This means that qualitatively the output images of CNN by EGT allow better identification of individual muscle than CGT-CNN output images.

In addition, table (5-3) gives a quantitative assessment of musculoskeletal image samples for the output from Experiment 1 and Experiment 2. In Experiment 1, our method achieved a lower accuracy value of mean = 0.69, while in Experiment 2 the mean = 0.8: showing that the EGT-CNN is more able to identify muscle boundaries. Table (5-3) also shows a noticeable difference in specificity values between the two experiments. The specificity in Experiment 2 is higher than in Experiment 1 because the Experiment 2 output images deliver fewer spurious edge pixels, see figure (5-8) and figure (5-12) as the example. This indicates that the performance of CNNs trained on EGT image data outperforms CNNs trained on CGT images.

According to equation (29), the number of Fn pixels has a significant impact on the value of sensitivity. In Experiment 1, the average sensitivity value is high because Fn is perversely very low: and this is due to the output image in this experiment having all of the edge pixels detected in the CGT image, making the resulting sensitivity value approximately equal to Tp/Tp. However, overall better-quality pixel classification is achieved in Experiment 2. Experiment 2's output images give us an acceptable way to determine the muscle boundary details of the input. Whereas, the output images of Experiment 1 only allow us to separate foreground objects from the background. The standard deviation of quantitative values in the table (5-3) shows us there is little difference between values of all samples.

The results are promising, but it needs some refinements to raise the CNN performance. Some of these refinements are to increase the size of the CNN training datasets to get better results and using GPU to help accelerate training and reduce implementation time.

5.1.5 Conclusions

In this part of the thesis, a very promising result was achieved when CNN was applied on MUI as it is the first use of state-of-the-art CNNs that focused on MUI edge detection. Moreover, CNN is likely to be a scalable solution, which improves the usefulness of important approaches in MUI such as the panoramic technique.

CNN has the potential to do pixel-based edge-detection on MUI in ways that are akin to a human anatomist with expertise in the analysis of this kind of image.

5.2 Part 2: Using fuzzy edge detection image technique in Musculoskeletal Ultrasound Images.

5.2.1 Introduction

In this thesis and in the first part of this chapter, a promising CNN experiment that is involved in classifying whether a pixel is an edge or not was presented. However, a successful CNN technique requires an extensive training and large training dataset to obtain a satisfactory edge detection output image. In this work, the CNN experiment has a small training dataset because the collection of a large dataset of MUI requires a long time to gather and needs an expert to recognize a complex features pattern of the images. Furthermore, the details of many edges in a resultant image of the CNN technique were highly interconnected. So, CNN technique allows to visualise an image's edges of the muscle boundaries, tendon, bone and other details altogether in one image. However, when the aim is to measure muscle borders alone automatically, then it is desirable to exclude other MUI details to minimise artifacts. This manoeuvre would help to optimise of edge detection for the structures of interest and reject those that are not needed.

Therefore, Fuzzy Edge Detection Method (FEDM) was developed in the second part of this chapter as a novel method to accomplish edge detection, which is based mainly on a fuzzy technique. It is conducted through fuzzification plus optimization of the fuzzy membership functions to achieve the best output, construction of fuzzy rules for edge detection in the fuzzy domain and defuzzification. Selection of parameters for the membership functions depends on the analysis of the standard deviation curve of a set of thresholded images as this curve depicts the variation of grey level intensities. These membership functions show

different levels of information. Furthermore, fuzzy rules reflect the knowledge of representation and detection of the enhanced image's edges.

In using fuzzy edge detection method (FEDM), it is possible to exclude the unnecessary information such as texture or speckle information and keep the most appropriate edge detection information. FEDM is relatively easy, completely automatic and its implementation is not time-consuming. The advantage of this technique is a robust edge detection method, which gives a clear description of the object's properties inside the MUI, without needing to collect too much data from MUI for training CNN as an example. In addition, there is no requirement for a large training dataset and it is not as time-consuming as CNN technique.

5.2.2 Metrics of Edge Measurement based on Reference image

Measurement of the FEDM's performance gives evidence about the technique's effectiveness and helps in improving edge detection method to get a high level of accuracy when describing geometric parameters of the object. The edge map can be assessed using subjective and objective evaluations. Subjective evaluation can be carried out based on human opinions and rating scales such as Mean Opinion Score (MOS) (Huynh-Thu et al, 2010), while objective evaluation is determined based on comparing the resultant edge image to a reference image. Often, a reference-based, objective measurement is recommended because MOS might be biased in the visual interpretation and it is difficult to measure the quality of edge performance without using a reference image (Panetta et al, 2016). Reference image reflects the expertise of the expert in demonstrating the most important details in the image to create this image. Different statistical methods have been used in reference objective assessment; for example, F-measure and Matthews Correlation Coefficient. These

methods include extraction of True positive (Tp), False positive (Fp), True negative (Tn) and False negative (Fn) by matching pixels of detected edge image and reference image (Lopez-Molina et al, 2013). Although an expert has the experience to trace the important details of the input image, it is not possible to say that reference image is faultless in assigning the precise location of the pixel; because the expert will draw it manually. Therefore, comparison between the detected image and ground truth image based on a pixel-by-pixel assessment may not give us an accurate evaluation. However, if the match between edge maps of detected and ground truth images is tested by analysis of higher-level features dependent on accurate assessment of the edge, it might avoid the pitfalls of a pixel by pixel comparison. Analysis of edge characteristics might include evaluations such as distance between actual edge and ideal edge pixel, thick edge occurrence and edge pixel presence. The first standard method, which was used in this matching, was Pratt's Figure of Merit (FOM) method; it is shown in equation (32).

$$FOM_{Pratt} = \frac{1}{max\{N_g, N_a\}} \sum_{i=1}^{N_a} \frac{1}{1 + \propto d^2} \tag{32}$$

where N_g is number of edge pixel in ground truth image, N_a is number of actual edge pixel, d is distance between actual edge pixel and the nearest ideal edge pixel and α equals 1/9 (at this value, a reasonable edge position is detected, suggested by Pratt, (1978). Moreover, the improved version of this method was achieved by Pinho for giving more effective accounting of false edges, as shown in equation (33).

$$Pinho = \left[\frac{1}{N_g} \sum_{k=0}^{N_g} \frac{1}{1 + \propto d^2}\right] \left[\frac{1}{1 + \beta \frac{N_{FP}}{N_g}}\right] \tag{33}$$

where N_{FP} is number of false positive pixels and the value of β is 1, but in the case of N_{FP}=N_g, the value of this parameter will be 0.5 (Pinho and Almeida, 1995). Recently, Reference-

Based Edge Measure (RBEM) has been introduced and applied to simple geometric shape image and natural images such as animal's image in the jungle (Panetta et al, 2016). In this metric, four edge characteristics are fused together: evaluation of edge connectivity, thick edge occurrence, edge localization and edge corner presence, to get an improved level of the quality assessment. This method demonstrated a high agreement with subjective assessment, which has been estimated by collecting opinions of experts (MOS). Equation (34) presents the main components of RBEM.

$$RBEM = \psi_L(1 - D_L) + \psi_{CO}(1 - D_{CO}) + \psi_{TH}(1 - D_{TH}) + \psi_S(1 - D_S) \quad (34)$$

where D_L is measurement of the edge pixels localization, D_{CO} is to measure edge corner presence, D_{TH} demonstrates the thick edge occurrence measurement and D_S is measurement of isolated pixels in output edge detection image. Ψ_L, Ψ_{CO}, Ψ_{TH} and Ψ_S are parameters for edge pixel, edge corner, thickness of edge and isolated pixels respectively. The values of these parameters used in the natural images were Ψ_L =0.63, Ψ_{CO} = -0.02, Ψ_{TH} =1.35 and Ψ_S =-1.28. All details of determination of D_L, D_{CO}, D_{TH} and D_S are as suggested in (Nercessian et al, 2009; Panetta et al, 2016). The results reported in Chapter 5 part 1 were published in early of 2016, when I used MCC for analysis. The RBEM metric was adopted for my research in late of 2016.

5.2.3 Fuzzy Edge Detection Method (FEDM)

This technique is based on fuzzy inference system and composed of the following steps: recruiting three membership functions are defined by a selection of the appropriate parameters in the first step. Selection parameters of the membership functions depends on the analysis of the standard deviation curve of input image. The second step is the construction of fuzzy rules that reflect acknowledge to represent the probabilities of the edge

pixels at a 3x3 window. The last step is defuzzification using Takagi and Sugeno method to obtain the output MUI (edge detection image), see figure (5-15) below.

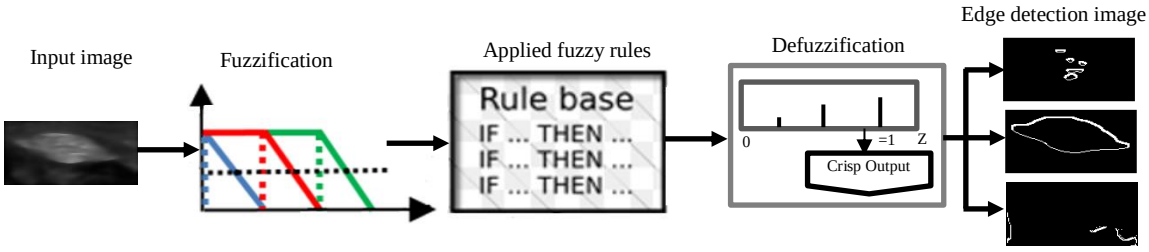

Figure (5-15) Pipeline of FEDM structure.

5.2.3.1 Fuzzification

The purpose of fuzzification is to map the grey level intensities of the image from the spatial domain to the fuzzy domain. Fuzzification can be done by choosing a suitable membership function (Tizhoosh et al, 1997). The two most important aspects of the membership function are its form and the parameters that describe the behaviour of these functions. In this work, three membership functions were established for three different levels of edge detection information. Parameters of these functions were selected according to the analysis of image properties. Assuming (*i, j*) are the spatial coordinates of each pixel in the input image *I* of size *N*x*M*, *gmax* is the maximum grey level intensity in the input image and *gmin* is the minimum, $I(i,j) \in [gmin, gmax]$. The intensity of the input image (spatial domain) is mapped to the interval [0,1] (fuzzy domain), equation (35) gives us a general aspect of these functions.

$$\mu_{a,Cp_{a-1},Cp_a}(i,j) = mapping\big(I(i,j)\big) \tag{35}$$

where multi membership functions are $\mu_{a,Cp_{a-1},Cp_a}(i,j) \in [0,1]$, a=1,3, and (Cp_{a-1},Cp_a) are parameters of $\mu_a(i,j)$. Figure (5-16), shows the form of the three membership functions in

different colors; for three different levels of edge detection information. High membership values in all three different levels are greater or equal 0.5, while low values are under 0.5.

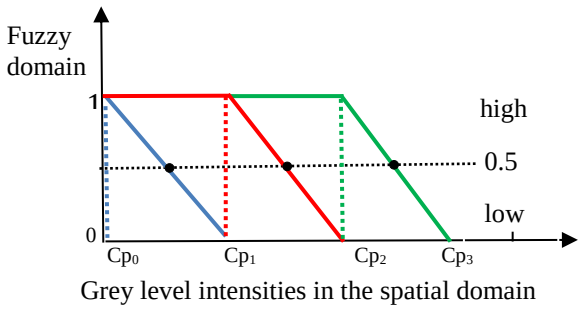

Figure (5-16) illustrates three membership functions ($\mu_1(i,j)$, $\mu_2(i,j)$ and $\mu_3(i,j)$) in different colors, blue color for first membership function in the case of level 1, red color for level 2 and green color for representation membership function of level 3, where, (Cp_0, Cp_1, Cp_2, and Cp_3) are parameters of these membership functions.

The important question is, how can a good set of membership functions be constructed for musculoskeletal ultrasound image domain using parameters (Cp_0, Cp_1, Cp_2, and Cp_3)? In this work, a new method for the selection of these parameters was developed. This method relies on an analysis of the standard deviation of grey level intensities instead of looking at the grey level intensities themselves, or analysis of the shape of the image histogram. Most medical images, particularly musculoskeletal US images, have heterogeneous regions of grey level intensities; this leads to difficulties in interpreting the shape of the histogram due to its many peaks and valleys (Sonka et al, 1993). Standard Deviation (SD) of grey level intensity provides a simple summary measure of the amount of data variability in the image. Before the standard deviation of the intensities is evaluated the original image is thresholded several times across a range of thresholds using equation (36):

$$B_h(i,j) = \begin{cases} I(i,j) & if\ \ I(i,j) \geq T_h \\ 0 & else \end{cases} \qquad (36)$$

where $I(i,j)$ is the original input image with dimension i and j, h=1,2,3, h denotes to the cut-off point and n to the number of cut-off points. T_h is the threshold used to generate output image $B_h(i,j)$ and T_h takes integer values over the range [*gmin*, *gmax*]. Based on the SD values, which are calculated for each $B_h(i,j)$ images an SD curve can be plotted against cut-off intensity. The SD curve gives us an indication of the variation of grey level intensities. If the cut-off point = *gmin*, this means the SD will be calculated for the original image, and if the image has low SD value, there are fewer pixels having different grey level intensities as compared to high level of SD, in which there is a greater variety of image grey level intensities. Furthermore, the complexity and amount of computation will be increased as the size of the i and j increase. A novel aspect of our proposed fuzzy edge detection method is to exploit the characteristic shape of this SD curve for thresholded musculoskeletal US images which rises to SDmax before decreasing again, see figure (5-17) below.

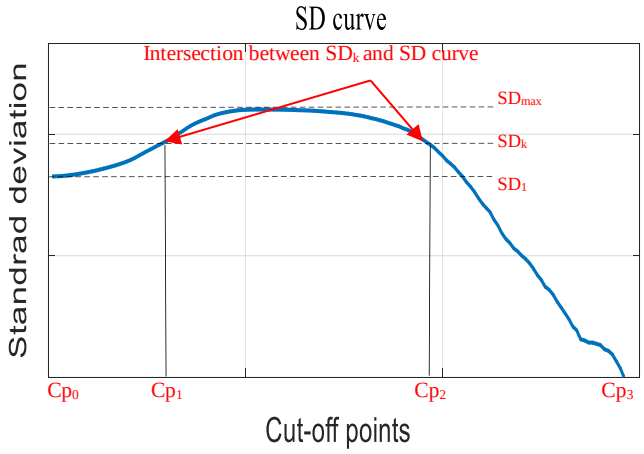

Figure (5-17) illustrated plot of SD curve which is calculated from a set of SD values. In this curve the value of SD_k is calculated at m_k =0.5 as example.

By collecting together SD values for each thresholded image they can be used to determine four parameters of the fuzzy membership functions, as follows:

1-Extract a set of the thresholded images based on a set of cut-off points with the range [*gmin*, *gmax*] by using equation (36), to get a set of thresholded images $B_h(i,j)$, h=1,2,…n, where n is number of cut off points. For example, if *gmin* =10 and *gmax* =200, so number of cut-off points=190, the first cut-off point is 10, the second is 11 …and the last cut-off point is 200.

2-For each thresholded image $B_h(i,j)$, calculate and save the standard deviation of pixel intensities, in order to get $SD_1(B_1(i,j))$, $SD_2(B_2(i,j))$, $SD_3(B_3(i,j))$… $SD_n(B_n(i,j))$.

3-Assign (SD_1) as the value of SD at initial state (at first cut-off point) and find SD_{max}, which represents the maximum value of the SD set.

4-Calculate SD_k using equation (37): $SD_k = m_k(SD_{max} - SD_1) + SD_1$ (37)

where m_k is control parameter, k =1, 2, ...10 and m_1=0.1, m_2=0.2… m_{10}=1.

5-This step consists of three parts as follows: -

a. Calculate the difference between SD_k and the array of SD values and save the result.

b. Detect the minimum differences which belong to cut-off points and save these cut-off points. Where, minimum difference points represent the intersection between SD_k and the SD array, as illustrated by figure (5-17).

c. Translate these cut-off points to the grey level intensities to get Cp_1 and Cp_2.

6-Add one row to a matrix recording these membership parameters (Cp_0, Cp_1, Cp_2 and Cp_3), these parameters defining fuzzy membership function in figure (5-16). Where, (Cp_1, Cp_2) are obtained from the previous step and (Cp_0, Cp_3) represents *gmin* and *gmax* respectively. The changing parameters on each row of the matrix depend on the changing the m_k value, go back to the step 4.

7-For each row of this matrix calculate $RBEM_k$ to find the best value of m_k.

where (Cp_0, Cp_1) are parameters of the fuzzy membership function of Level 1, (Cp_1, Cp_2) are parameters of the fuzzy membership function of Level 2 and (Cp_2, Cp_3) are parameters of the fuzzy membership function of Level 3.

5.2.3.2 Application of the fuzzy rules and defuzzification

As shown in figure (5-18), where C_5 is the particular pixel in $\mu_k(i,j)$ and (C_1, C_2, C_3, C_4, C_6, C_7, C_8, C_9) are neighbour pixels of the C_5 pixel. The black color in 3x3 window represent high probabilities of darkness grey level intensities, while the white color reflects high probabilities of brightness grey level intensities.

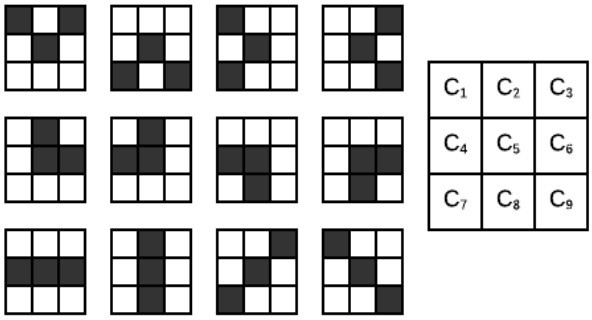

Figure (5-18) Mask configuration for detection of image's edges.

Twelve fuzzy rules were introduced to represent twelve properties of edge pixel in a 3x3 mask as are shown in the figure (5-18). If the weights of central pixel and two neighbour pixels are high degree of membership (fuzzy set is greater than or equal to 0.5) and the weights of remaining five neighbour pixels are low degree (fuzzy set is less than 0.5), then the central pixel represents an edge, see figure (5-17). All details of rules in the Appendix III, but some of rules are demonstrated as follows:

Rule 1: If (C_1, C_3, & C_5) are high & (C_2, C_4, C_6, C_7, C_8, & C_9) are low then central pixel is edge.

Rule 2: If (C_5, C_7, & C_9) are high & (C_1, C_2, C_3, C_4, C_6, & C_8) are low then central pixel is edge.

…

Rule 12: If (C_1, C_5, & C_9) are high & (C_2, C_3, C_4, C_6, C_7, & C_8) are low then central pixel is edge.

In this work, the Takagi and Sugeno method (Takagi and Sugeno, 1985) was selected to detect output edges, each rule has a crisp output, and the final output is evaluated by weighting the average of rules using equation (38):

$$Final\_output = \frac{\sum_{d=1}^{R} W_d Z_d}{\sum_{d=1}^{R} Wd} \tag{38}$$

where, W_d is rule weight (antecedent), the part of the sentence after IF in the rule and weight is determined by performing the first part of each rule, while Z_d represents output level (consequent or conclusion in the rule) and d=1…R, R is number of rules and equal 12. This method was designed to get an edge detection image with two colors (black and white) and is not time consuming. Ultimately, different levels of edge detection images were extracted. It is possible to choose the most appropriate level of information and exclude unnecessary regions to get a powerful final edge detection image. However, it is useful to additionally

remove some individual pixels or thin double layers of edges from the final edge detection image using morphological operations (Haralick and Sternberg, 1987).

5.2.4 Experiments and Results

5.2.4.1 Experiment 1

Data was collected from 25 healthy volunteers (9 females and 16 males) and from the hand region (protocol 1), all details in section 3.3.2.1. The collected images show the cross section of flexor pollicis longus tendon and 25 ground truth images for these samples were drawn by an expert, who concentrated on identifying the boundaries of the cross section of the flexor pollicis longus tendon in the ground truth images.

Pre-processing steps (denoising):

In this section, an anisotropic diffusion filter was applied to 25 samples of the healthy image to reduce speckle noise. The details of the image in sample 1 elucidate all processing steps for one example image. The first step is reducing speckle noise of the musculoskeletal ultrasound image using an anisotropic diffusion filter using equation (17) in Chapter 4. Figure (5-19), illustrates the image before and after using an anisotropic filter on FPLT (at cross section).

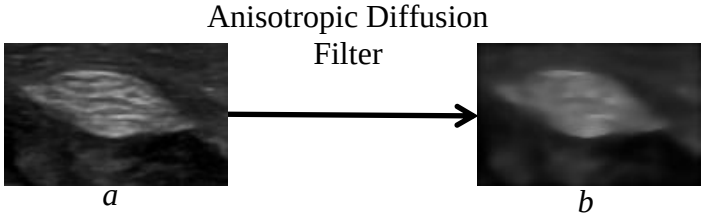

Figure (5-19) Speckle noise reduction on FPLT (sample1), figure (*a*) and figure (*b*) represent image before and after enhancement respectively.

The second step is implementation of fuzzy edge detection method on the enhanced image in figure (5-19)*b*, this step consists of three stages. The first one is fuzzification and selection of appropriate parameters for membership functions (Cp_0, Cp_1, Cp_2, and Cp_3). These parameters were selected according to the SD curve. Figure (5-20), shows the SD curve of sample 1 after image enhancement. The SD curve is formed by determining SD of a set of thresholded images, the range of cut-off points between minimum and maximum values of the image.

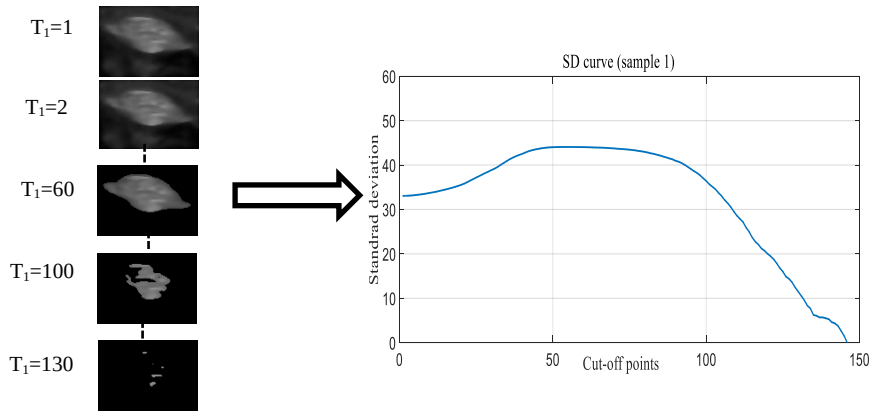

Figure (5-20), illustrates the plot of the SD curve, where the first cut-off point is 1, which represents the minimum grey level intensity in the input image of the sample 1, the last cut-off is 146, this value represents the maximum grey level intensity in the input image, so we have 145 cut-off points.

Extraction of SD_1 and SD_{max} from SD curve was achieved (as described in section 5.2.3.1). SD_K was calculated using equation (37) at different values of m_k; a set of parameters (Cp_0, Cp_1, Cp_2, and Cp_3) were extracted at every change of m_k value, so we can generate a matrix, which includes this information. Each row of this matrix illustrates different parameters of the membership function. Selection of the best value of m_k depends on the evaluation of $RBEM_k$, $RBEM_k$ is calculated using equation (34), the best value of m_k will be chosen at high score of RBEM.

Twelve fuzzy rules in the section 5.2.3.2 were applied to the image of sample 1 (see figure (5-19)*b* after implementing the fuzzification stage and construction of three membership functions. Three levels of edge detection information were obtained after defuzzification using equation (38); an edge detection image, which includes necessary information will be kept, and pixel information from other levels such as texture or sporadic pixels will be rejected. Sometimes it is necessary to utilize post-processing such as morphological operations (thinning) (Haralick and Sternberg, 1987). This is used as a post-processing step to remove isolated pixels or to get single pixel thickness in the final edge detection image. RBEM was employed to do assessment between the final edge detection image and ground truth image. The value of SD_K controls the decision of all levels of information because the intersection between SD_k and SD curve determined the parameter values (Cp_1, Cp_2). Figure (5-21), shows selection of the best value of m_k based on RBEM evaluation to calculate SD_K and then get the best obtained parameters (Cp_1, Cp_2) of the membership functions in the case of sample 1. The best value of m_k is 0.1 at $RBEM_k$ = 0.621.

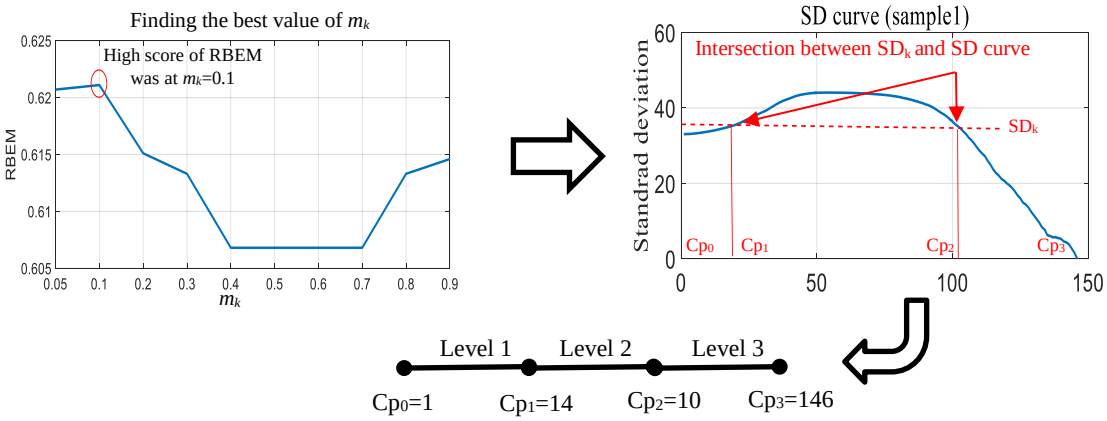

Figure (5-21) Steps of obtaining proper parameters of membership functions at different levels (level 1, level 2 and level 3). Step 1 was optimization of m_k, step 2 was evaluation of SD_k and third step was extraction parameters (Cp_0, Cp_1, Cp_2, and Cp_3).

Figure (5-22), demonstrates three levels of edge detection information, level 2 describes shape configuration of FPLT (at cross-section). Morphological operation (thinning) helps to get a single layer of pixel's edge instead of double layer, see figure (5-23). Sometimes, this step is useful to avoid inclusion of thick edges and isolated pixels in the measurements. In the case of practical application, it is not necessary to perform all measurements of RBEM, if this can be avoided (Pratt, 1978).

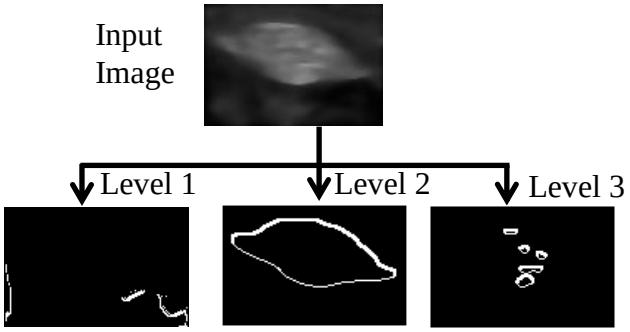

Figure (5-22) shows input image (sample 1), edge detection images at three different levels of information by using fuzzy edge detection method. Level 1 shows background information, and level 3 illustrates the information inside the object (texture information), while level 2 outlines the object shape.

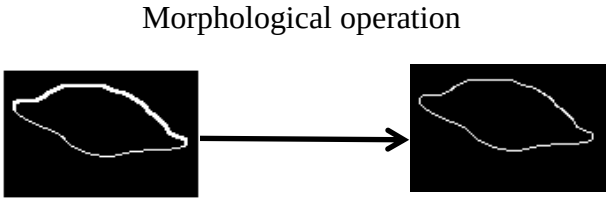

Figure (5-23) Edge detection image before and after thinning.

The same procedure was done on the rest of the 25 healthy image samples. To evaluate fuzzy edge detection method's performance, Pratt's FOM, Pinho and RBEM were employed. Furthermore, the fuzzy edge detector was replaced with a Canny edge detector (Canny, 1986); the same metrics were employed on it to see performance difference between the two

methods. Table (5-4) demonstrates the quantitative assessment of all healthy samples (25 images) using fuzzy and Canny edge detector. High scores in these metrics denote high performance for the method.

Table (5-4) Quantitative assessment of the 25 healthy samples (Experiment 1).

N	**FEDM**			**Canny**		
	RBEM	**FOM**	**Pinho**	**RBEM**	**FOM**	**Pinho**
1	0.621	0.653	0.500	0.600	0.192	0.245
2	0.618	0.540	0.418	0.600	0.400	0.300
3	0.604	0.500	0.407	0.600	0.401	0.370
4	0.616	0.540	0.402	0.615	0.273	0.300
5	0.615	0.51	0.402	0.609	0.390	0.333
6	0.606	0.47	0.360	0.600	0.233	0.265
7	0.620	0.609	0.447	0.604	0.290	0.296
8	0.620	0.613	0.440	0.612	0.217	0.254
9	0.620	0.55	0.407	0.611	0.264	0.301
10	0.600	0.234	0.250	0.615	0.132	0.190
11	0.612	0.560	0.436	0.605	0.347	0.334
12	0.611	0.433	0.401	0.600	0.333	0.313
13	0.614	0.345	0.328	0.604	0.192	0.242
14	0.625	0.509	0.400	0.616	0.166	0.221
15	0.612	0.536	0.403	0.596	0.196	0.237
16	0.617	0.408	0.374	0.617	0.216	0.265
17	0.622	0.255	0.300	0.614	0.123	0.176
18	0.612	0.533	0.433	0.600	0.206	0.258
19	0.619	0.408	0.333	0.610	0.316	0.324
20	0.605	0.345	0.290	0.588	0.224	0.255
21	0.618	0.408	0.370	0.61	0.267	0.304
22	0.623	0.500	0.411	0.610	0.176	0.230
23	0.623	0.430	0.420	0.611	0.200	0.242
24	0.613	0.600	0.430	0.586	0.256	0.265
25	0.611	0.602	0.430	0.586	0.391	0.320
Mean	0.615	0.501	0.400	0.600	0.256	0.273
SD	0.006	0.108	0.055	0.009	0.083	0.046

Summary of statistical comparison of three metrics (RBEM, FOM and Pinho) for both methods (FEDM and Canny) of the 25 samples is in the figure (5-24). Figure (5-24)*a* illustrates the means values of three different metrics. Based on the evaluation of T-test, the *p* values were 0.000028 for RBEM, 0.00003 for FOM and 0.00015 for Pinho. As the *p* values were under 0.05, so there is statistically significant difference between FEDM and Canny methods. Moreover, the right side of the figure, figure (5-24)*b* shows the evaluation of

standard deviation of three metrics of all samples. The *p* values using F-test were reported as 0.1046 for RBEM, 0.1890 for FOM and 0.402 for Pinho. These values provide sufficient evidence to conclude that there are no significant differences between the variances of two methods because *p* values are over 0.05.

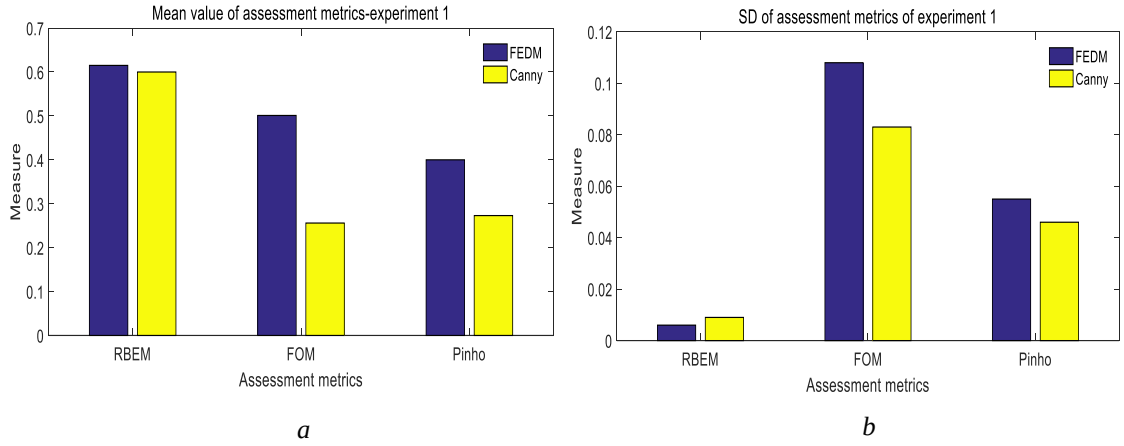

a *b*

Figure 5-24), illustrates the statistically comparison of FEDM and Canny method of experiment 1.

5.2.4.2 Experiment 2

The same previous steps in experiment 1 were applied on experiment 2, which includes: data collection, denoising as pre-processing step, implementation of fuzzy edge detection method (FEDM). However, in this experiment, FEDM was applied on the grey level and binary image, while FEDM was carried out in experiment 1 only on the grey level intensities image.

Regarding data collection, data were collected from 25 healthy volunteers (9 females and 16 males) and from arm region (protocol 2), all details in section 3.3.2.1. The collected images illustrate one snapshot of the triceps muscle in a longitudinal section. However, only 20 image samples were used in this experiment due to some limitations such as presence fat layer and subcutaneous tissue on the upper aponeurosis of the muscle. These limitations have

an impact shown on the orientation of the upper and lower aponeurosis (it has curve shape instead of straight line) as shown in the figure below: -

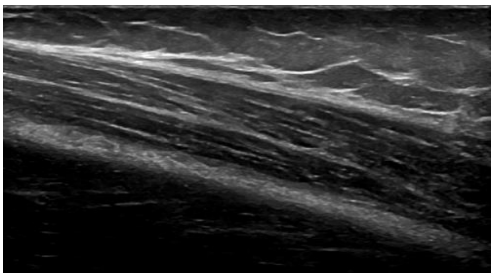

Figure (5-25) Example of ultrasound imaging (one snapshot of triceps muscle), which shows fat and subcutaneous tissue layer above the upper aponeurosis.

Moreover, 20 ground truth images for these samples were drawn by an expert, who concentrated on identifying the upper and lower aponeurosis of triceps muscle in the ground truth images.

Following steps in figure (5-26) which present the pipeline of detection upper and lower aponeurosis from an ultrasound image of the triceps muscle. These aponeuroses appeared in the top and the bottom of the image respectively, as thicker and brighter lines compared with muscle fascicle.

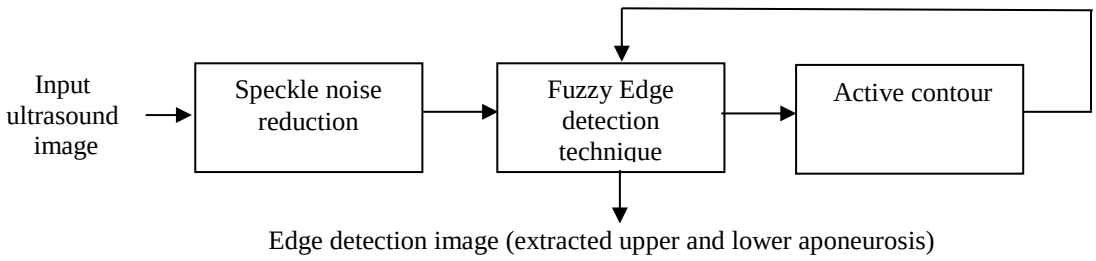

Figure (5-26) Steps of extraction of upper aponeurosis and lower aponeurosis from ultrasound image.

Figure (5-27) introduced some results of sample 1 (ultrasound image of the triceps muscle) after following the steps in the figure (5-26).

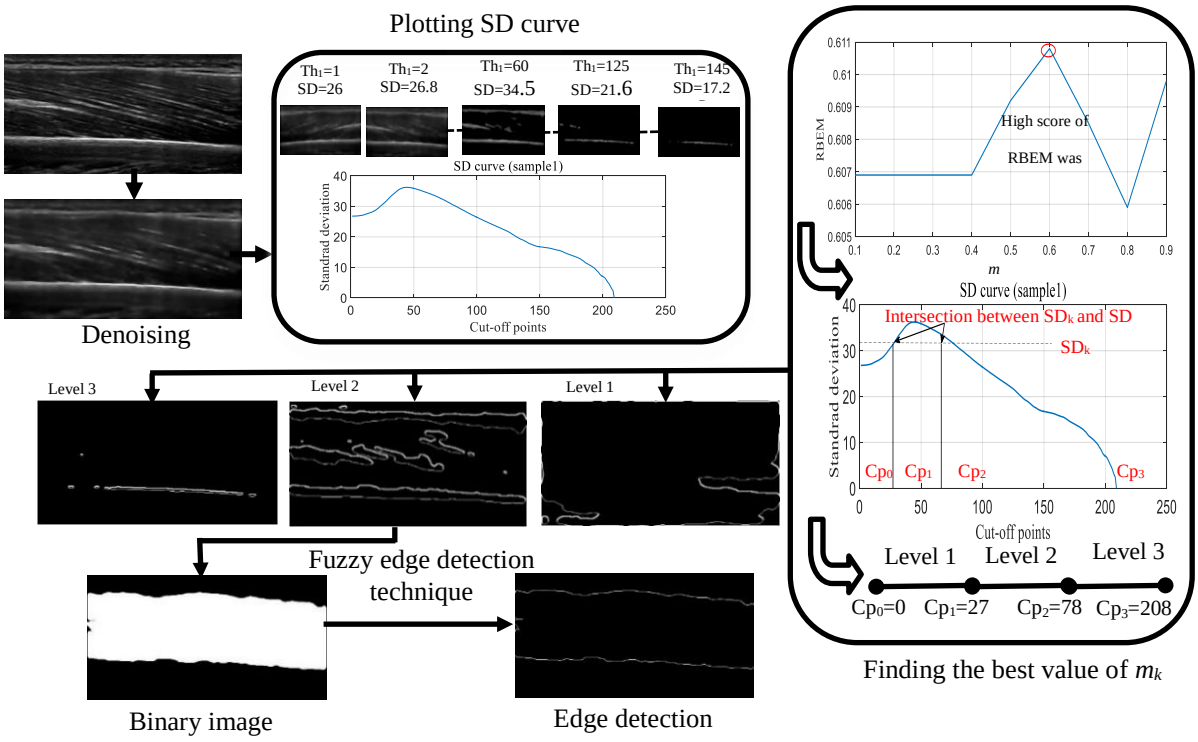

Figure (5-27) illustrates the pipeline of performing processing steps of experiment 2, starting from input ultrasound image and denoising as the pre-processing step. Following this step by implementing fuzzy edge detection technique on the image, this step includes plotting SD curve, selecting the best value of m_k, getting parameters (Cp0, Cp1, Cp2 and Cp3) then extraction of three edge detection images. Applying active contour on level 2 to get the binary image then getting the final edge detection image using fuzzy edge detection technique on the binary image.

In the case of performing fuzzy edge detection technique on the binary image, only one level of edge detection image can be extracted because it is the binary image which has only two cut-off points, see figure (5-28) below.

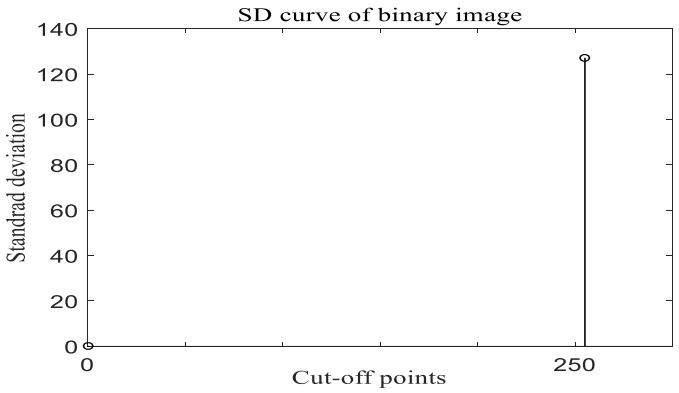

Figure (5-28) illustrates SD curve, the value of $SD_k = SD_{max.}$

The same steps were applied to the rest of the 20 samples and compared with images after using Canny edge detection technique. The quantitative assessment of the 20 healthy samples in the (Experiment 2) are shown in the table (5-5).

Table (5-5) Quantitative assessment of the 20 healthy samples (Experiment 2).

N	FEDM			Canny		
	RBEM	FOM	PINO	RBEM	FOM	PINO
1	0.6092	0.5423	0.3902	0.6086	0.0672	0.1091
2	0.6251	0.3343	0.2461	0.614	0.0991	0.1458
3	0.6140	0.4120	0.3050	0.6244	0.0959	0.1373
4	0.6079	0.4596	0.3440	0.6141	0.0894	0.1358
5	0.6133	0.3385	0.2537	0.6176	0.0872	0.1344
6	0.6202	0.3235	0.2375	0.6121	0.1028	0.1462
7	0.6200	0.2706	0.2257	0.6185	0.0862	0.1297
8	0.6247	0.2730	0.2166	0.6131	0.0644	0.1031
9	0.6271	0.2588	0.2098	0.6227	0.0598	0.0843
10	0.6187	0.3187	0.2446	0.6167	0.0703	0.1074
11	0.6222	0.2272	0.1767	0.5982	0.0863	0.1276
12	0.6122	0.3593	0.2753	0.6252	0.0770	0.1123
13	0.6200	0.2591	0.2067	0.6262	0.0630	0.0932
14	0.6254	0.3543	0.2548	0.5841	0.0978	0.1514
15	0.6238	0.3915	0.3142	0.6237	0.0389	0.0642
16	0.6202	0.3179	0.2175	0.6064	0.1106	0.1596
17	0.6257	0.3292	0.2336	0.6055	0.1215	0.1721
18	0.6000	0.3369	0.2608	0.6000	0.1041	0.1541
19	0.6161	0.2568	0.2139	0.6215	0.0728	0.1101
20	0.6266	0.2713	0.2072	0.6259	0.0571	0.0899
Mean	0.6186	0.3317	0.2517	0.6139	0.0826	0.1234
SD	0.0073	0.0762	0.0521	0.0110	0.0208	0.0283

Figure (5-29) illustrates statistical comparison between FEDM and Canny based on evaluation of three different metrics (RBEM, FOM and Pinho). The *p* values of RBEM using T-test was 0.1217 and 0.0805 using F-test; therefore, there is no significant difference between FEDM and Canny methods. Whereas, in the case of FOM and Pinho metrics, a significant difference between the two methods was found (*p* value < 0.05) by using T-test and F-test. The *p* values of FOM were 0.00012 and 0.00054 using T-test and F test respectively, while the *p* values of Pinho were 0.00001 and 0.01 using T-test and F-test respectively.

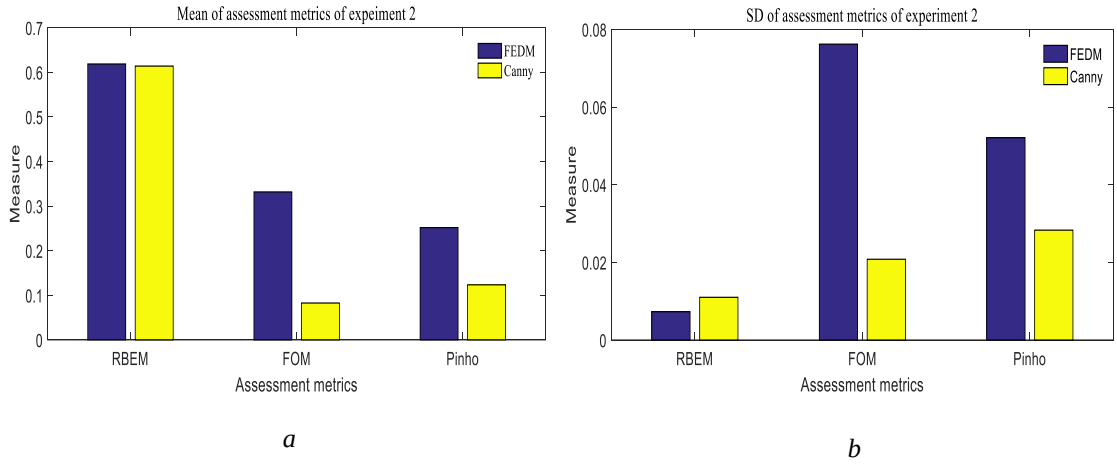

Figure (5-29), illustrates the statistically comparison of FEDM and Canny method of experiment 2.

In terms of noise affecting the results, fuzzy edge detector was applied on the ultrasound image without addressing speckle noise to investigate the superiority of the performance of fuzzy edge detector technique; figure (5-30) illustrates some artifacts which have a negative impact on the evaluation of geometric information of FPLT.

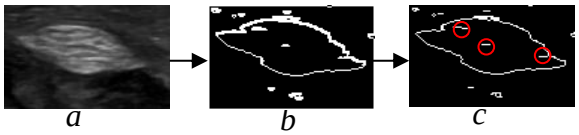

Figure (5-30) Input ultrasound image (sample1) without doing denoising processing is shown in figure (*a*), while figure (*b*) and (*c*) represent the result of image after applying fuzzy edge detector and thinning respectively. In figure (*c*), some artifacts were noticed due to the impact of the noise on the image (see red circles in figure (*c*)).

Furthermore, some metrics of edge measurements (Pratt's FOM, Pinho) of the sample 1 without denoising receded more than 50% compared with the previous values in the case of performing speckle noise reduction before employing fuzzy edge detector on this sample. Where Pratt's FOM =0.157, Pinho = 0.215 and RBEM =0.607 compared with these values which employed with denoising, see table (5-4).

For further applications such as evaluation of cross-section area of tendon or muscle thickness, it is difficult to get accurate evaluations based on the resulting image from Canny edge detector, see figure (5-31)*b*. The main reason is the unnecessary information and artifacts inside in the image, in contrast with the figure (5-31)*c* which includes a clear boundary of cross-section tendon without extra information on it.

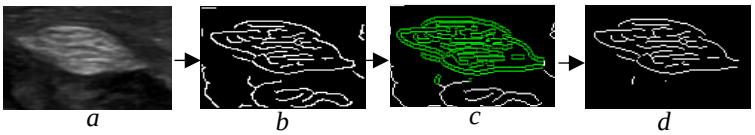

Figure (5-31), figure (*a*) represent image after denoising. The result of image after applying Canny edge detector on the image is shown in figure (*b*), while figure (*c*), shows using active contour on the image in figure (*b*) to extract binary object. Figure (*d*) demonstrates the difficulty in isolating the boundaries of the tendon at cross-section from its background due to unnecessary information inside the object.

Another example in the figure (5-32)*b*, it is impossible to calculate triceps muscle thickness due to extra edge information in the image, while muscle thickness of image in figure (5-32)*c* can be calculated at different points.

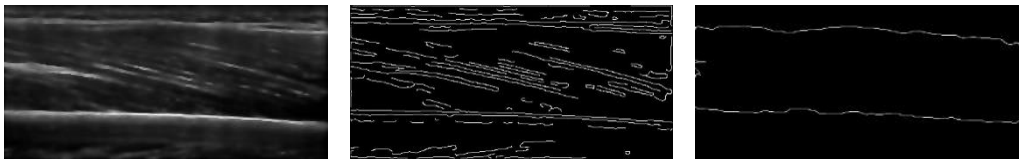

Figure (5-32), where figure (*a*) represents the result of image after denoising and figure (*b*) presents the image after applying Canny edge detector on the image in figure (*a*), while figure (*c*) illustrates image after following steps in the figure (5-26).

5.2.5 Discussion

Grey level intensities of MUI are noisy and highly variable due to the nature of the ultrasound image and the musculoskeletal structure, so a fuzzy technique is an appropriate choice to represent it. The main contribution of this work is to identify necessary information in the ultrasound image for these evaluations using fuzzy edge detection method. This approach offers a successful way of isolating the edge of the musculoskeletal ultrasound image into three different levels of edge information. The basic idea of this approach is derived from a fuzzy inference method with carefully selected fuzzy parameters of membership function based on standard deviation (see figure (5-20) in experiment 1 and figure (5-27)). Experiment 2 shows an example of the SD curve of the image after speckle noise reduction. According to this curve, parameters (Cp_0, Cp_1, Cp_2, and Cp_3) were extracted and detection of these parameters helped in the construction of three membership functions. This is a new way of identification of the parameters which control the behaviour of membership functions. Edge detection was carried out using 12 fuzzy rules. This produces three levels of edge detection information. In all image samples, the images resulting from the 2nd level showed more details because this level contained the highest value of SD, while the images of levels 1 and 3 contained unnecessary image details (as shown in figure (5-22)). At times, if edge detection of the ultrasound image included all details of image information, it was more challenging to perform the necessary calculations, see figure (5-31)*b* and figure (5-32)*b*. Also, another example, in the case of measuring the length of the muscle fascicle, if the edge detection image has all detail levels in one image, it is hard to evaluate the length of the muscle fascicle automatically; unnecessary information in the form of artifacts can mask the true edges.

Fuzzy edge detection method was applied successfully on the grey level ultrasound images as experiment 1, and experiment 2 to extract three levels of edge detection images. Also, it is possible to extract edges from the binary image using this method as in experiment 2.

To assess the fuzzy edge detection method performance, Pratt's FOM, Pinho and RBEM were utilised for this purpose. In experiment 1, the mean value of the recent assessment metric (RBEM) scores for all samples reported over 0.6 and for Pratt's FOM and Pinho were 0.5 and 0.4 respectively. In addition, there is a tiny difference in the RBEM score between all samples, the standard deviation was approximately 0.006, see table (5-4). In contrast with the traditional method (Canny edge detector), Pratt's FOM and Pinho metrics were reported around 0.25, while the standard deviation of RBEM was 0.009. Regarding experiment 2, the performance of FEDT outperforms the performance of the traditional edge detection method using Canny operator technique, based on the evaluation of three assessment metrics (Pratt's FOM, Pinho and RBEM), see table (5-5).

5.2.6 Conclusions

The presented work in this part of the thesis represents a successful approach for the extraction of image edges from grey level intensity ultrasound and binary image. Furthermore, the parameters of fuzzy membership functions were set up depending on the analysis of a Standard Deviation curve that built-up from a set of thresholding images.

Fuzzy edge detection method is more powerful than another method (Canny edge detector) because it can specify different levels of edge detection information with a good score of quantitative assessment in all samples. In addition, it is an efficacious way for edge detection of MUI as it preserved time compared to other machine learning techniques such as training

CNNs. The CNN approach depends on extensive training datasets and it can detect image edges based on what they are trained.

In this thesis, fuzzy edge detection method was introduced as a novel method to achieve edge detection of musculoskeletal ultrasound images and used in further applications in Chapter 6.

Chapter Six

Analysis of the Musculoskeletal Ultrasound Image

Chapter 6 Analysis of the musculoskeletal ultrasound image

6.1 Introduction

The main purpose of this chapter is the analysis of musculoskeletal ultrasound images of the upper limb to estimate some musculoskeletal parameters such as muscle thickness, tendon thickness and pennation angle. This process can be performed manually based on the skills of an expert and using measurement options of the ultrasound machine. However, the manual method is inherently prone to over or underestimation of the measurement and it is time consuming (Giot et al, 2016). Furthermore, due to the complex texture features of the musculoskeletal ultrasound images, it is difficult to give accurate measurements. Therefore, in this thesis, an automated method was developed to achieve this analysis, which depends on an underlying analysis of the properties of the musculoskeletal ultrasound image.

The implementation of the automated analysis requires pre-processing steps such as image enhancement and segmentation to make musculoskeletal ultrasound image more readable and suitable for automatic measurements.

Comparison between manual and automatic measurements was proposed to assess the agreement between these methods during the evaluation process of the morphological parameters of upper limb.

6.2 Manual measurement

Manual measurement is the most popular method, which has been used in the clinical diagnosis and research. Manual measurement in the ultrasound machine depends on the quality of the operator and experience who works on the ultrasound machine. After ultrasound scanning, musculoskeletal ultrasound images were saved in the ultrasound machine as DICOM (Digital Imaging and Communications in Medicine) format, then

analysed offline manually. In the case of using it in the external computer, these images are saved as JPEG (Joint Photographic Experts Group) format to analyse it automatically.

6.3 Automatic measurement

The primary purpose of the automation measurements is improving productivity, raising the accuracy and consistency of measurements compared to the manual measurements. Automatic analysis can help to overcome two previously mentioned limitations: speckle noise and low image contrast in the domain of MUI. Furthermore, it is possible to highlight the main details, which describe the configuration of the object inside the image using edge detection method. Image analysis is the last step to achieve automatic measurements, and it evaluates the same geometric parameters which were determined by manual measurements. In this thesis, these parameters are the thickness and pennation angle of the medial head of triceps muscle, also cross-sectional area and circumference of flexor pollicis longuis tendon. In the automatic measurement, figure (6-1) illustrates the diagram of musculoskeletal ultrasound analysis using automatic measurements.

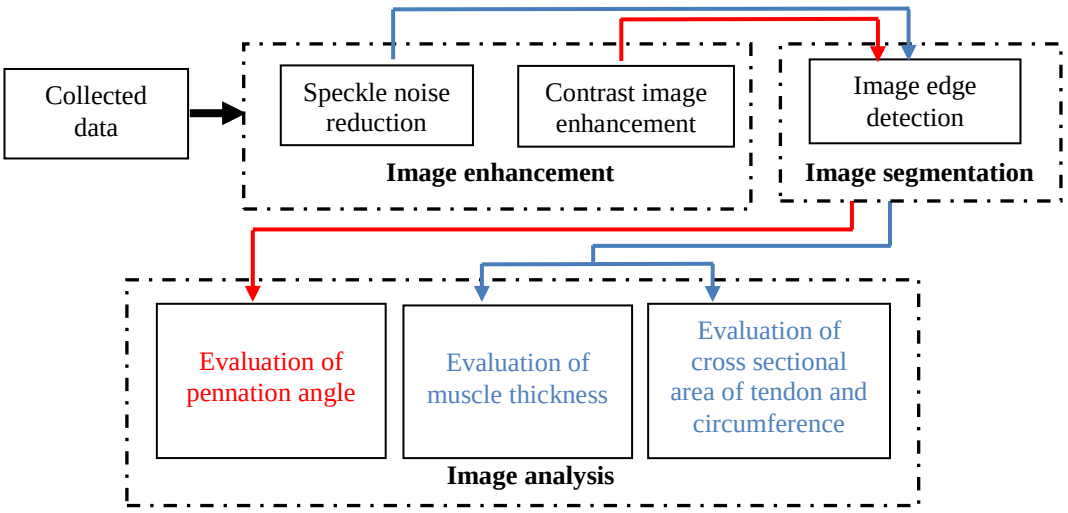

Figure (6-1), illustrates the framework of automatic method to evaluate some of morphological parameters of musculoskeletal system in the upper limb.

From the figure (6-1) above, image analysis requires pre-processing steps such as image enhancement (speckle noise reduction and image contrast enhancement) and image segmentation (edge detection). Selection of pre-processing steps depends on the objective of the evaluations. For instance, if the objective is thickness evaluation of muscle or tendon, speckle noise reduction and edge detection steps are selected to extract only necessary information. On the other hand, if we proposed to determine the pennation angle, using contrast image enhancement step is likely to illustrate key features such as fibre orientation.

6.4 Comparison between manual and automatic measurements.

Differences between the automatic and manual measurement results were investigated using Bland–Altman plots (Bland and Altman, 1986). In this graphical method, the average of manual and automatic measurements is plotted against the difference between them, see figure (6-2).

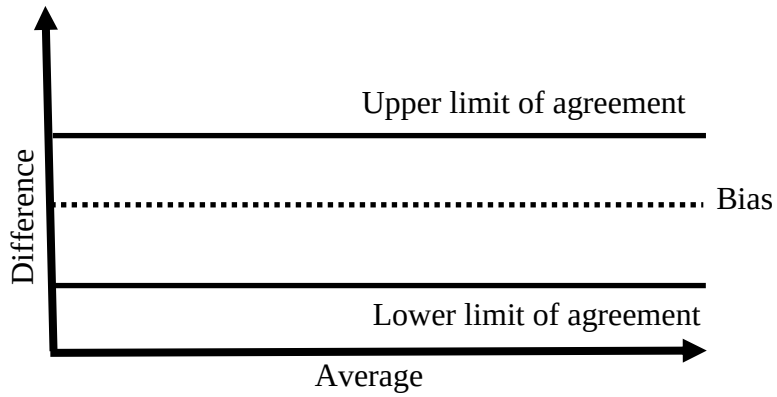

Figure (6-2) Brief description of Bland Altman plot.

From figure (6-2), bias represents the mean of the difference between two measurements. Moreover, the upper and lower limit of the agreement can be calculated using (mean

difference + 1.96 SD and mean difference - 1.96 SD) respectively, giving a 95% confidence limit. SD is standard deviation SD of the difference between two measurements (Bland and Altman,1986). It is necessary to make sure and check that the distribution of the measurements values follows normal distributions.

6.5 Experiments and results

6.5.1 Experiment 1

The objective of this experiment is the evaluation the circumference and cross-sectional area of the flexor pollicis longus tendon using manual and automatic measurement tools. The data, which is used in experiment 1 is collected from 25 recruited volunteers (9 females and 16 males) and from hand region (protocol 1), all details in section 3.3.2.1.

6.5.1.1 Manual measurement

The cross-sectional area was determined by tracing the border of the tendon and calculating the endorsed area, given in cm^2 using ultrasound machine software, see figure (6-3).

Figure (6-3) Evaluation of cross section area of flexor pollicis longus tendon at transverse plane and one ultrasound image snapshot manually. This area was evaluated in cm^2 by tracing the border of tendon at cross section, so the cross-sectional area is 0.19 cm^2 .

Since the cross-section of flexor pollicis longus tendon is an irregular shape, the circumference was determined by accumulating small straight distances around the cross-section of the tendon. The number of the small straight lines depends on how straight line can cover small distance around cross-section of the tendon; therefore, this evaluation is mostly subjective, see figure (6-4).

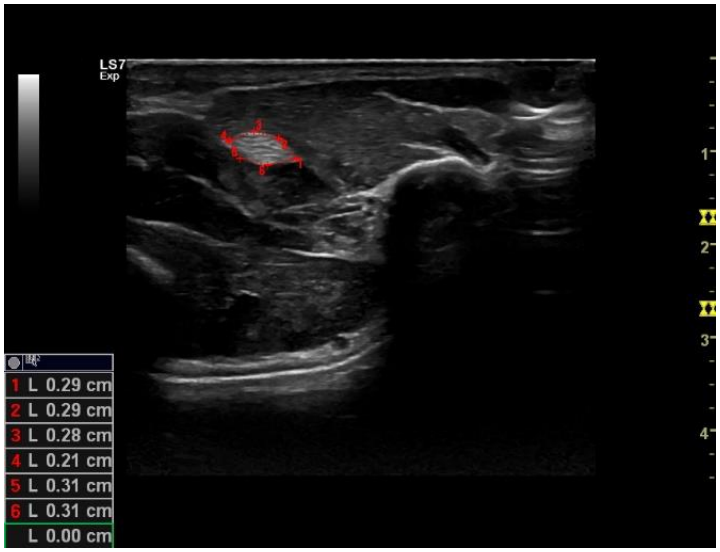

Figure (6-4) The circumference determination of the flexor pollicis longus tendon at transverse plane (one ultrasound image snapshot) is shown manually. This circumference was evaluated in cm by gathering small straight distances around the cross section of the tendon. The circumference in this evaluation was 1.69 cm

6.5.1.2 Automatic measurement

The strategy of the automatic evaluation of the circumference and cross-sectional area of FPLT is presented by several steps as in the figure (6-5).

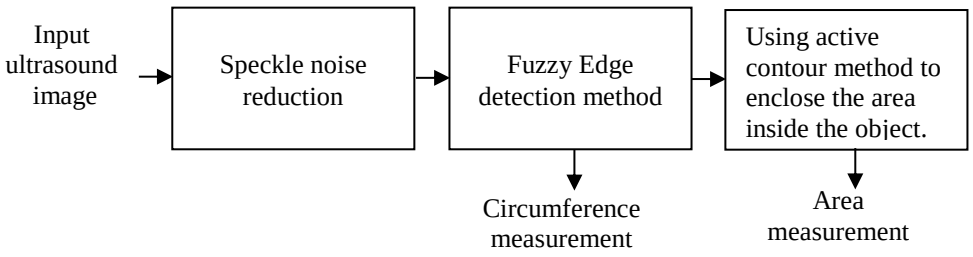

Figure (6-5) Steps of the evaluation area and circumference of the FPLT at cross-section.

Starting with step1 in the figure (6-5), speckle noise reduction was carried out using the anisotropic filter, which was described in chapter 4 -part 1, using equation (17). Fuzzy edge detection was carried out according to the methods described in Chapter 5-part 2, section

5.2.3. The result of the edge detection image is the fundamental step in the evaluation of geometric parameters of the musculoskeletal ultrasound image because it can convert an image from the high level (grey level intensities) to the low level (white and black colour). Therefore, in the automated measurement, circumference was measured based on resultant edge detection image by counting white pixels at the borders of FPLT (at cross section), then converted to millimetres (mm). Active contour-based segmentation (Krueger et al., 2008) is a powerful way to isolate an object from its background. After isolation, it is possible to get an object with white pixels and background with black pixels. The area can be determined by counting white pixels of the isolated objected and then converting the pixel area to physical units of area (mm^2).

However, a successful active contour method depends on the homogeneity of the image intensity and placement of the initial contour. For example, some musculoskeletal US images had heterogeneous regions even if the image had been enhanced by speckle noise reduction. If an object consists of a high-intensity heterogenous region, more than one initial contour could be produced, and different objects will be segmented, see figure (6-6). Active contour based on segmentation method was performed using Matlab tools (version 8.6). The Matlab code of active contours-based segmentation was performed, started firstly with defining the initial contour position and growing until all the area of the object was included. To get the best separation of an object from its background, the position of the initial contour should be close to the object boundaries.

a *b* *c* *d* *e* *f*

Figure (6-6), *a*, *b* and *c* represent the ultrasound image of sample 17, after applying active contour on this image and extracting binary object. Figure *d* illustrates the image after speckle noise reduction, while figure *e* illustrates isolated objects by active contour to achieve binary image in figure *f*.

Therefore, sometimes it is hard to gather all the pixels of the object in one contour and calculate its area precisely. Employing active contour method-based segmentation on a region, which is enclosed by edges helps to cover the cross-sectional area of the tendon (irregular shape), see figure (6-7). In this case, initial contour is growing until it includes all the homogenous area (black pixels) and stops at the edges (white pixels).

a *b* *c*

Figure (6-7), *a* represents the ultrasound image of sample 17 after speckle noise reduction. The image in figure *b* shows employing active contour on the edge detection image (resultant image after using FEDM), while figure *c* depicts the binary object.

Figure (6-8) presents some successful examples of the evaluation of cross-sectional area of the FPLT by using active contour method.

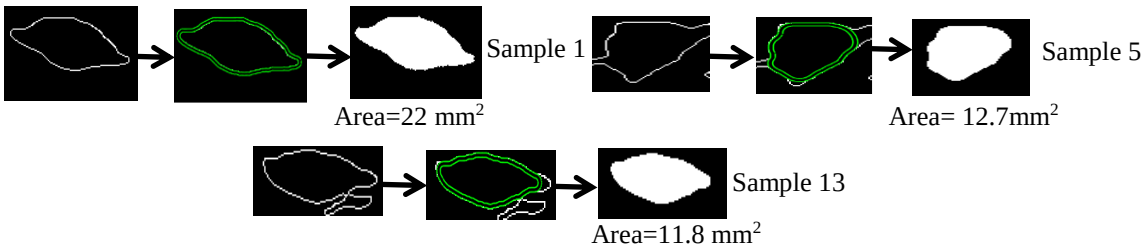

Figure (6-8), the first line illustrates calculation of cross section area of sample 1 and sample 5 using active contour-based segmentation method, while the second line shows the area calculation of the sample 13.

Concerning noise affecting the results, fuzzy edge detector was applied on the ultrasound image without addressing speckle noise to investigate the superiority of the performance of fuzzy edge detector technique; figure (6-9) illustrated some artifacts which have a negative impact on the reality of evaluation of geometric information of FPLT.

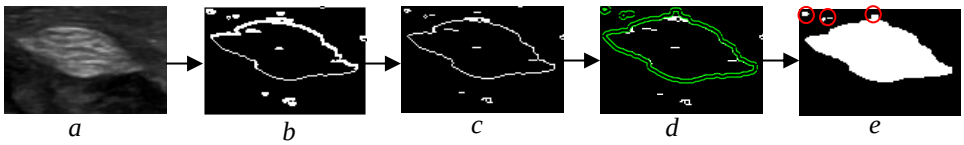

Figure (6-9), *a* shows input image (sample1) without doing denoising processing. Figure *b* and figure *c* represent the result of image after applying fuzzy edge detector and thinning respectively. Active contour was applied on the image in figure *c* to get the result as shows in figure *d* and extracted binary object as shown in figure *e*. In figure *e*, some artifacts were noticed due to the impact of the noise on the image (see red circles in figure *e*).

6.5.1.3 Comparing between manual and automatic measurements

Bland-Altman plot was constructed to measure the agreement between manual and automatic measurements of the circumference and cross-sectional area of the FPLT as are shown in figure (6-10) and figure (6-11) and this data is normally distributed. From figure (6-10) we can observe some values decrease as the other increase (negative correlation). In

this case, the negative slope indicates that the size of the error increases in proportion to the size of the measurement, as the (negative) difference increases with increasing average.

On the other hand, figure (6-11) illustrates scattering values around the bias line get randomly smaller and larger as the average gets higher. In the case of cross-sectional area measurements, the difference between the two methods was 1.07 mm^2. The plot shows a good agreement in most of the samples between manual and automatic determination of the tendon cross-sectional area. In the case of the circumference estimation, the difference was more significant, as one would expect with this type of estimating, where errors in both directions are cumulative. For our application in estimating musculotendon parameters for biomechanical modelling, the calculation of the area is of far greater importance. Evaluation of cross-sectional area of a tendon is one of the important parameters to be studied in the musculoskeletal modelling design (Horsman et al., 2007).

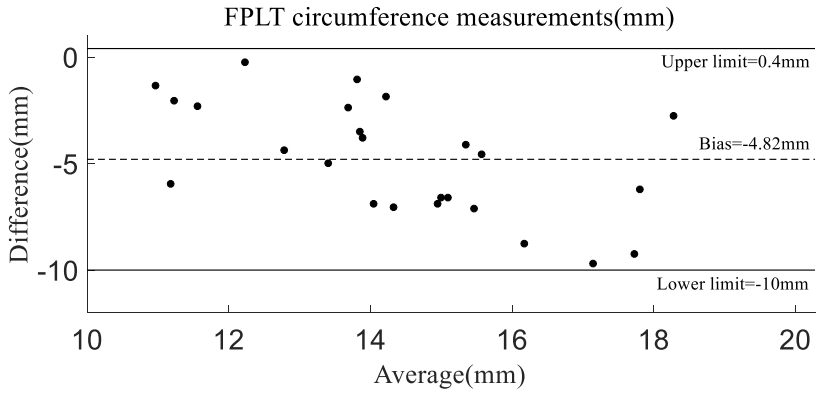

Figure (6-10) Bland-Altman plot of circumference measurements of FPLT in mm.

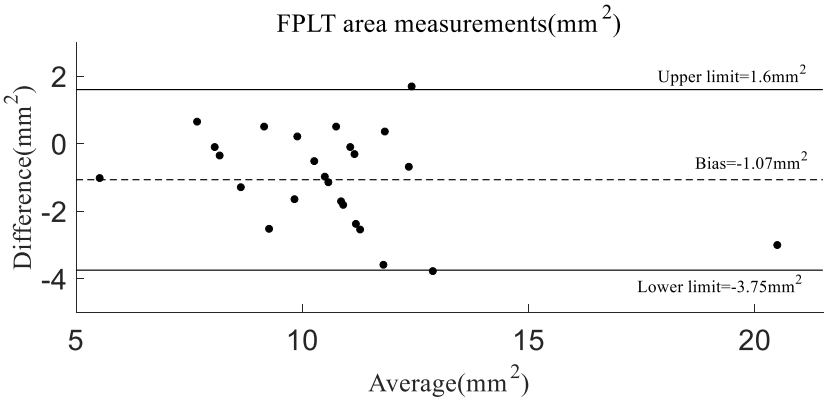

Figure (6-11) Bland-Altman plot of cross-sectional area measurement in $mm^{2.}$

6.5.2 Experiment 2

The main purpose of experiment 2 is determining the thickness of the triceps muscle at longitudinal section (one snapshot of ultrasound image). Data was acquired from 25 volunteers (9 females and 16 males) and from arm region (protocol 2 all details in section 3.3.2.1). However, some samples suffered from the presence of the subcutaneous tissue layer on the upper aponeurosis of the muscle as in the figure (6-12).

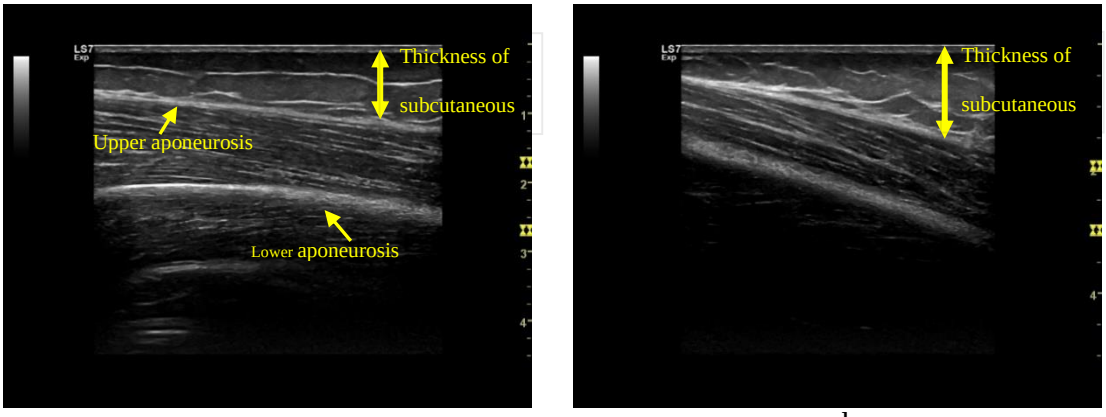

a b

Figure (6-12) presents two different samples, which include subcutaneous tissue layer above the upper aponeurosis of the muscle.

The fundamental question is: did this limitation influence the manual and automatic evaluations? Manual method should not be affected with this limitation because one can easily spot aponeurosis of the muscle and measure the distance between them despite some changing in the direction and shape of muscle aponeuroses, see figure (6-13) below.

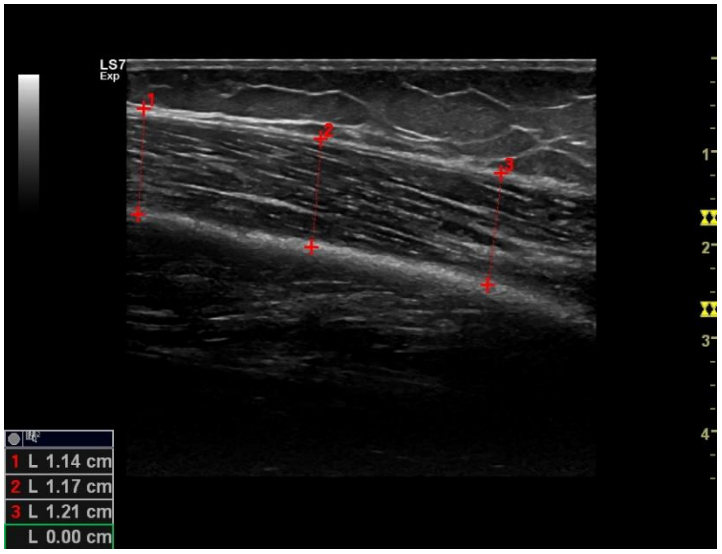

Figure (6-13) illustrates a sample of the evaluation of the triceps muscle thickness in one ultrasound image snapshot manually. This sample includes layer of the subcutaneous tissue on the upper aponeurosis.

On the other hand, in the case of automatic evaluation it was possible to evaluate the thickness in only 20 volunteers due to this limitation because it is hard to extract a full aponeuroses configuration using the proposed method and following the steps of extraction of the upper and lower aponeuroses in the figure (5-26).

Figure (6-14) gives the example of edge detection image after performing fuzzy edge detection method on the image in the figure (6-12)*b*. We can observe the figure (6-14) did not define a full aponeuroses profile.

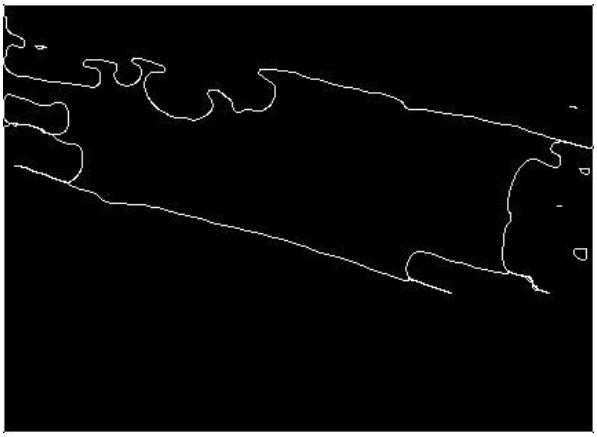

Figure (6-14), shows resulted image after applying fuzzy edge detection method on the image in figure (6-12)*b*, this image was restricted with subcutaneous tissue layer on the upper aponeurosis of triceps muscle.

6.5.2.1 Manual measurement

The thickness of triceps muscle was evaluated at three different places (proximal, middle and distal) by measuring the distance between the upper and lower aponeuroses. Figure (6-15), illustrates the sample of the thickness evaluation manually.

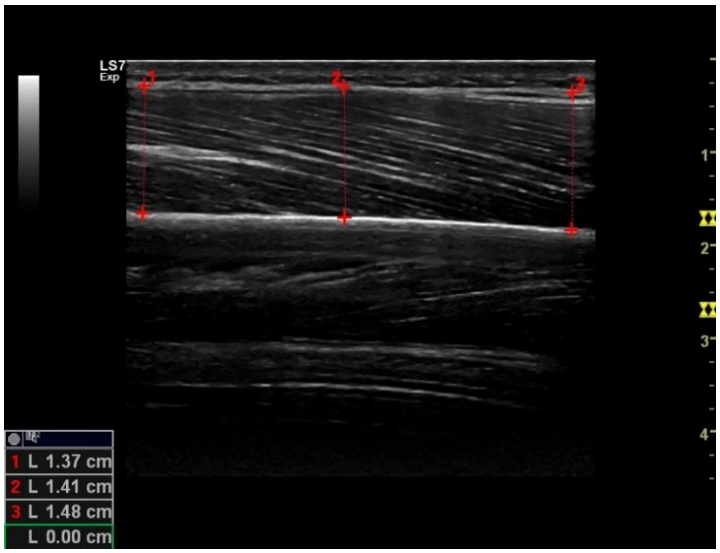

Figure (6-15) Sample of evaluation of triceps muscle thickness in one ultrasound image snapshot manually. Thickness was evaluated in cm, it is the average of three values: proximal, middle and distal measurement

6.5.2.2 Automatic measurement

In the figure (6-16), the same steps in experiment 1 are followed to get edge detection image. However, this image included both aponeuroses with extra information. Therefore, active contour-based segmentation method was applied to enclose the area between upper and lower aponeuroses; then fuzzy edge detection method was employed on the binary image to extract only upper and lower aponeuroses, see figure (5-27). The thickness of triceps muscle was calculated by measuring the distance between both aponeuroses by pixel and converted to mm automatically.

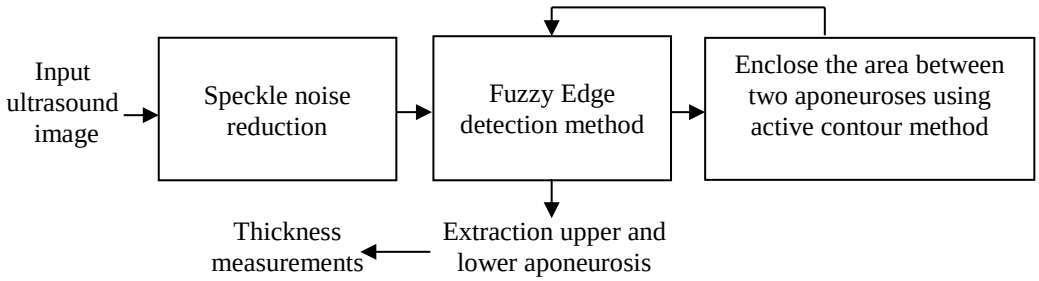

Figure (6-16) illustrates the steps of the thickness evaluation of triceps muscle in one snapshot of the ultrasound imaging.

The figure below shows the thickness evaluation of the sample 1 passing across different stages (speckle noise reduction, edge detection, using active contour and then muscle thickness evaluation at three different points).

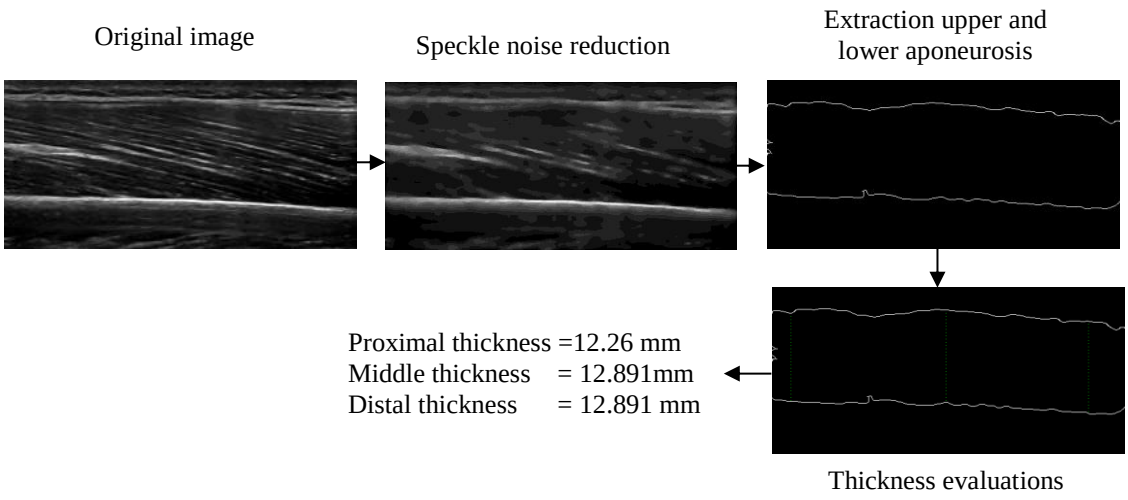

Figure (6-17) illustrates the results at different steps, which ended at thickness evaluation of triceps muscle at three different points (proximal, middle and distal).

6.5.2.3 Comparing between manual and automatic measurements

Again, in this experiment, Bland-Altman method was used to highlight the difference between manual and automatic measurements in the case of triceps thickness evaluation and this data is normally distributed. The most interesting aspect of this graph is that bias =0.115 mm. which represents the average discrepancy between two measures. It is a minimal value; this means the manual and automated measurement of the triceps muscle thickness have close results, see figure (6-18). From this figure we observe values are distributed randomly around the bias line as the average gets higher.

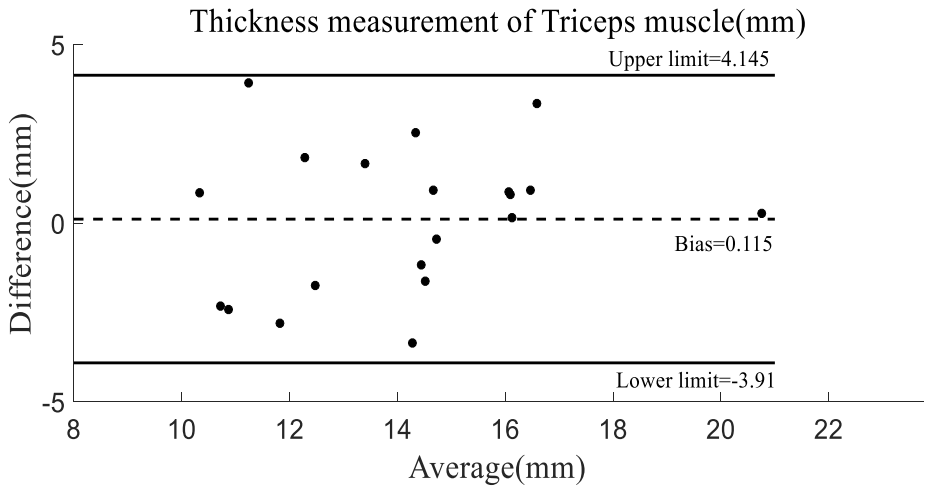

Figure (6-18) Bland-Altman plot of thickness measurement in mm for 20 volunteers.

6.5.3 Experiment 3

Experiment 3 is set out to calculate the pennation angle of the triceps muscle, the data of this experiment are the same data of experiment 2, which were collected from arm region (protocol 2, all details in section 3.3.2.1). This data has suffered from considerable limitations. The first one is the same limitation in experiment 2 (presence of subcutaneous tissue on the upper aponeurosis, see figure (6-12); this limitation affected the manual and automatic measurements of pennation angle. Another potential limitation is lack of clarity in the definition of the muscle fascicle orientation; therefore, it is hard to trace muscle fascicle even manually, see figure (6-19). As a result, the number of samples in the manual and automatic measurements is 10 samples that were not compromised by these problems.

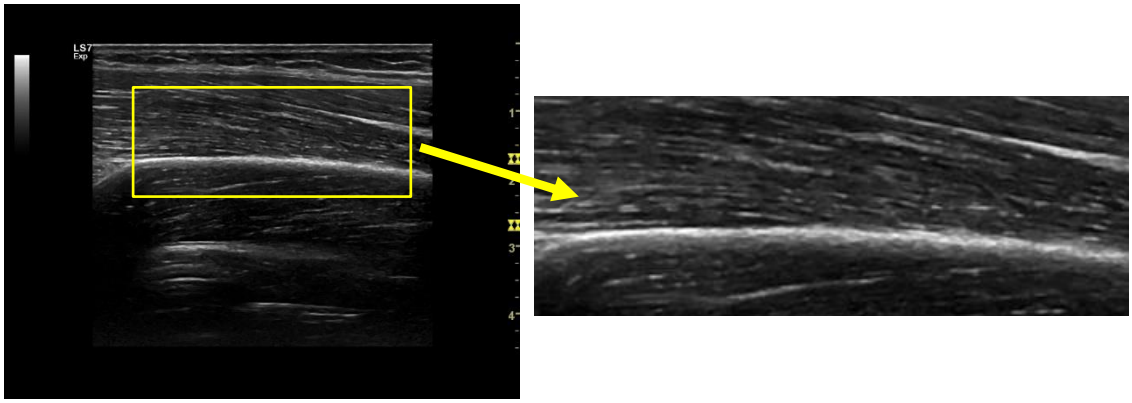

Figure (6-19) illustrates the difficulty of defining muscle fascicles orientation.

6.5.3.1 Manual measurement

The figure (6-20) shows the sample of evaluation of the pennation angle manually. Due to the nature of the triceps muscle architecture, and the use of just one snapshot, it is challenging to track the orientation of the muscle fibre from lower aponeurosis to upper aponeurosis to evaluate pennation angle. It is possible to reduce the impact of this problem by finding the straight line, which cuts the lower aponeurosis and goes up to cut the orientation of the muscle fascicle. This line is perpendicular on the lower aponeurosis, see figure (6-20), ultrasound machine has an option to measure angle based on the length of the lower aponeurosis and defining muscle fascicle length.

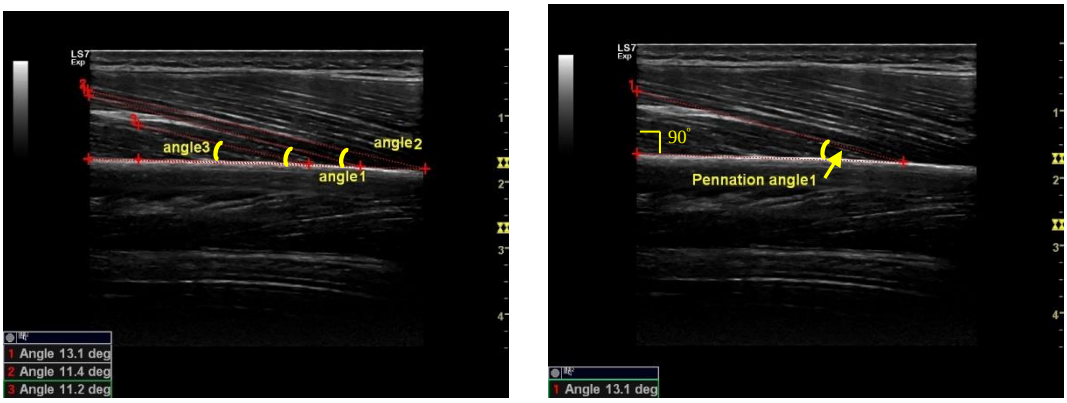

Figure (6-20) demonstrates the manual evaluation of the pennation angle of triceps muscle in one snapshot.

6.5.3.2 Automatic measurement

In this experiment, pre-processing steps were performed using local contrast enhancement method, see Chapter 4-part 2, section 4.2.4 and fuzzy edge detection method, see Chapter 5-part 2, section 5.2.3. After obtaining edge detection images, Hough transform method (Duda and Hart 1971) was used to detect muscle fascicle and lower aponeurosis, after cropping the image into the region of interest. The Hough transform is a detection technique that can be used to identify the features of particular shapes such as lines and circles, which best fits a set of given edge image pixels. The Hough Transform involves polar coordinates to show the parametric representation of a line. In this thesis, Hough transform was used to detect of the muscle fibre orientation and muscle aponeuroses. It was applied on musculoskeletal ultrasound images after applying fuzzy edge detection method on these images. After this detection, the length of the lower aponeurosis and muscle fascicle can be measured. The pennation angle is taken as the angle between the aponeurosis and the fibre direction.

Again, we faced the same difficulties in the evaluation of pennation angle manually. Figure (6-21) shows the pipeline of the determination of pennation angle automatically.

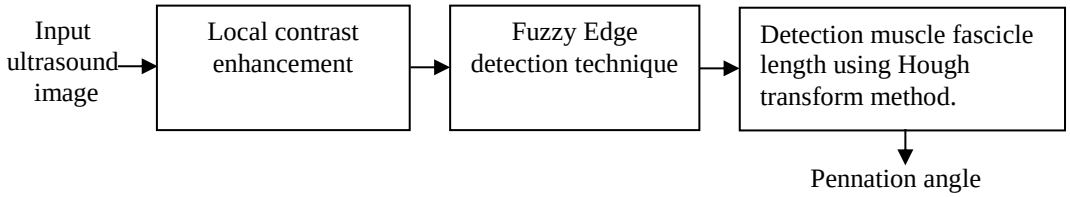

Figure (6-21) illustrates the steps of pennation angle evaluation of the triceps muscle in one snapshot of ultrasound imaging.

The result of the pennation angle evaluation of the sample 1 in the figure (6-22), this includes all steps in detail.

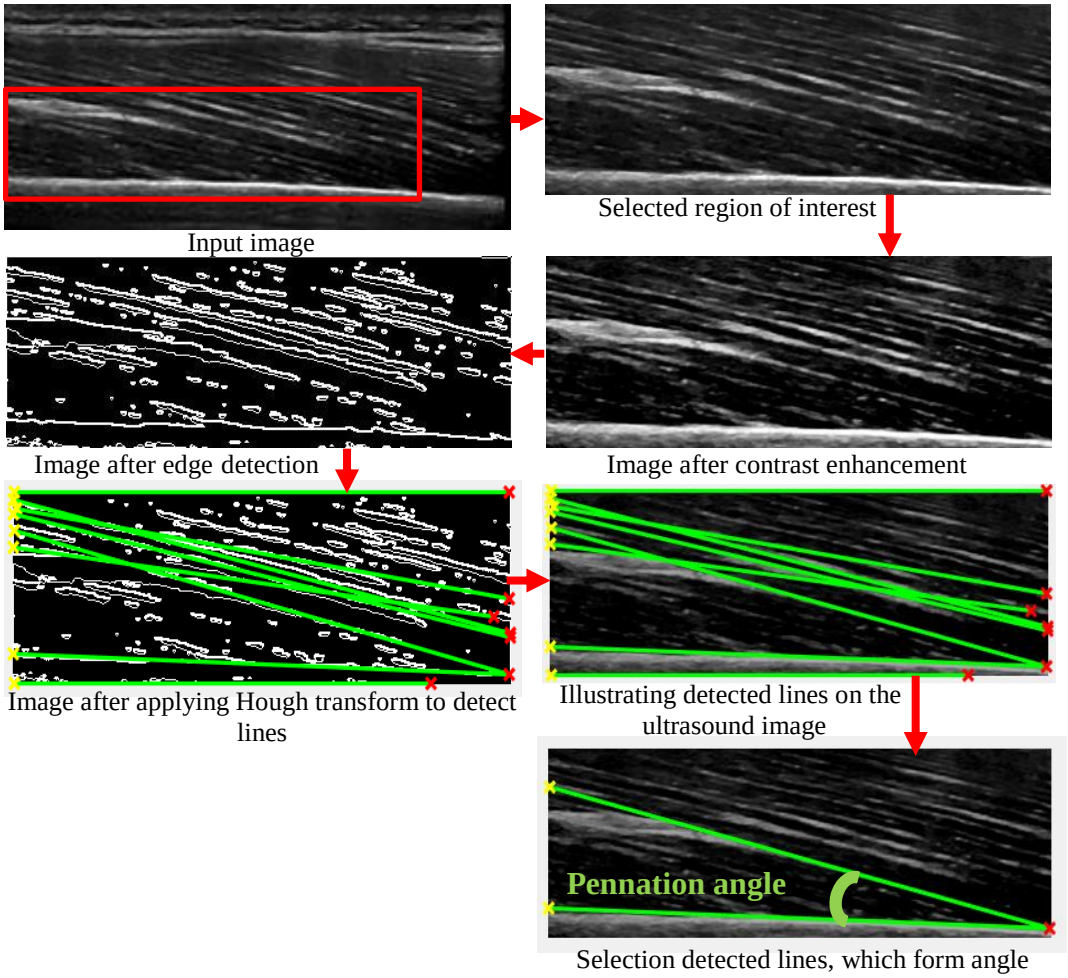

Figure (6-22) presents the steps of the pennation angle evaluation of the triceps muscle in one snapshot ultrasound image, the pennation angle is taken as the angle between the aponeurosis and the fibre direction.

From the above figure we can conclude that it is possible to evaluate the pennation angle of triceps muscle successfully by following the steps of the figure (6-21). However, due to limitations, which were mentioned previously in figure (6-12), it is difficult to measure pennation angle automatically, figure (6-23) and figure (6-24) below show that.

Input image

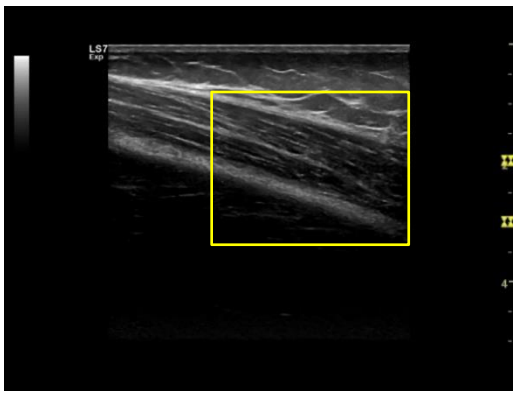

Image after cropping and applying all steps in the figure (93).

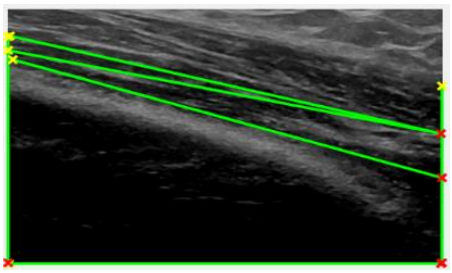

Figure (6-23) Detection lines in the image, which suffered from subcutaneous tissue layer on the upper aponeurosis of triceps muscle is shown in this figure.

Input image

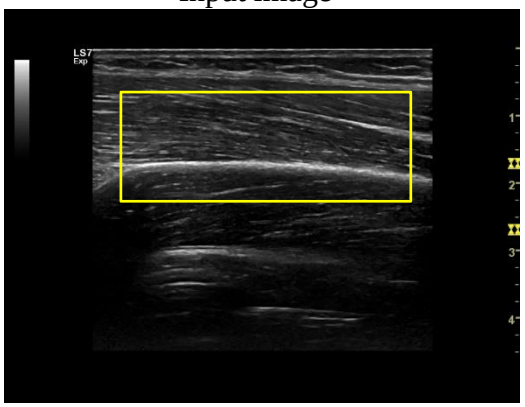

Image after cropping and applying all steps in the figure (93).

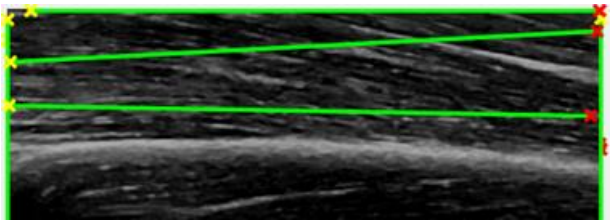

Figure (6-24) Detection lines in the image, which suffered from difficulties in defining the orientation of muscle fascicles is illustrated in this figure.

6.5.3.3 Comparing between manual and automatic measurements

Figure (6-25) shows the difference between manual and automatic estimation of pennation angle and this data is normally distributed. Through this depiction, the average of the difference between the two measurements was reported approximately at 1 degree; this is a good agreement between two the measurements. Furthermore, this figure illustrates a negative correlation as some values decrease and the other increases. However, only 10

samples were involved in this comparison. Therefore, in the future work, it is possible to increase the number of samples to get a sophisticated assessment of comparability.

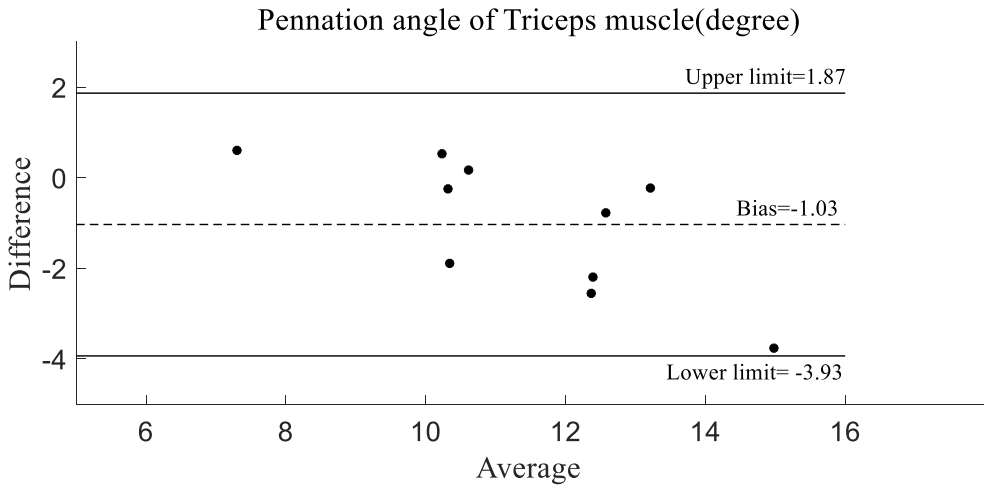

Figure (6-25) Bland-Altman plot of pennation angle measurement in degrees for 10 volunteers.

6.6 Discussion

Currently, the construction of musculoskeletal models depends on geometric musculoskeletal information, which has been collected from a cadaver, and this information is therefore not patient-specific and time-consuming to obtain (Asadi Nikooyan et al., 2011). The evaluation of the morphological parameters from volunteers based on the ultrasound imaging can support the development of a personal musculoskeletal model design. In this thesis, three experiments were proposed to evaluate some of these parameters of the upper extremity manually and automatically.

In the first experiment, 25 samples were involved in the manual and automated calculations (circumference and area of FPLT in cross-section). Regarding experiment 2, 25 samples were utilised in the manual measures, while 20 samples were used in the

automated measurement, due to the limitation, which was mentioned previously (presence of subcutaneous tissue). In the case of the experiment 3, the limitations are the poorly defined muscle fascicle orientation and the presence of subcutaneous tissue; therefore, only 10 samples were utilised in the manual and automatic measurements to evaluate pennation angle of the triceps muscle. There is this a certain minimum level of ultrasound image quality required before this method can be applied.

In three experiments, different pre-processing steps were employed to prepare image samples for the automatic evaluation stage. Experiment 1 and experiment 2 used the same steps (speckle noise reduction and image edge detection). The primary purpose of both experiments is detection of necessary information for evaluations; so, these steps are required to achieve this aim. In the case of experiment 3, there is a need to present and restore most details of the image, hence the pre-processing steps were: contrast enhancement and image edge detection. Since the determination of the pennation angle requires a precise definition of muscle fascicle orientation; therefore, these steps support the succinct objective of experiment 3.

The Bland-Altman plot demonstrated a good agreement between manual and automated methods in the three experiments except measuring circumference in experiment 1, which was larger than other measures. The scenarios of the circumference estimation in both directions has cumulative errors. Furthermore, estimation using manual methods was inherently prone to overestimation of the length. This is the reason for the significant difference between the two measurements.

6.7 Conclusions

The automatic evaluation for the morphological parameters of the upper extremities used in this chapter has satisfactory outcomes, which could open a new era for utilizing this technique in vivo. However, a larger sample-population is required to draw a realistic conclusion regarding the advantages and disadvantages of this procedure. In addition, it is possible to invest the proposed methods of three experiments in the lower extremity such as measurement of the cross-sectional area of the Achilles tendon and thickness and pennation angle of the gastrocnemius muscle.

Although developed methods in this thesis were used successfully to evaluate muscle thickness and pennation angle in the upper limb, it is still a limited number of ultrasound image samples. This is due to some limitations such as an anatomical variation, muscle status and the presence of subcutaneous adipose layer above upper aponeurosis of the muscle. However, a question would be raised: is it possible to design a more sophisticated artificial intelligent approach to learn to discriminate and detect adipose tissue then can evaluate these geometric parameters?

Artificial intelligence has an ability to solve problems. So, artificial intelligence could add new possibilities to evaluate these parameters by developing new methods to detect the complex structure of the musculoskeletal tissue. Examples of these methods are training convolutional neural networks to differentiate adipose tissue from other tissue and fuzzy image processing techniques which can be used to represent and analyse a complex pattern texture of musculoskeletal ultrasound images.

Chapter Seven
General Discussion

Chapter 7 General discussion

7.1 Summary of the main findings

The initial aim of this project was to develop new methods to automate the estimation of morphological parameters of the muscles and tendons of the upper extremity in vivo using ultrasound imaging. However, the presence of speckle noise and low image contrast are the main limitations of ultrasound images and affect quality in a negative way. Therefore, improving the quality of the musculoskeletal ultrasound image is a prerequisite. Identification of the required muscles or tendons details is fundamental to evaluate the geometric parameters. This can be extracted using edge detection method for musculoskeletal ultrasound imaging. Therefore, in this thesis, a new method for edge detection has been developed and tested on musculoskeletal ultrasound images and is a pre-processing step before musculoskeletal ultrasound image analysis. Finally, in this thesis, automated evaluation based on our new developed methods showed a good agreement with manual measurements.

The results of the speckle noise reduction methods showed the superiority of the anisotropic diffusion filter over local adaptive median filter in minimising speckle noise in the MUI. Therefore, anisotropic diffusion filter was selected to employ speckle noise reduction in this thesis.

The thesis developed local fuzzy contrast image enhancement as a new method to enhance the contrast of the musculoskeletal ultrasound image. Local fuzzy contrast enhancement method performed well when applied to a single image such as traditional one snapshot image and panoramic image. However, the contrast was not improved in all frames of an ultrasound video scan compared with a global fuzzy contrast enhancement method. The

reasons behind this is related to the nature of video recording as it could impose several obstacles such as the operator's ability to control the moving probe over the skin surface within a scanned surface. The other major outcome in this study was related to the findings of fuzzy edge detection method of the musculoskeletal ultrasound images. The novelty of this technique was linked to the ability of minimising the picture's artifacts by selection of the substantial edge details and reject unnecessary other details. The net result was a successful mapping of all the boundaries of an ultrasound picture.

An alternative CNN approach to edge detection of the MUI was explored and applied for edge detection of the musculoskeletal ultrasound image and two kinds of ground truth images (expert ground truth and Canny ground truth images) were used in the edge detection application. The results emphasised that a preferable visualisation of the ultrasound picture's boundaries was achieved when using an expert ground truth image compared to that of Canny ground truth image.

The results of this thesis indicated the ability to identify some of the geometric parameters automatically, and the automated methods were compared to the manual measurements.

The cross-sectional area and circumference of flexor pollicis longuis tendon, thickness and pennation angle of triceps muscle are the primary assessed parameters. Furthermore, Bland-Altman plot method demonstrated a substantial agreement between the manual and automated methods during measurement of the cross-sectional area of flexor pollicis longuis tendon, thickness and pennation angle of triceps muscle except measuring the circumference of flexor pollicis longuis tendon. The significant difference between the two measurements during circumference estimation was related to the recorded accumulative errors during the

procedures. This is because the manual measurement of the circumference was evaluated by gathering small straight distances around the cross section of the tendon.

All in all, the outcomes of this thesis answered research questions of this dissertation, which are the following:

1- How can the quality of the ultrasound image be improved?
2- How can musculoskeletal parameters be extracted automatically?
3- How well do automatic measurements of musculoskeletal parameters compare to manual measurements?

These research questions were being addressed when carrying out novel methods, which were developed in this work. Moreover, the outcomes of this thesis had important implication in supporting future design of personalised musculoskeletal models and further research in this field.

7.2 Discussion of the dissertation results in relation to current articles

The source of the results of this thesis comes from different stages: enhancement (speckle noise reduction and enhancement of image contrast), image edge detection (using CNN, Fuzzy edge detection method) and analysis (such as measurement of thickness and pennation angle of triceps muscle). Moreover, ultrasound image data was collected from the same ultrasound machine without any further calibration to avoid any bias in the samples' results.

Regarding speckle noise reduction of musculoskeletal ultrasound images, two filters were used. The first filter was the local adaptive median filter that was performed on the SAR image at a different window size (3x3, 5x5 and 7x7) (Qiu, 2004). In this thesis, the local adaptive median filter was applied to reduce speckle noise in the musculoskeletal ultrasound images and with expanding window size (9x9 and 11x11). In both applications (SAR image

and musculoskeletal ultrasound images), the window size (3x3) illustrated a higher quality of speckle noise reduction compared with other window sizes. This result agrees with Qiu, (2004). The second filter was an anisotropic diffusion filter, the relative advantages of this filter resides in reducing speckle noise while at the same time working to keep the important parts of the image such as edges and texture. Therefore, this filter is a suitable choice for medical image applications. Anisotropic diffusion filter was applied successfully in several ultrasound applications such as kidney and heart ultrasound images (Abd-Elmoniem et al., 2002) and liver ultrasound image (Krissian et al., 2007). Recent application of the musculoskeletal ultrasound image (collected from shoulder region) was introduced by Gupta et al. (2014). In this thesis, anisotropic diffusion filter and local adaptive median filter were applied to the musculoskeletal ultrasound images, which were collected from the shoulder region of a cadaver and the arm region of healthy participants. The performance of anisotropic diffusion filter outperforms local adaptive median filter performance in speckle noise reduction of the MUI. Therefore, anisotropic diffusion filter was selected in the thesis as pre-processing step in some applications such as evaluation of muscle thickness.

Concerning the contrast enhancement of the musculoskeletal ultrasound images, a novel method was developed and tested in this thesis. This method is based on fuzzy inference system and addresses the low contrast of the image locally. However, more than one method was introduced to improve the contrast quality in the image and depending primarily on fuzzy techniques. The first method involving fuzzy technique, which modified the fuzzy membership function to improve the image contrast in the fuzzy domain. This method was applied in other biomedical applications such as medical x-ray images (Tizhoosh et al., 1997) and breast ultrasound images (Guo et al., 2006), but it has not been applied to the musculoskeletal ultrasound images. The second method is Intuitionistic Fuzzy Sets (IFS),

which was implemented on a mammogram images (Deng et al., 2016) and MRI images (Deng et al., 2016), but it has not been recruited to enhance musculoskeletal ultrasound images. Due to complex texture patterns of MUI, it is difficult to define the significant details of the ultrasound images and make a threshold. The IFS method requires a pre-processing step such as a thresholding process, so this adds a challenge in performing intuitionistic fuzzy method on MUI, whereas local fuzzy contrast method does not require this step. Furthermore, both methods : Intuitionistic Fuzzy Sets and modification technique of fuzzy membership function were performed globally. Hence, a local method with prior knowledge of contrast enhancement analysis has been presented to overcome the effects of low contrast at the selected region.

The concept of edge detection method was carried out in this thesis using Convolutional Neural Network (CNN) and fuzzy edge detection methods. The idea of using CNN in this thesis is derived from (Ciresan et al. 2012), which was one of the pioneers of using CNN in medical image applications. In this study, CNN was used to detect biopsy pixels within the membrane or not. Ciresan's work made extensive use of graphics processing units (GPUs) in the training of their CNNs. GPU has a significant role in the acceleration of deep neural network training (Ciresan et al. 2013), but no special GPU architecture is required once the CNNs have been trained. In 2013, this scenario of pixel classification was also applied to detect mitosis in breast cancer images; features that were fed to the classifier came from a fusion of CNN features and handcrafted features (Wang et al. 2014). CNNs have also been applied to X-ray image processing applications. Here, CNNs have been used to detect bone (Yang et al., 2016). Recently, segmentation of musculoskeletal ultrasound images has been introduced as another application of using CNNs (Cunningham et al.,2017). This shows that CNNs are finding increasing use in biomedical image processing applications. CNN in this

thesis was recruited to identify whether the pixel of musculoskeletal ultrasound images is edge or non-edge. This image was a panoramic ultrasound image, which was collected from a cadaver (shoulder region). Ultrasound scanning of cadaveric material is beneficial in understanding the internal structure of the musculoskeletal system and drawing ground truth images, as estimates can be checked by dissection. However, there are several limitations experienced during the procedure of CNN implementation compared with other articles in the literature. Firstly, a limited set of training data involved only one image for training and selected 8000 pixels (3000 edge pixels and 5000 non-edge pixels). The main reason for using only one image is the lack of available data and the rate of superiority of CNN performance with limited training data sets. Compared with other work for example, Ciresan et al. (2012), who used 30 biopsy images with dimensions (512x512) in the training dataset. Another application recruited 404 cases (404 x-ray images) for training CNN (Yang et al., 2016). The recent implementation of the musculoskeletal ultrasound image was introduced by Cunningham et al. (2017), which involved 9,187,904 trainable weights for detecting the orientation of muscle fibres of the medial gastrocnemius muscle. Secondly, it is possible that the results might have been affected by the difference in the pattern of the texture characteristic between medical images and a musculoskeletal ultrasound image. Furthermore, CNN did not apply to the healthy samples due to insufficient time to increase the number of collected data and expand a set of training data.

A novel fuzzy edge detection technique was introduced to perform edge detection of the musculoskeletal ultrasound image. It was applied to the ultrasound image, which describes the cross-section of flexor pollicis longus tendons in one snapshot. Furthermore, it was used in single view of the ultrasound image of the triceps muscle to isolate upper and lower aponeuroses. This method is based on a fuzzy inference system that relies on the construction

membership function and fuzzy rules. Fuzzy membership function parameters were selected according to a standard deviation analysis, which was a newly introduced during this thesis. The essential part of this technique was fuzzy rules, which detect the edge pixel of the image from the surrounding pixels.

Moreover, evaluating geometric parameters concentrated on details such as muscle thickness evaluation which requires focus on the extraction of upper and lower muscle aponeuroses and rejection of extraneous information. Referring to other related literature studies, traditional methods (Canny operator, Sobel operator and Prewitt operator) (Canny, 1986), fuzzy image techniques (Gonzalez et al., 2014; Gonz et al., 2016) and CNN illustrate all the details of edge pixels in one image. However, the main limitation of these studies as mentioned above was the possibility of inheriting a bias during the result's evaluation due to the presence of artifacts, see figure (5-31). Example of this artifact is speckle information due to complex feature texture of MUI. However, fuzzy edge detection method was developed in this thesis to separate MUI into different levels of information, so is it possible to get important details in one level such as object's boundaries and reject other details such as speckle information in other level.

There is a relatively small body of literature dealing with the automatic evaluation of the muscle thickness. This was applied to an extensive data set of ultrasound images, which were collected from the lower limb muscle (Han et al., 2013; Caresio et al., 2016). While the proposed method in this thesis was employed on a smaller data population (20 image samples). With the same aim, Han et al. (2013) used Hough transform method after enhancement to extract the deep and superficial aponeuroses of the medial gastrocnemius muscle. However, the resulting images would include aponeuroses details and other details such as muscle fascicles. Therefore, this would raise the mean difference between manual

and automatic measurements; the mean difference was approximately 1.45 mm. Whereas Caresio et al. (2016), followed the same steps of Han et al. (2013), but unnecessary information (muscle fascicles) was avoided using a binary mask, and the mean difference of the medial gastrocnemius muscle was 0.45 mm. On the other hand, in this thesis, fuzzy image edge detection and active contour-based segmentation were utilised to extract upper and lower aponeuroses without additional information (muscle fascicle). The mean differences between the automatic and manual measurements were smaller than the previous studies and were reported at 0.115 mm.

In the last decade, much of the published studies have been concerned with the determination of the muscle pennation angle. One of these studies was introduced by Zhou et al. (2015) and was carried out on the gastrocnemius muscle in the lower limb. The employed method in this thesis followed the same steps of Zhou, but the traditional method of the image edge detection (Canny operator) was replaced by fuzzy edge detection method. Moreover, the proposed local contrast enhancement method was added to the steps of the pennation angle evaluation to strengthen the results. Another study was presented by Jalborg (2016). This study used a random transform method to detect the orientation of muscle fibres and lower aponeurosis instead of the Hough transform method. The researcher measured the pennation angle of the gastrocnemius muscle but did not compare manual and automatic measurements. The performance of Hough and random transform are very close, except the Hough transform method needs a pre-processing step (edge detection). Furthermore, the Hough transform method is quicker and less complicated than random transform methods. However, in this thesis, we introduced a novel method of edge detection using fuzzy inference system. Therefore, it is possible to avoid the limitation of the Hough transform method and use it for line detection.

There is a relative lack of studies focusing specifically on the evaluation of the cross-section area of tendons and muscles. Recently, Toktas et al. (2016), presented a manual method for evaluation of the cross-sectional area of flexor policies longus tendon based on the ultrasound images of healthy patients and those with Parkinson's disease patients. Furthermore, another experiment was presented (Baño-aledo et al., 2017) to measure thickness of different tendons in the lower limb (Achilles and patellar tendons). In this experiment, tendons were measured by the same expert several times and by different experts to evaluate the agreement of these measurements. These evaluations were achieved manually. If these measurements were evaluated automatically based on analysis of image properties, it could illustrate the difference in the reality more clearly. Automatic evaluation of the cross-section area presented in this thesis is one of the first investigations to try to automate this process. The results demonstrate a small mean difference between the automatic and manual measurements; it is approximately 1 mm^2.

All in all, the proposed techniques that are presented and described in this thesis could pave the way for future study of automatic measurement of the other skeletal muscles and other geometric parameters such as length of muscle fascicle, tendon length and muscle length.

7.3 Limitations

Since the primary aim of this thesis is the development of new methods across the whole image processing pipeline to allow automatic evaluation of musculoskeletal parameters. Therefore, all available time was spent on this purpose and it was extremely challenging to collect a large set of data in limited time. Moreover, the complex structure of musculoskeletal system requires an expert to interpret patterns of MUI and differentiate between musculoskeletal components. The large set of data is necessary to train CNN and get good

results, but absence of large set of data adds additional constraints of using CNN in the edge detection method of musculoskeletal ultrasound images. As CNN is craving to have a massive set of training data, using CNN technique would have been more useful if it had more trained data. Therefore, the small set of musculoskeletal ultrasound images which were acquired from healthy subjects are insufficient to realise the potential of a CNN. Furthermore, increasing the number of the image samples works to raise the statistical power of the results from all proposal approaches and makes the analysis more representative. Sufficient sample data could also support manual and automatic comparison.

The second limitation is related to the facility of equipment such as the ultrasound machine. Data was acquired with one snapshot; this view only showed limited information because this machine did not include the advanced technique (panoramic technique), but, it is possible to exploit technology in the clinic to collect data, if it is readily available. This is useful to use panoramic technique when measuring a whole muscle fascicle or whole tendon length, because a panoramic technique through a set of frames offers better clarification of musculoskeletal system details in one image. In this thesis, it is possible to collect a set of ultrasound image frames to visualise a whole muscle using ultrasound video scanning. Ultrasound video has more variation than panoramic image because it is difficult to control on the probe through video scanning. However, more practice courses of using ultrasound machine helps to reduce this variation and get a proper scanned ultrasound video.

Presence of a subcutaneous tissue layer above upper aponeurosis of the overweight participants can change the shape and size of the muscle, see figure (6-12). This add another limitation for the manual and automatic measurements, see experiment 2, section 6.5.2 and experiment 3, section 6.5.3.

Chapter Eight
Conclusions and Future work

Chapter 8 Conclusions and Future work

8.1 Conclusions

The outcome of this dissertation highlighted the ability of measuring the geometric parameters of the upper extremities in healthy volunteers using ultrasound imaging and developed automated techniques.

New methods were developed to assist in the analysis of the musculoskeletal ultrasound imaging such as the local fuzzy contrast image enhancement and fuzzy edge detection method. The algorithm for both methods depends on the fuzzy inference technique, which includes constructing a set of fuzzy rules, which reflect the knowledge of problem representation and solution. On the other hand, local adaptive median filter and the CNN method were applied for the first time on the musculoskeletal ultrasound images. Furthermore, Hough transform method and active contour-based segmentation were utilised to assist the final steps of the musculoskeletal ultrasound analysis to extract musculoskeletal parameters. These developed and applied methods were tested successfully on musculoskeletal ultrasound images that were collected from cadaver and healthy participants.

The main results of the thesis can be summarized as follows: this project compared the efficacy of two filters in reducing speckle noise of the musculoskeletal ultrasound images and concluded that an ADF filter offered a high-quality performance over the LAMF in speckle noise reduction. Minimizing the impact of the speckle noise in the musculoskeletal ultrasound images was involved as the pre-processing step in some applications during this dissertation. The study stated the capability to enhance the contrast of offline musculoskeletal ultrasound video using the local fuzzy contrast enhancement method.

However, not all the video frames were enhanced due to the high level of variation which could occur through ultrasound video scanning of muscle and tendons. The findings of this dissertation highlighted the significant advantage of using fuzzy edge detection to get different levels of edge details of musculoskeletal ultrasound images. It is therefore possible to choose the level of information, which is necessary for musculoskeletal parameters extraction. In addition, the use of this edge detection application in CNN is promising, but a large sample-population is required to train CNN in contrast with the fuzzy edge detection method.

To sum up, the results of these methods are novel and could open a new era to evaluate other morphological parameters of the upper extremity in vivo automatically. This will support the design of subject-specific models and prosthetic design. In addition, it would work as preliminary step for further research in the evaluation of the muscle fibre length and the automated construction of the 3D musculoskeletal ultrasound images.

8.2 Future work

Further data collection will help in raising the applicability of the developed methods in this thesis; therefore, it would be desirable to expand the range of data collection as future work. Further proposals include collecting ultrasound images using different protocols from other parts of the upper and lower extremities. Moreover, it is beneficial to collect musculoskeletal ultrasound images using a panoramic technique from healthy volunteers not only from cadaver and apply these methods on it. Obtaining a large data set of the ultrasound images offers abundant room for further progress of using CNN in edge detection application of the musculoskeletal ultrasound images, because it will expand the data set of the training.

To obtain a full picture of the developed methods in this thesis (local fuzzy contrast enhancement and fuzzy edge detection method), they need to be applied on the other biomedical images such as biopsy image, MRI and CT scanning images because these images have different properties. In addition, it is useful, if they are applied on the other musculoskeletal ultrasound images, which will be collected from lower limb for example, ultrasound image of Achilles tendons and gastrocnemius muscles.

Also, this thesis has thrown up some questions in need of further investigation:

Q1: Is it possible to evaluate a long muscle fascicle length automatically?

It is difficult to scan a whole tendon whether is short or long in one snapshot or one view, this means, in one view can scan a part of the tendon. Therefore, as future proposal, there are two ways to answer this question and this depends on the way of collecting musculoskeletal ultrasound imaging:

1-If collected data is musculoskeletal ultrasound video, the muscle fascicle length could be evaluated by combining two techniques: fuzzy entropy and optical flow method. Fuzzy entropy is involved in detecting the candidate pixel in each frame, while optical flow method is utilized for tracking muscle fascicle and measuring the length.

2-In the case of collecting data using a panoramic technique, can use methods that have been developed in this thesis to determine the length of the muscle fascicles. Achieving this purpose involves the following steps (image contrast enhancement, fuzzy edge detection of the image and using Hough transform method for detection muscle fascicle and measuring its length).

Q2: Can the performance of speckle noise reduction in the musculoskeletal ultrasound imaging be improved?

In this thesis, there is a competitive performance between Local Adaptive Median Filter (LAMF) and Anisotropic Diffusion Filter (ADF). ADF outperforms LAMF in speckle noise reduction, while LAMF has a high score in preserving edges of the ultrasound images. A future work is to improve the performance of speckle noise reduction, it is possible to combine both filters. This will help in raising the score of speckle noise reduction and at the same time keep the important details of the image content.

References

Abd-Elmoniem, K.Z., Youssef, A.B.M. and Kadah, Y.M. (2002). Real-Time Speckle Reduction and Coherence Enhancement in Ultrasound Imaging via Nonlinear Anisotropic Diffusion. *IEEE Transactions on Biomedical Engineering.* 49(9), 997–1014.

Abrahams, M. (1967). Mechanical behaviour of tendon. *Medical & biological .Engineering* 5,433-443.

Ackland D.C., Pandy M.G. (2009) Lines of action and stabilizing potential of the shoulder musculature. *Journal of Anatomy* 215(2):184–197.

Agaian, S.S., Panetta, K. and Grigoryan, A.M. (2000). A new measure of image enhancement. *Presented at International. Conference. Signal Processing Communication, Marbella, Spain*, Sep. 19–22.

Agaian, S.S., Panetta, K. and Grigoryan, A.M. (2001). Transform-Based Image Enhancement Algorithms with Performance Measure. *IEEE Trans. Image Processing.* 10(3), 367–382.

Agaian, S.S., Silver, B. and Panetta, K. (2007). Transform Coefficient Histogram-Based Image Enhancement Algorithms Using Contrast Entropy. *IEEE Trans. Image Processing.* 16(3):741-758.

Ahmed, R. and Nazarian, L. N. (2010). Overview of Musculoskeletal Sonography. *Ultrasound Quarterly*, 26(1), 27–35.

Ai, T., Morelli, J. N., Hu, X., Hao, D., Goerner, F. L., Ager, B. and Runge, V.M. (2012).A historical overview of Magnetic Resonance Imaging focusing on technological innovations. *Investigative Radiology*. 47(12),725-741.

Aja-Fernandez, S. and Alberola-Lopez, C. (2006). On the estimation of the coefficient of variation for anisotropic diffusion speckle filtering. *IEEE Transaction in image processing*. 15(9), 2694-2701.

Amis, A.A., Dowson, D. and Wright, V. (1979). Muscle strengths and musculoskeletal geometry of the upper limb. *Engineering in Medicine*. 8 (1), 41-48.

Arnet, U., van Drongelen, S., van der Woude, L.H.V, Veeger, D.H.E.J. (2012) Shoulder load during handcycling at different incline and speed conditions. *Clinical Biomechanics* 27(1):1–6

Arnold, A. S., Ph, D., Salinas, S., Asakawa, D. J. and Delp, S. L. (2000). Accuracy of Muscle Moment Arms Estimated from MRI-Based Musculoskeletal Models of the Lower Extremity. *Computer Aided Surgery*. 5, 108–119.

Arnold, E. M., Ward, S. R., Lieber, R. L. and Delp, S. L. (2010). A model of the lower limb for analysis of human movement. *Annals of Biomedical Engineering*. 38(2), 269–79.

Asadi Nikooyan, A.,Veeger, H.E.J., Chadwick, E.K.J., Praagman, M., and Van Der Helm, F.C.T. (2011). Development of a comprehensive musculoskeletal model of the shoulder and elbow. *Medical. Biological. Engineering. Computing.* 49(12), 1425–1435.

Asakawa, D. S., George, P. and Blemker, S. S. (2003). Cine Phase-Contrast Magnetic Resonance Imaging as a Tool for Quantification of Skeletal Muscle Motion. *Seminars in Musculoskeletal Radiology*. *7*(4), 287–296.

Baikoussis, N. G., Apostolakis, E., Papakonstantinou, N. A., Sarantitis, I., & Dougenis, D. (2011). Safety of Magnetic Resonance Imaging in Patients with Implanted Cardiac Prostheses and Metallic. Annals of thoracic surgery. 91(6), 2006–2011.

Baño-aledo, M.E., Martínez-Payá, J.J., Ríos-Díaz, J., Mejías-Suárez, S., Serrano-Carmona, S. and Groot-Ferrando, A. (2017). Ultrasound measures of tendon thickness: Intra-rater , Inter-rater and Inter-machine reliability. *Muscles, Ligaments and Tendons Journal* 7(1), 192–199.

Bama, S. & Selvathi, D. (2014). Despeckling of medical ultrasound kidney images in the curvelet domain using diffusion filtering and MAP estimation. *Signal Processing*. 103, 230–241. Available at: http://dx.doi.org/10.1016/j.sigpro.2013.12.020.

Bengio, Y. (2009). Learning deep architectures for AI. *Foundations and Trends in Machine Learning*. 2(1), 1-127.

Bey, M. J. and Derwin, K. (2012). Measurement of in vivo tendon function. *Journal of Shoulder and Elbow Surgery*. 21(2), 149–57.

Bignotti, B., Cadoni, A., Martinoli, C. and Tagliafico, A. (2014). Imaging of skeletal muscle in vitamin D deficiency. World. *Journal of Radiology*. 6(4),119-124.

Binaee, K., and Hasanzadeh, R. P. R. (2014). An ultrasound image enhancement method using local gradient based fuzzy similarity. *Biomedical Signal Processing and Control*. *13*, 89–101. doi: 10.1016/j.bspc.2014.03.013.

Biradar, N., Dewal, M. L. and Rohit, M. K. (2014). Edge Preserved Speckle Noise Reduction Using Integrated Fuzzy Filters. *International Scholarly Research Notices*, 1–11. doi:10.1155/2014/876434.

Blana, D., Chadwick, E.K., Van Der Bogert, A.J.and Murray, W.M. (2017). Real-time simulation of hand motion for prosthesis control. *Computer Methods in Biomechanics and Biomedical Engineering*. 20(5), 540–549.

Bland, J.M. and Altman, D.G. (1986). Statistical methods for assessing agreement between two methods of clinical measurement, *Lancet and Biochemical clinical*, 307–310.

Blemker, S. S., Asakawa, D. S., Gold, G. E. and Delp, S. L. (2007). Image-based musculoskeletal modelling: applications, advances, and future opportunities. *Journal of Magnetic Resonance Imaging: JMRI*. *25*(2), 441–51.

Blum, T., Heining, S. M., Kutter, O. and Navab, N. (2009). Advanced training methods using an Augmented Reality ultrasound simulator. *8th IEEE International Symposium on Mixed and Augmented Reality*, 177–178.

Bolsterlee, B., Veeger, D., H., E., J., Chadwick, E., K.(2013).Clinical applications of musculoskeletal modelling for the shoulder and upper limb. *International Federation for Medical and Biological Engineering*, 51(9),953-963.

Brand, P.W., Beachm, R.B. and Thompson, D.E. (1981). Relative tension and potential excursion of muscles in the forearm and hand. *Journal of Hand Surgery American*. 6, 209–219.

Brorsson, S., Nilsdotter, A., Hilliges, M., Sollerman, C. and Aurell, Y. (2008). Ultrasound evaluation in combination with finger extension force measurements of the forearm musculus extensor digitorum communes in healthy subjects. *BioMed Central*. 10, 1–10.

Canny, J., 1986. A Computational Approach to Edge Detection. *IEEE Transaction on Pattern Analysis and Machine Intelligence.* 8(6), 679–698.

Caresio, C., Salvi, M., Molinari, F., Meiburger, K.M. and Minetto, A.M. (2017). Fully Automated Muscle Ultrasound Analysis (MUSA): Robust and Accurate Muscle Thickness Measurement. *Ultrasound in Medicine and Biology*. 43(1), 195–205.

Casciola-Rosen, L., Nagaraju, K., Plotz, P., Wang, K., Levine, S., Gabrielson, E., Corse, A. and Rosen, A. (2005). Enhanced autoantigen expression in regenerating muscle cells in idiopathic inflammatory myopathy. *The Journal of Experimental Medicine*. 201(4), 591–601.

Cernazanu-glavan, C. and Holban, S. (2013). Segmentation of bone structure in X-ray images using convolutional neural network. *Advances in Electrical and Computer Engineering*. 10(1), 1-8.

Chadwick, E.K., Blana, D., Kirsch, R.F. and Van Der Bogert, A.J. (2014). Real-time simulation of three-dimensional shoulder girdle and arm dynamics. *IEEE Transactions on Biomedical Engineering*, 61(7), 1947–1956.

Chan, T. and Vese, L. (2001). Active Contours Without Edges. *IEEE Transaction Image. Processing*. 10(2), 266–277.

Chan, V. and Perlas, A. (2011). Basics of Ultrasound Imaging. In Atlas of ultrasound guided procedures in international pain management. 13–20.

Charlton, I.W.and Johnson, G.R. (2006) A model for the prediction of the forces at the glenohumeral joint. *Proc Inst Mech Eng*. 220(8), 801–812.

Chaudhary, H. and Aneja, S. (2012). MRI Evaluation of Shoulder Joint: Normal Anatomy and Pathological Finding a Pictorial Essay and Review. *Journal of Dental and Medical Sciences*. 2(2), 1–9.

Chaudhry, A., Hassan, M., Khan, A. and Kim, J.Y. (2013). Automatic active contour-based segmentation and classification of carotid artery ultrasound images. *Journal of Digital Imaging*. 26(6), 1071–1081.

Chauhan, B., Hamzeh, M. A. and Cuesta-vargas, A. I. (2013). Prediction of muscular architecture of the rectus femoris and vastus lateralis from EMG during isometric contractions in soccer players. *Springer Plus 2*(1), 1-8. doi:10.1186/2193-1801-2-548.

Cheng, H. and Shi, X.J. (2004). A simple and effective histogram equalization approach to image enhancement. *Digital Signal Processing*, 14(2), 158–170.

Choudhury, A. and Medioni, G. (2012). A framework for robust online video contrast enhancement using modularity optimization. *IEEE Transactions on Circuits and Systems for Video Technology*. 22(9), 1266–1279.

Chunming, H., Huadong, G. and Changlin, W. (2002). Edge preservation evaluation of digital speckle filters. IGARSS 2002, IEEE Int. Geosocial. Remote Sensing Sump. 4, 2471–2473.

Ciresan, D., Giusti, A. and Gambardella, L.M. (2012). Deep Neural Networks Segment Neuronal Membranes in Electron Microscopy Images. *Neural Information Processing System conference*. 2852—2860.

Ciresan, D., Giusti, A. and Gambardella, L.M. (2013). Mitosis Detection in Breast Cancer Histology Images with Deep Neural Networks. *Medical Image Computing and Computer-Assisted Intervention*. 2, 411-418.

Cook, T. S., Stein, J. M., Simonson, S. and Kim, W. (2011). Normal and variant anatomy of the shoulder on MRI. *Magnetic Resonance Imaging Clinics of North America*. 19(3), 581–94.

Cunningham, R., May, G. and Loram, I. (2017). Estimating Full Regional Skeletal Muscle Fibre Orientation from B-Mode Ultrasound Images Using Convolutional, Residual, and Deconvolutional Neural Networks. *Journal of Imaging*, 4(2), p.29. Available at: http://www.mdpi.com/2313-433X/4/2/29.

Dainty J. 1970. Some statistical properties of random speckle patterns in coherent and partially coherent illumination. *International Journal of Optics*. 17(10),.761–772.

Damadian, R. (1971). Tumour detection by nuclear magnetic resonance. *American association for the advancement of science*. 171, 1151-1153.

Damadian, R., Zaner, K. E. N., Hor, D. and Dimaiot, T. (1974). Human Tumours Detected by Nuclear Magnetic Resonance. *Proceeding of the. National. Academy. Science. USA*. 71(4), 1471–1473.

Deepa, B. and Sumithra, M. (2015). Comparative analysis of noise removal techniques in MRI brain images. 2015 *IEEE International Conference on Computational Intelligence and Computing Research (ICCIC)*

Dellepiane, S.G. and Angiati, E. (2014). Quality assessment of despeckled SAR images. *IEEE Journal of Selected Topics in Applied Earth Observations and Remote Sensing*. 7(2), 691–707.

Deng, G. (2011). A Generalized Unsharp Masking Algorithm. *IEEE Transactions on Image Processing*. 20(5), 1249–1261.

Deng, H., Deng, W., Sun, X., Liu, M., Ye, C. and Zhou, X. (2016a). Mammogram Enhancement using Intuitionistic Fuzzy Sets. *IEEE Transactions on Biomedical Engineering*. 64(8), 1803-1814.

Deng, H., Deng, W., Sun, X., Ye, C. and Zhou, X. (2016b). Adaptive Intuitionistic Fuzzy Enhancement of Brain Tumor MR Images. *Scientific Reports.*,1–14, DOI: 10.1038/srep357.

Doorn, J. (2014). Analysis of Deep Convolutional Neural Network Architectures," *21th Twente Student Conference on IT, University of Twente*, Netherlands.

Duda, R.O., and Hart., P.E. (1972). Use of the Hough transformation to detect lines and curves in pictures. *Communications of the ACM*. 15(1), 11–15.

Duenwald, S., Kobayashi, H., Frisch, K, Lakes,R. and Jr, R., V. (2011).Ultrasound echo is related to stress and strain in tendon. *Journal of biomechanics*, 44, 424-429.

Farbiz, F., Menhaj, M.B., Motamedi, S.A. and Hagan, M.T. (2000). A new fuzzy logic filter for image enhancement. *IEEE Transaction on Systems Man Cybernetics*. 30(1), 110–119.

Fischer, A. and Igel, C. (2012). An Introduction to Restricted Boltzmann Machines. *Frontiers in Neuroscience*, 7, pp.14–36.

Flower, K. A. B. and Chung, C. B. (2004). Normal MR imaging anatomy of the elbow. *Magnetic Resonance Imaging of north America*. 12, 191-206.

Frost, V.; Stiles, J.A.; Shanmugan, K.S. and Holtzman, J.C. A. (1982). Model for Radar Images and its Application to Adaptive Digital Filtering of Multiplicative Noise. *IEEE Trans. on Pattern Analysis and Machine Intelligence*. 4(2), 157-166.

Gallegos-funes, F. J., Jose, M., Rosales-silva, A. J. and Isakina, S. S. (2011). Real-Time Speckle and Impulsive Noise Suppression in 3-D Ultrasound Imaging. *Ultrasound Imaging*, ISBN: 978-953-307-239-5, http://www.intechopen.com

Gerus, P., Rao, G. and Berton, E. (2011). Short communication A method to characterize in vivo tendon force-strain relationship by combining ultrasonography, motion capture and loading rates. *Journal of Biomechanics*. 44(12), 1–4.

Giot, R., Bourqui, R., Journet, N and Vialard, A. (2015). Visual graph analysis for quality assessment of manually labelled documents image database. *2015 13th International Conference on Document Analysis and Recognition.* DOI: https://doi.org/10.1109/ICDAR.2015.7333938.

Gompels, B. A. and Darlington, L.G. (1981). Septic arthritis in rheumatoid disease causing bilateral shoulder dislocation: diagnosis and treatment assisted by grey scale ultrasonography. Annals of the Rheumatic diseases. *Annals of the Rheumatic Diseases*. 40, 609-611.

Gonzalez, R. C. and Woods, R. E. (2002). *Digital image processing*. 2nd edition. United State of America. Prentice Hall Inc.

Gopura, R. A. R. C., Kiguchi, K., and Horikawa, E. (2010). A Study on Human Upper-Limb Muscles Activities during Daily Upper-Limb Motions. *International Journal of Bio electromagnetism*. 12(2), 54–61.

Graf, R. (1980). The diagnosis of congenital hip joint dislocation by the ultrasonic compound treatment. *Archives of orthopaedic and traumatic surgery*. 97, 117-133.

Gravel, P., Beaudion, G. and De Guise, J. (2004). A method for modelling noise in medical images. *IEEE Transaction on Medical Imaging*. 23(10), 1221-1232

Grieg, G., Kubler, O., Kikinis, R. and Jolesz, F. A. (1992). Nonlinear Anisotropic Filtering of MRI Data. *IEEE Transactions on Medical Imaging*. 11(2), 221-232.

Guo, Y., Cheng, H., Huang, J., Tian, J., Litao, W. and Y. Su, Y. (2006). Breast Ultrasound Image Enhancement Using Fuzzy Logic. *Ultrasound in Medicine & Biology* 44(2), 297-514.

Gupta R., Elamvazuthi I., Chandra Dass S., Faye I., Vasant P., George J. and Izza F. (2014). Curvelet based automatic segmentation of supraspinatus tendon from ultrasound image: a focused assistive diagnostic method. *Biomedical Engineering Online*. http://www.biomedical-engineering-online.com/content/13/1/1.

Gupta R., Elamvazuthi I., Dass S., Faye I., Vasant P., George J., and Izzo F. (2014). Comparative Analysis of Anisotropic Diffusion and Non- Local Means on Ultrasound Images. *Journal of Machine to Machine Communications*. 1(1), 51–68.

Hagmann, P., Jonasson, L., Maeder, P., Thiran, J., Wedeen, V. J. and Meuli, R. (2006). Central nervous system: state of the art understanding Diffusion MR Imaging Techniques: From Scalar Imaging to Diffusion. *Radiographic*. 26, 205–224.

Hamill, J. and Knutzen, K. M. (1995). *Biomechanical basis of Human Movement*. Williams and Wilkins. Printed in United States of America.

Han, J., Yang, S. and Lee, B. (2011). A Novel 3-D Color Histogram Equalization Method with Uniform 1-D Gray Scale Histogram. *IEEE Transactions on Image Processing*. 20(2), 506–512.

Han, P., Chen, Y., Ao, L., Xie, G., Li, H., Wang, L. and Zhou, Y. (2013). Automatic thickness estimation for skeletal muscle in ultrasonography: evaluation of two enhancement methods. *Biomedical Engineering Online*. http://www.biomedical-engineering-online.com/content/12/1/6.

Haralick, R.M. and Sternberg, S.R. (1987). Image Analysis Morphology. *IEEE Transaction on Pattern Analysis and Machine Intelligence*. (4), 532–550.

Harm, S.and Muschler, G. (1986). Three-dimensional MR imaging of the knee using surface coils. *Journal of Computer assist tomography*. 10, 773-777.

Hashemi, R. H., Bradley, W. G. and Lisanti, C. J. (2010) *MRI the basics*.3rd edition, China, Wolters Kluwer, Lippincott Williams & Wilkins.

Health and Safety Executive, (2017). *Work- related Musculoskeletal Disorders (WRMSDs) Statistics in Great Britain 2017* Available at: http://www.hse.gov.uk/statistics/causdis/musculoskeletal/

Heemskerk, A. M., Sinha, T., K., Wilson, K., J., Ding, Z., Damon, B. M. (2009). Quantitative assessment of DTI-based muscle fibre tracking and optimal tracking parameters. *National Institute of Health*. 61(2), 467-472.

Heemskerk, A. M., Strijkers, G. J., Vilanova, A., Drost, M. R. and Nicolay, K. (2005). Determination of mouse skeletal muscle architecture using three-dimensional diffusion tensor imaging. *Magnetic Resonance in Medicine*. 53(6), 1333–40.

Heinz, N. (2016). Validity of two-dimensional ultrasound as a method of measurement of muscle and tendon parameters of the Infraspinatus", Master thesis in medical science, Keele university, UK.

Herbert, R. D. and Gandevia, S. C. (1995). Changes in pennation with joint angle and muscle torque: in vivo measurements in human brachialis muscle. *Journal of Physiology*. 484(2), 523–532.

Heron, C. W. (1992). Magnetic resonance imaging in rheumatology. *Annals of the Rheumatic Diseases*. 51, 1287–1291.

Hinton, G. E. (2007). Learning multiple layers of representation. *Trends in Cognitive Sciences*, 11(10), 428–34.

Hinton, G. E., Osindero, S. and Teh, Y.W. (2006). A fast learning algorithm for deep belief nets. *Neural Computation*. *18*(7), 1527–1554.

Hiremath, P.S., Tegnoor, J.R. (2014). Fuzzy inference system for follicle detection in ultrasound images of ovaries. *Soft Computing.* 18(7), 1353–1362.

Hodges, P. W., Pengel.Herbert, R. D., Gandevia, S. C. (2003). Measurement of muscle contraction with ultrasound imaging. *Muscle and Nerve*. 27,682–692.

Holzbaur, K.R.S., Delp, S.L. and Murray, W.M. (2007). Moment-generating capacity of upper limb muscles in healthy adults. *Journal of Biomechanics*. 40(11), 2442–2449.

Holzbaur, K.R.S., Murray, W.M. and Delp, S.L. (2005). A model of the upper extremity for simulating musculoskeletal surgery and analysing neuromuscular control. *Annals of Biomedical Engineering*. 33(6),.829-840.

Hough, P.V.C. (1962). Method and means for recognizing complex patterns, U.S. Patent 3,069,654.

Huynh-Thu, Q., Garcia, M., Speranza, F., Corriveau, P., and Raake, A. (2010). Study of Rating Scales for Subjective Quality Assessment of High-Definition Video. *IEEE Transactions on Broadcasting*, 57(1), 2010.

Ibrahim, A. M. (2004). *Fuzzy logic for embedded systems applications*, Elsevier Science, USA.

Ihnatsenka, B. and Boezaart, A. P. (2010). Ultrasound: Basic understanding and learning the language. *International Journal of Shoulder Surgery*. 4(3), 55–62.

Infantolino, B. W., Gales, D. J., Winter, S. L. and Challis, J. H. (2007). The validity of ultrasound estimation of muscle volumes. *Journal of Applied Biomechanics*. 23(3), 213–217.

Insana, M.F., Wagner, R.F., Garra, B. S, Brown, D.G. and Shawker, T. H. (1986). Analysis of ultrasound image texture via generalized Rician statistics. *Optical Engineering* 25, 743-748.

Jabbar S.I., Day C.R., Heinz N. and Chadwick E.K. (2016). Using Convolutional Neural Network for edge detection in musculoskeletal ultrasound images. *2016 IEEE International Joint Conference on Neural Networks (IJCNN)*, Vancouver, BC, 4619-4626.

Jalborg F.E. (2016). Automatic detection of skeletal muscle architecture features, *Master thesis, University of Oslo*.

Joshi, N. S., Choubey, N. S.and Dwivedi, R. (2013). Overview of Edge Detection Techniques. *American Journal of Computer Science & Information Technology*. 1, 20–32.

Kane, D., Grassi,W., Sturrock, R. and Balint, P.V. (2004). A brief history of musculoskeletal ultrasound: 'From bats and ships to babies and hips'. *Rheumatology*. 43, 931-933.

Kaplan, L. J., Potter, H. G. (2004).MR imaging of ligament injuries to the elbow. *Magnetic Resonance Imaging of north America*. 12, 221-232.

Kass M., Wikin.A. and Terzopoulos D. (1988). Snakes: Active Contour Models. *International Journal Computer Vision, Netherlands*. 321–331.

Kaur, J. and Gupta, P. (2012). Fuzzy Logic Based Adaptive Noise Filter for Real Time Image Processing Applications. *International Journal Computer Science Issues*. 9(4), 269–271.

Kim, M. and Chung, M. (2008). Recursively separated and weighted histogram equalization for brightness preservation and contrast enhancement. *IEEE Transactions on Consumer Electronics*. 54(3), 1389–1397.

Kontaxis, A. and Johnson, G.R. (2009). The biomechanics of reverse anatomy shoulder replacement - a modelling study. *Clinical Biomechanics*. 24 (3), 254-260.

Korstanje, J. H., Selles, R. W., Stam, H. J., Hovius, S. E. R., and Bosch, J. G. (2010). Development and validation of ultrasound speckle tracking to quantify tendon displacement. *Journal of Biomechanics*. 43(7), 1373–1379.

Kosbatwar, P. S. P. (2012). Pattern Association for character recognition by Back-Propagation algorithm using Neural Network approach. *International Journal of Computer Science & Engineering Survey 3*(1), 127–134.

Krell G, Tizhoosh HR, Lilienblum T, Moore CJ, Michaelis B. (1997). Fuzzy Image Enhancement and Associative Feature Matching in Radiotherapy. *Proceedings of International Conference on Neural Networks (ICNN'97).*

Kremkau, F. W. (2010). *Sonography principle and instruments*. 8th edition, China, Elsevier.

Krissian, K., Westin, C.F., Kikinis, R.and Vosburgh, K.G. (2007). Oriented Speckle Reducing Anisotropic Diffusion. *IEEE Transaction on Image Processing*. 16(5), 1412-1424.

Krizhevsky, A. and Hinton, G. (2012). ImageNet Classification with Deep Convolutional Neural Networks. *Advances in Neural Information Processing systems Conference*, 1097–1105.

Krueger, M., Delmas, P. and Gimel, G. (2008). On 3D Face Feature Segmentation Using Implicit Surface-Active Contours GAC on Implicit Surfaces. *23rd International Conference, Image and Vision Computing New Zealand, IEEE*.

Kuan, D.T.; Sawchuck, A.A.; Strand, T.C. and Chavel, P. (1987). Adaptive Restoration of Images with Speckle. *IEEE Transaction. on Acoustics Speech and Signal Processing*. 35(3), 373-383.

LaScalza, S. and Gallo, L.N. (2002). A Method for Measuring Euler Rotation Angles and Helical Axis of Upper Arm Motion. *Journal of Applied Biomechanics Inc.* 18, 374-383.

LeCun, Y., Bottou, L., Bengio, L. and Haffner, P. (1998). Gradient-Based learning applied to document recognition. *Proceedings of the IEEE*. *86*(11), 2278–2324.

Lee, J.S. (1980). Lee filter Digital image enhancement and noise filtering by using local statistics. *IEEE transactions on pattern analysis and machine intelligence*. 2(2), 165–168.

Lee, J.S., Jurkevich, I., Dewaele, P., Wambacq, P. and Oosterlinck, A. (1994). Speckle Filtering of Synthetic Aperture Radar Images: Review. *Remote Sensing Reviews*. 8,.313–340.

Lew, H. L., Chen, C. P. C.,Wang, T. G. Chew, K.T.L. (2007). Introduction to musculoskeletal diagnostic *Ultrasound. American Journal of Physical Medicine & Rehabilitation.* 86(4), 310-321.

Li, L., Tong, K., Y. (2005). Musculotendon parameters estimation by ultrasound measurement and geometric modelling: application on brachialis muscle. *Engineering in Medicine and Biology 27th Annual conference. China. IEEE.*

Lieber, R.L., Jacobson, M.D., Fazeli, B.M., Abrams, R.A. and Botte, M.J. (1992). Architecture of selected muscles of the arm and forearm - Anatomy and implications for tendon transfer. *Journal of Hand Surgery-American Volume* 17 (5), 787-798

Lieber, R., L. (2002). *Skeletal muscle structure function and plasticity*. 2nd edition, United State of America, Lippincott Williams & Wilkins.

Lin J., Fessell D., P., Jacobson J. A., Weadock, W.J. and Hayes C.W. (2000) An illustrated tutorial of musculoskeletal sonography: part1 introduction and general principle. *American Journal of Roentgenology*. 175, 637-645.

Locke, J., Baird, S. a, and Frankis, J. (2010). Preliminary observations of muscle fibre cross sectional area of flexor digitorum brevis in cadaver feet with and without claw toes. *Journal of Foot and Ankle Research*. *3*(1), 32.

Lopez-Molina, C., De Baets, B. and Bustince, H. (2013). Quantitative error measures for edge detection. *Pattern Recognition*. 46(4), 1125–1139.

Louis,L.J.(2008).Musculoskeletal ultrasound intervention: principles and advances *Radial Clin N Am*. 46, 515-533.

Maganaris, C. N., Baltzopoulos, V. and Sargeant, A. J. (1998). Changes in Achilles tendon moment arm from rest to maximum isometric plantar flexion: in vivo observations in man. *Journal of Physiology*. 510(3), 977–985.

Magermans, D.J., Chadwick, E.K.J., Veeger, H.E.J., Rozing, P.M.and Van der Helm, F.C.T. (2004). Effectiveness of tendon transfers for massive rotator cuff tears: a simulation study. *Clinical Biomechanics* 19 (2), 116- 122.

Makhsous, M., Hogfors, C., Siemien'ski A. and Peterson, B. (1999) Total shoulder and relative muscle strength in the scapular plane. *Journal of Biomechanics*. 32(11),1213–1220.

Mamdani, E.H. (1974). Application of fuzzy algorithms for control of simple dynamic plant. *Proceedings of the Institution of Electrical Engineers*. 121(12),1585.

Martin, D. C., Medri, M. K., Chow, R. S., Oxorn, V., Leekam, R. N., Agur, M. and McKee, N. H. (2001). Comparing human skeletal muscle architectural parameters of cadavers with in vivo ultrasonographic measurements. *Journal of Anatomy*. 199(4), 429–34.

Matthews, B. (2013). Comparison of the predicted and Observed secondary structure of T4 Phage Lysozyme. *Biochemical et Biophysical Acta*. 405, 442–451.

Mcqueen, F. M. (2000). Magnetic resonance imaging in early inflammatory arthritis: what is its role? *Rheumatology*. *39*, 700–706.

Melinscak, M., Prentasic, P. and Loncaric, S. (2015). Retinal Vessel Segmentation Using Deep Neural Networks. *10th International Conference on Computer Vision Theory and Applications*, 577-582.

Mori, S. and Zhang, J. (2006). Principles of diffusion tensor imaging and its applications to basic neuroscience research. *Neuron*. 51(5), 527–39.

Mozer, M. C. (1989). A Focused Backpropagation Algorithm for Temporal Pattern Recognition. *Complex Systems*. *3*, 349–381.

Muscolino, J. E. (2010). *The muscular system manual*. 3rd edition, China, Mosby Elsevier.

Michailovich, O. V & Tannenbaum, A. (2006). Despeckling of Medical Ultrasound Images. *IEEE Transactions on Ultrasonics, Ferroelectrics and Frequency Control transactions on Ultrasonics, ferroelectrics, and frequency control*. 53(1), 64–78.

Nachtegael, M., Weken, D.V., Kerre, E.E. (2010). *Fuzzy filters for image processing*. 1st edition, Springer-Verlag Berlin Heidelberg, Germany.

Nachtegeal M., Van der Weken D., Van De Ville D. and Kerre E. (2010). *Fuzzy Filters for Image Processing*. 1st edition Germany, Springer-Verlag Berlin Heidelberg.

Nair, M.S. and Lakshmanan, R. (2011). Fuzzy logic-based automatic contrast enhancement of satellite images of ocean. *Signal, Image and Video Processing*. *5*, 69– 80.

Naraghi, A. and White, L. M. (2012). Three-dimensional MRI of the Musculoskeletal System. *American Journal of Roentgenology*. 199, 283–293.

Narouze S.N. (2011). *Atlas of Ultrasound-Guided Procedures in Interventional Pain Management*. 1st edition USA, Springer.

Narici, M. (1999). Human skeletal muscle architecture studied in vivo by non-invasive imaging techniques: functional significance and applications. *Journal of Electromyography and Kinesiology*.9(2), 97–103.

Nercessian, S., Panetta, K. and Agaian, S. (2009). A non-reference measure for objective edge map evaluation. *Conference Proceedings - IEEE International Conference on Systems, Man and Cybernetics*, (October), 4563–4568.

Neumann, D.A. (2010). *Kinesiology of the musculoskeletal system*. 2nd edition. United State, Mosby Elsevier.

Nikooyan, A.A., Veeger, H., E., J., Chadwick, E., K., J., Pragman, M. and Ven Der Helm, F.C.T. (2011). Development of a comprehensive musculoskeletal model of the shoulder and elbow. *Medical & Biological Engineering Computer*. 49, 1425-1435.

Noorovi, M., Nosaka, K. and Blazevich, A., J. (2010). Assessment of quadriceps muscle cross-sectional area by ultrasound extended-field-of-view imaging. *European Journal of Applied Physiology Springer*. 109,631-639.

Özkan, K. (2015). A novel multi-scale and multi-expert edge detector based on common vector approach. *International Journal of Electronics and Communications.* 69, 1272–1281.

Pal, S. K. and King, R.A. (1981). Image Enhancement Using Smoothing with Fuzzy Sets. *IEEE Transaction on Systems. Man, Cybernetics: Systems.* 1(7), 494–501.

Panetta K., Gao C., Agaian S., and Nercessian S. (2016). A New Reference-Based Edge Map Quality Measure. *IEEE Transactions on Systems Man, and Cybernetics: Systems*. 46(11), 1505–1517.

Panetta, K., Zhou, Y., Agaian, S. and Jia, H. (2011). Nonlinear unsharp masking for mammogram enhancement. *IEEE Transaction Information Technology Biomedical.* 15(6), 918–928.

Pascal, V., Hugo, L., Isabelle, L., Yoshua, B., Manzagol, P. (2010). Stacked Denoising Autoencoders: Learning Useful Representations in a Deep Network with a Local Denoising Criterion. *Journal of Machine Learning Research*, 11, 3371–3408.

Perona, P. and Malik, J. (1990). Scale-space and edge detection using anisotropic diffusion. *IEEE Trans. on Pattern Analysis and Machine Intelligence*. 12(7), 629–639.

Petroudi S., Loizou C., Pantziaris M., and Pattichis C. (2012). Segmentation of the common carotid intima-media complex in ultrasound images using active contours. *IEEE Transactions on Biomedical Engineering*, 59(11), 3060–3069.

Pillen, S. (2010). Skeletal muscle ultrasound. *European Journal Translational Myology*. *1*(5), 145–155.

Pinho, A.J., Almeida, L.B. and Telecomunicaw, D.E. (1995). Edge Detection Filters Based on Artificial Neural Networks *International Conference on Image Analysis and Processing,* 159–164.

Plis, S. M., Hjelm, D. R., Salakhutdinov, R., Allen, E. A., Bockholt, H. J., Long, J. D., Johnson, H. J., Paulsen, J. S., Turner, J. A. and Calhoun, V. D. (2014). Deep learning for neuroimaging: a validation study. *Frontiers in Neuroscience*. 8(229), 1-11.

Polesel, A., Ramponi, G. and Mathews, V. J. (2000). Image Enhancement via Adaptive Unsharp Masking. *IEEE Transactions on Image Processing*. 9(3), 505–510.

Poudel P., Hansen C., Sprung J., and Friebe M. (2016). 3D segmentation of thyroid ultrasound images using active contours. *Current Directions in Biomedical Engineering*. 2(1), 467–470.

Pratt, W. K. (1978). *Digital Image Processin*g. 3rd edition. New York, NY, USA:Wiley.

Qiu, F., Berglund, J., Jensen, J.R., Thakkar, P. and Ren, D. (2004). Speckle Noise Reduction in SAR Imagery Using a Local Adaptive Median Filter. *GIScience and Remote Sensing*. 41(3),.244–266.

Quick, H. H., Ladd, M. E., Hoevel, M., Bosk, S., Debatin, J. F., Laub, G. and Schroeder, T. (2002). Real-time MRI of joint movement with true FISP. *Journal of Magnetic Resonance Imaging*. 15, 710-715.

Rab, G., Petuskey, K. and Bagley, A. (2002). A method for determination of upper extremity kinematics. *Gait & Posture*. 15(2), 113–119.

Rao, Y. and Chen, L. (2012). A Survey of Video Enhancement Techniques. *Journal of Information Hiding and Multimedia Signal Processing*. *3*(1), 71–99.

Ramponi, G., Strobel, N., Mitra, S.K. and Yu, T. (1996) Nonlinear Unsharp masking methods for image contrast enhancement. *Journal of. Electron. Imaging*. 5(3), 353–366.

Rankin, J. W. and Neptune, R. R. (2012). Musculotendon lengths and moment arms for a three-dimensional upper-extremity model. *Journal of Biomechanics* 45(9), 1739–1744.

Reeves, N. D., Maganaris, E. C. N., and Narici, M. V. (2004). Ultrasonographic assessment of human skeletal muscle size. *European Journal of Applied Physiology*. 8, 116–118.

Rosen, J., Perry, J. C., Manning, N., Burns, S. & Hannaford, B. (2005). The human arm kinematics and dynamics during daily activities toward a 7 DOF upper limb powered exoskeleton. Advanced Robotics, ICAR '05. Proceedings., 12th International Conference on (pp. 532-539). Seattle, WA, USA.

Rosenberg, J. G., Ryan, E. D., Sobolewski, E. J., Scharville, M.J., Thompson, B. J. and King, G. E. (2014). Reliability of panoramic ultrasound imaging to simultaneously examine muscle size and quality of the medial gastrocnemius. *Muscle & Nerve*. 49, 736-740.

Rosenfeld, A. and Haber,S. (1985).The perimeter of a fuzzy set. *Pattern Recognition* .18(2),125-130.

Rumelhart, D., Hinton, G. and Williams, R. (1986). Learning representation by back-propagating errors. *Nature*. 333(9), 533–536.

Runkler, T.A. (1997). Selection of appropriate defuzzification methods using application specific properties. *IEEE Transactions on Fuzzy Systems*. 5(1), 72–79.

Sanada, K. and Kearns, C. F. (2006). Prediction and validation of total and regional skeletal muscle mass by ultrasound in Japanese adults. *European Journal of Applied Physiology*. 96, 24–31.

Sanches, J. M., Nascimento, J. C. and Marques, J. S. (2008). Medical Image Noise Reduction Using the Sylvester-Lyapunov equation. *IEEE Transactions on image processing, 17*(9), 1522–1539.

Schulze, M.A. and Wu, Q. (1997). Noise Reduction in Synthetic Aperture Radar Imagery Using a Morphology-based Nonlinear Filter. *Conference Proceedings of the Australian Pattern Recognition Society*. 661–666.

Scott, J., Martin, D. S., Synder, R. P., Caine, T., Matz, T., Arzeno, N. M., Buxton, R. and Snyder, L. P. (2012). Reliability and validity of panoramic ultrasound for muscle quantification. *Ultrasound in medicine and biology*. 38(9), 1656-1661.

Scott, S., H., Engstrom and Loeb, G.E. (1993). Morphometry of human thigh muscles. Determination of fascicle architecture by magnetic resonance imaging. *Journal of Anatomy* 182, 249–257.

Seth, A., Sherman, M., Reinbolt, J.A. and Delp, S.L. (2011). OpenSim: a musculoskeletal modelling and simulation framework for in silico investigations and exchange. *Procedia IUTAM*. 2, 212–232.

Shamsoddini, A. and Trinder, J. C. (2010). Image texture preservation in speckle noise suppression. *ISPRS Commission VII Symposium*. Vienna, Austria. 239–244.

Shellock, F. G., Mink,J. H., Deutsch, A. and Pressman, B. D.(1991). Kinematic Magnetic Resonance Imaging of the joints: techniques and clinical applications. *Magnetic Resonance Quarterly*. 7(2), 104-135.

Sheng, Y. and Z. G. Xia, Z.G. (1996). A comprehensive evaluation of filters for radar speckle suppression. *IGARSS 1996, IEEE Geoscience and Remote Sensing Symposium*. 1559–1561.

Silvoster, M. L. and Govindan, V. K. (2012). Enhanced CNN Based Electron Microscopy Image Segmentation. *Cybernetics and Information Technologies*, 12(2), 84–97.

Slane, L. C., Thelen, D.G. (2014). The use of 2D ultrasound elastography for measuring tendon motion and strain. *Journal of biomechanics. Elsevier*. 47, 750-754.

Smajlovic, F., Carovac, A. and Bulja, D. (2011). Sonoelastography: the method of choice for evaluation of tissue elasticity. *Journal of Health Science*. 1(1), 50–55.

Sonka M., Hlavac V. and Boyle R. (1993). Image Processing Analysis and Machine Vision, 1st edition, *UK, Cambridge*.

Takagi, T. and Sugeno, M. (1985). Fuzzy identification of system and its applications to modelling and control. *IEEE Transactions on Systems, Man, and Cybernetics*. 15(1), 116–132.

Tandon, A., Bhatt, S. and Bhargava, S. K. (2013). Dynamic musculoskeletal sonography. *JIMSA*, 26(1), 21–24.

Tao, Y., Lin, H., Bao, H., Dong, F., and Clapworthy, G. (2009). Feature enhancement by volumetric unsharp masking. *The Visual Computer*. *25*(5-7), 581–588.

Tizhoosh, H. R., Krell, G. and Michaelis, B. (1997).On Fuzzy Enhancement of Megavoltage Images in Radiation Therapy. *IEEE Conference on Fuzzy Systems, FUZZ-IEEE'97*. *3*, 1399–1404.

Toktas, H., Dundar, U., Kusbeci, Ö., Ulasli, A., Toy, O. and Oruc, S. (2016). FPL tendon thickness, tremor and hand functions in Parkinson's disease. *Open Medicine*. 11(1), 16–20.

Van der Helm, F.C.T. (1994). A finite-element musculoskeletal model of the shoulder mechanism. *Journal of Biomechanics* 27 (5), 551-569.

Van der Helm, F.C.T. and Pronk, G.M. (1994). Loading of shoulder girdle muscles in consequence of a glenohumeral arthrodesis. *Clinical Biomechanics.* 9 (3), 139-148.

Veeger, H.E.J., Van Der Helm, F.C.T., Van Der Woude, L.H.V., Pronk, G.M. and Rozendal, R.H. (1991). Inertia and muscle contraction parameters for musculoskeletal modelling of the shoulder mechanism. *Journal of Biomechanics*. 24(7), pp.615–629.

Veeger, H.E.J., Yu, B., An, K. and Rozendal, R.H. (1997). Parameters for modelling the upper extremity. *Journal biomechanics*. 30(6), pp.647–652.

Wagner, R.F., Smith, S.W., Sandrik, J.M. and Lopez, H. (1983). Statistics of Speckle in Ultrasound B-Scans. *IEEE Transactions on Sonics and Ultrasonics*. 30(3), 156–163.

Wang, H., Cruz-roa, A., Basavanhally, A., Gilmore, H., Shih, N., Feldman, M., Tomaszewski, J., Gonzalez, F. and Madabhushi, A. (2014). Mitosis detection in breast cancer pathology images by combining handcrafted and convolutional neural network features. *Journal of Medical Imaging*. 1(3), 1-10.

Ward, S.R., Hentzen, E.R., Smallwood, L.H., Eastlack, R.K., Burns, K.A., Fithian, D.C., Friden, J. and Lieber, R.L. (2006). Rotator cuff muscle architecture: implications for glenohumeral stability. Clinical Orthopaedics and Related Research. *Clinical Orthopaedics & Related Research.* 448, 157-63.

Weiss, K. L., Beltran, J., Shamam, O. M., Stilla, R. F. and Levey, M. (1986). High-Feild MR Surface-Coil Imaging of the Hand and Wrist. *Radiology*. 160, 143–146.

Wen, C.Y. and Chou, C.M. (2004). Color Image Models and its Applications to Document Examination. *Forensic Science Journal*. *3*, 23–32.

Westbrook, C. (2010) *MRI at a glance*, 2nd edition, Singapore, Wiley Blackwell.

Wood, J.E., Meek, S.G. and Jacobsen, S.C. (1989). Quantitation of human shoulder anatomy for prosthetic arm control. *Journal of Biomechanics.* 22, 273-292.

Wren, T.A.L., Yerby, S.A., Beaupre, G. S. and Carter, D.R. (2001). Mechanical properties of the human Achilles tendon. *Clinical Biomechanics*.16, 245-251.

Yang, W., Chen, Y., Liu, Y., Zhong, L., Qin, G., Lu, Z., Feng, Q. and Chen, W. (2016). Cas- cade of multi-scale convolutional neural networks for bone suppression of chest radiographs in gradient domain. *Medical. Image Analysis.* 35, 421–433. doi: 10.1016/j. media.2016.08.004.

Yu J, Ackland D.C., Pandy M.G. (2011). Shoulder muscle function depends on elbow joint position: an illustration of dynamic coupling in the upper limb. *Journal of Biomechanics*, 44(10):1859–1868.

Yu, J. S. and Habib, P. A. (2004). Normal MR imaging anatomy of the wrist and hand. *Magnetic Resonance Imaging of north America*. 12, 207-219.

Zhang, J., Lin, G., Wu, L. and Cheng, Y. (2016). Speckle filtering of medical ultrasonic images using wavelet and guided filter. *Ultrasonic*, 65, 177–193.

Zhou G.Q. and Zheng Y.P. (2015). Automatic Fascicle Length Estimation on Muscle Ultrasound Images with an Orientation-Sensitive Segmentation. *IEEE Transaction of Biomedical Engineering.* 62(12), 2828–2836.

APPENDICES

APPENDIX I

Keele University

Ref: ERP1290

15th July 2016

Shaima Jabbar
Institute for Science and Technology in Medicine
Guy Hilton Research Centre
Thornburrow Drive
Stoke-On-Trent
ST4 7QB

Dear Shaima,

Re: Identification of muscle and tendon properties from ultrasound scans

Thank you for submitting your revised application for review.

I am pleased to inform you that your application has been approved by the Ethics Review Panel. The following documents have been reviewed and approved by the panel as follows:

Document(s)	Version Number	Date
Study Advert/Poster	2	11-08-2016
Invitation Letter	2	11-08-2016
Participant Information Sheet	2	11-08-2016
Consent Form	2	11-08-2016

If the fieldwork goes beyond the date stated in your application, **1st December 2016**, or there are any other amendments to your study you must submit an 'application to amend study' form to the ERP administrator at research.erps@keele.ac.uk stating **ERP1** in the subject line of the e-mail. This form is available via http://www.keele.ac.uk/researchsupport/researchethics/

If you have any queries, please do not hesitate to contact me via the ERP administrator on research.erps@keele.ac.uk stating **ERP1** in the subject line of the e-mail.

Yours sincerely

pp C H Bonnerman

Dr Jackie Waterfield
Chair – Ethical Review Panel

CC RI Manager
Supervisor

Directorate of Engagement & Partnerships
T: +44(0)1782 734467

Keele University, Staffordshire ST5 5BG, UK
www.keele.ac.uk +44 (0)1782 732000

APPENDIX II

A list of presentations and posters that have resulted from the work

A. Conference oral presentation:

1- IEEE (WCCI) Congress Vancouver Canada, June 24-29, 2016. The title of paper is'' Using convolutional neural network for Edge Detection in Musculoskeletal Ultrasound Images''. I attended and presented 20 minutes.

2- MEIbioeng Conference 2016 in Oxford university, September 5-6, 2016. The title of paper is "Speckle Noise Reduction in Musculoskeletal Ultrasound Panoramic Imaging''. I attended and presented 15 minutes.

3- 7th Computing and Mathematics Postgraduate Research Day (Keele university), April 5, 2017, I attended and presented 20 minutes.

4- 2nd Crossing path conference 2017, (Keele university), April 16, 2017, I attended and presented three minutes.

5- 8th Computing and Mathematics Postgraduate Research Day (Keele university), April 11, 2018, I attended and presented 10 minutes.

B. Conference Poster presentation:

- Keele Postgraduate Conference 2016, (Keele university), April 18, 2016, I attended and presented a poster.
- Health Research conference 2016, (Keele university), October 14, 2016, I attended and presented a poster.

C. Journal Publications:

- Journal article is submitted to the Medical engineering and Physics journal and currently it is under review. This article is "Automated Analysis of Ultrasound Image of the Flexor Pollicis Longus Tendon".

APPENDIX III

Rules of local fuzzy contrast enhancement method

Rule1: If (central pixel (C_5) is brightness AND C_1 is darkness) OR
(central pixel (C_5) is brightness AND C_2 is darkness) OR
(central pixel (C_5) is brightness AND C_3 is darkness) OR
(central pixel (C_5) is brightness AND C_4 is darkness) OR
(central pixel (C_5) is brightness AND C_6 is darkness) OR
(central pixel (C_5) is brightness AND C_7 is darkness) OR
(central pixel (C_5) is brightness AND C_8 is darkness) OR
(central pixel (C_5) is brightness AND C_9 is darkness) THEN
*Z=Sd.*Y*

Rule2: If (central pixel (C_5) is grey AND C_1 is darkness) OR
(central pixel (C_5) is grey AND C_2 is darkness) OR
(central pixel (C_5) is grey AND C_3 is darkness) OR
(central pixel (C_5) is grey AND C_4 is darkness) OR
(central pixel (C_5) is grey AND C_6 is darkness) OR
(central pixel (C_5) is grey AND C_7 is darkness) OR
(central pixel (C_5) is grey AND C_8 is darkness) OR
(central pixel (C_5) is grey AND C_9 is darkness) THEN
*Z=Sd.*Y.*

Rule3: If (central pixel (C_5) is brightness AND C_1 is grey) OR
(central pixel (C_5) is brightness AND C_2 is grey) OR
(central pixel (C_5) is brightness AND C_3 is grey) OR
(central pixel (C_5) is brightness AND C_4 is grey) OR
(central pixel (C_5) is brightness AND C_6 is grey) OR
(central pixel (C_5) is brightness AND C_7 is grey) OR
(central pixel (C_5) is brightness AND C_8 is grey) OR
(central pixel (C_5) is brightness AND C_9 is grey) THEN
*Z=Sd.*Y.*

Rule4: If (central pixel (C_5) is darkness AND C_1 is grey) OR
(central pixel (C_5) is darkness AND C_2 is grey) OR
(central pixel (C_5) is darkness AND C_3 is grey) OR
(central pixel (C_5) is darkness AND C_4 is grey) OR
(central pixel (C_5) is darkness AND C_6 is grey) OR
(central pixel (C_5) is darkness AND C_7 is grey) OR
(central pixel (C_5) is darkness AND C_8 is grey) OR
(central pixel (C_5) is darkness AND C_9 is grey) THEN
Z=Y- Se.

Rule5: If (central pixel (C_5) is darkness AND C_1 is brightness) OR
(central pixel (C_5) is darkness AND C_2 is brightness) OR
(central pixel (C_5) is darkness AND C_3 is brightness) OR
(central pixel (C_5) is darkness AND C_4 is brightness) OR
(central pixel (C_5) is darkness AND C_6 is brightness) OR
(central pixel (C_5) is darkness AND C_7 is brightness) OR
(central pixel (C_5) is darkness AND C_8 is brightness) OR

(central pixel (C_5) is darkness AND C_9 is brightness) THEN
Z=Y- Se.

Rule6: If (central pixel (C_5) is grey AND C_1 is brightness) OR
(central pixel (C_5) is grey AND C_2 is brightness) OR
(central pixel (C_5) is grey AND C_3 is brightness) OR
(central pixel (C_5) is grey AND C_4 is brightness) OR
(central pixel (C_5) is grey AND C_6 is brightness) OR
(central pixel (C_5) is grey AND C_7 is brightness) OR
(central pixel (C_5) is grey AND C_8 is brightness) OR
(central pixel (C_5) is grey AND C_9 is brightness) THEN
Z=Y- Se.

Rules of fuzzy edge detection method

Rule 1: If (C_1, C_3, & C_5) are high & (C_2, C_4, C_6, C_7, C_8, & C_9) are low then central pixel is edge.
Rule 2: If (C_5, C_7, & C_9) are high & (C_1, C_2, C_3, C_4, C_6, & C_8) are low then central pixel is edge.
Rule 3: If (C_1, C_5, & C_7) are high & (C_2, C_3, C_4, C_6, C_8, & C_9) are low then central pixel is edge.
Rule 4: If (C_3, C_5, & C_9) are high & (C_1, C_2, C_4, C_6, C_7, & C_8) are low then central pixel is edge.
Rule 5: If (C_2, C_5, & C_6) are high & (C_1, C_3, C_4, C_7, C_8, & C_9) are low then central pixel is edge.
Rule 6: If (C_2, C_4, & C_5) are high & (C_1, C_3, C_6, C_7, C_8, & C_9) are low then central pixel is edge.
Rule 7: If (C_4, C_5, & C_8) are high & (C_1, C_2, C_3, C_6, C_7, & C_9) are low then central pixel is edge.
Rule 8: If (C_5, C_6, & C_8) are high & (C_1, C_2, C_3, C_4, C_7, & C_9) are low then central pixel is edge.
Rule 9: If (C_4, C_5, & C_6) are high & (C_1, C_2, C_3, C_7, C_8, & C_9) are low then central pixel is edge.
Rule 10: If (C_2, C_5, & C_8) are high & (C_1, C_3, C_4, C_6, C_7, & C_9) are low then central pixel is edge.
Rule 11: If (C_3, C_5, & C_7) are high & (C_1, C_2, C_4, C_6, C_8, & C_9) are low then central pixel is edge.
Rule 12: If (C_1, C_5, & C_9) are high & (C_2, C_3, C_4, C_6, C_7, & C_8) are low then central pixel is edge.